Shift Currents in Bulk GaAs and GaAs Quantum Wells Analyzed by a Combined Approach of k·p Perturbation Theory and the Semiconductor Bloch Equations

Dissertation zur Erlagung
des Doktorgrades der Naturwissenschaften (Dr. rer. nat.)
dem Department Physik der Fakultät für Naturwissenschaften
der Universität Paderborn vorgelegt von

Reinold Ephraim Podzimski
Paderborn, December 15, 2016

UNIVERSITÄT PADERBORN
Die Universität der Informationsgesellschaft

Hiermit erkläre ich, dass ich die vorliegende Arbeit selbstständig angefertigt, nicht anderweitig zu Prüfungszwecken vorgelegt und keine anderen als die angegebenen Hilfsmittel verwendet habe. Sämtliche wissentlich verwendete Textausschnitte, Zitate oder Inhalte anderer Verfasser wurden ausdrücklich als solche gekennzeichnet.

Paderborn, December 15, 2016

Reinold Ephraim Podzimski

Contents

Chapter 1

Abstract

A combined theory of k.p-perturbation theory and the semiconductor Bloch equations (SBE) is used to simulate photo currents in GaAs based systems. The focus lies on the so-called shift current, a microscopic current caused by the spatial motion of excited carriers inside the crystal structure. The validity of the combined theory is tested for the example of bulk GaAs using known symmetry properties of shift currents. Using the SBE, which allow for a non-perturbative and k-resolved analysis of shift currents, various linear and non-linear properties of shift currents are investigated, in particular, signatures of Rabi-oscillations in bulk and the influence of band-mixing in quantum well systems.

Excitonic effects in shift currents are investigated for a full three-dimensional band structure. The inclusion of Coulomb interaction is numerically demanding and normally done using approximations, e.g., a parabolic band structure. Such approximations cannot be applied for shift currents. To deal with this numerical challenge, the development of a new non-uniform grid is necessary. The convergence and accuracy of the new grid as well as the obtained results for the exciton binding energy and the shift current are presented and discussed.

A novel method is developed which consists of combining k.p-perturbation theory with real-space wave function obtained from density functional theory. The method allows to simulate shift currents in real-space with atomic resolution.

Kurzfassung

Eine vereinheitlichte Theorie von k.p Störungtheorie und den Halbleiter-Bloch-Gleichung wird benutzt für die Simulation von Photoströmen in GaAs-Systemen. Der Fokus der Arbeit ist die theoretische Beschreibung und Analyse des sogenannten Shiftstroms, ein mikroskopischer Strom erzeugt durch die räumliche Bewegung von angeregten Ladungsträgern. Mit Hilfe bekannter Eigenschaften des Shiftstroms wird die Theorie am Beispiel eines GaAs Festkörperkristalls getestet. Der nicht störungstheoretische Ansatz der Halbleiter-Bloch-Gleichungen erlaubt die Analysis von linearen und nichtlinearen Eigenschaften des Shiftstroms.

Der Einfluss von exzitionischen Effekten auf den Shiftstrom wird für einen dreidimensionalen Kristall untersucht. Der numerische Aufwand für die Einbindung der Coulombwechselwirkung wird häufig durch Näherungen reduziert, diese sind jedoch für den Shiftstrom nicht möglich. Die Einbindung der Coulombwechselwirkung bedarf der Entwicklung eines neuen, nicht uniformen Gitters. Sowohl die Konvergenzeigenschaften und die Genauigkeit des Gitters als auch die simulierten Shiftstrom-Resultate werden vorgestellt und diskutiert.

Eine neue Methode wird vorgestellt, die k.p Störungstheorie mit Realraum-Wellenfunktionen aus Dichtefunktionaltheorie kombiniert. Diese ermöglicht die Simulation von Shiftströmen im Realraum mit atomarer Auflösung.

Chapter 2

Introduction

An electric current is a controlled energy transport without the involvement of macroscopic moving components. This seems self-evident today, but it was a major factor in the so-called second industrial revolution in the middle of the 19th century. It enabled to power devices without the use of mechanical belts, was used for long range communication via the invention of the telegram and the phone, and led to the invention of the electric lamp, a small and practical artificial light source for its time. After decades of miniaturization and development electric currents are an indispensable part of the modern world and omni-present. With world wide increasing power consumption and environmental protection being a big challenge, research and development of alternative energy sources and the development of more power efficient devices is a very important research topic.

From early on it is known that optical light can be transformed into kinetic energy in the form of electronic motion. The photoelectric effect is a prime example of this, describing an electron absorbing a photon and escaping its environment.[1, 2] For gallium arsenide (GaAs) this process of photo-ionization, which lifts the electron from its bound state to the vacuum level, corresponds to a photon energy of at least $E_{esc} = 3eV$.[3] In comparison, the photovoltaic effect describes an electron absorbing a photon but not leaving its environment. Instead, the electron moves in it and thus creates a microscopic current. The energy transformation of optical light into an electric current is a broad field of research because of the large number of suitable materials and their potential applications. Materials ranging from classical bulk, to quantum wells and quantum dots, and to organic molecules can be used for numerous photoelectric applications, e.g. solar cells, photosynthesis, and optical control.[4–6] A classical and widespread material for photo current generation are semiconductors and semiconductor nanostructures which are used in the construction of solar panels.[7]

The non-linear optical properties of semiconductors allow for a large variety of applications, like second harmonic generation or THz spectroscopy, to name just a few.[8–12] Under usual circumstances, no external bias or magnetic field, optical excitation does not generate electric currents in semiconductors. But using quantum interference as in two-color excitation, i.e., an excitation with two different photon energies, it is possible to generate currents in the semiconductor band structure.[13–16] Using certain material properties, e.g. inversion asymmetry or reduced dimensionality in a quantum well, it is also possible to generate currents by only one-color excitation.[17–22] One particular photocurrent is the so-called injection current which is caused by an asymmetric distribution of carriers in **k**-space. In the past, several investigations were performed for injection currents in GaAs quantum well systems.[23–27]

In this work the focus lies on another kind of current, the so-called shift current. The shift current is caused by the shift of carriers in real-space induced by optical excitation. Experimental research on shift current was performed for bulk materials[28–30] as well as quantum well system[31–34]. Shift currents can appear in different material types such as semiconductors, ferroelectrical, and antiferromagnetical materials.[35–38] Previous theoretical research on shift current was performed using theories limited to frequency space.[39–41]
In contrast, a combined theory of k.p perturbation theory and semiconductor Bloch equations is presented in this work which allows for the description of shift currents in time domain. This approach has the advantage that it allows for investigations beyond the perturbation limit and can be straight forwardly expanded to include excitonic effects. The combined theory has been used to describe the injection current in GaAs based systems in good agreement with experiment.[24, 25]

The scope of this work lies on the question how well the combined theory is capable of describing shift currents in various semiconductor systems. The thesis begins with an introduction to the theoretical basics of k.p perturbation theory and the semiconductor Bloch equations in Chapter 3. In addition, a brief motivation and explanation about the so-called geodesic grid is given which will be of major importance for simulations with Coulomb interaction.
In Chapter 4 the validity of the combined theory is tested for the example of bulk GaAs by reproducing known shift current properties. After confirming the shift current properties, various non-linear properties of shift currents are

investigated. Further, the advantages and disadvantages of simulations with a non-uniform geodesic grid and with a Cartesian grid are compared and discussed.
In Chapter 5 the combined theory is used for the simulation of quantum well systems. In a quantum well the reduced dimensionality has a great impact on the band structure which gives rise to new effects. How the reduced dimensionality affects the shift current is studied.
In Chapter 6 the excitonic effects on shift currents near the band gap are investigated for a full three-dimensional band structure. A detailed explanation for the inclusion of the numerically challenging Coulomb interaction is given and the exciton binding energy is calculated for a parabolic and a k.p band structure. Afterwards, the exciton contributions to the shift current are presented and discussed.
In Chapter 7 a brief discussion about another type of photo current, the rectification current, is held for bulk GaAs and GaAs quantum well systems.
Finally, in Chapter 8 a novel method is developed which enables the visualization of shift currents with atomic resolution in real-space.

Publications in the context of this thesis

Some of the result this thesis have been presented at conferences,

- R. Podzimski, H. T. Duc, and T. Meier, Time-domain calculations of shift currents in bulk GaAs, Proc. SPIE, vol. 93611V, p. 9361, 2015.
- R. Podzimski, H. T. Duc, and T. Meier, Photocurrents in semiconductors and semiconductor quantum wells analyzed by k.p-based Bloch-equations, Proc. SPIE, vol. 97460W, p. 9746, 2016.

and have been published:

- E. Sternemann, T. Jostmeier, C. Ruppert, S. Thunich, H. T. Duc, R. Podzimski, T. Meier, and M. Betz, Quantum interference control of electrical currents in gaas microstructures: Physics and spectroscopic applications, Applied Physics B, vol. 122, p. 44, 2016.
- H. T. Duc, R. Podzimski, S. Priyadarshi, M. Bieler, and T. Meier, Ultrafast shift and rectifcation photocurrents in gaas quantum wells: Excitation intensity dependence and the importance of band mixing, Phys. Rev. B, vol. 94, p. 085305, 2016.

Chapter 3

Theoretical Basics

In this thesis a unified approach of k.p perturbation theory and the semiconductor Bloch equations is employed to simulate different photo currents in GaAs-based systems. The k.p perturbation theory is a well established method for the calculation of semiconductor band structures in bulk and quantum well systems.[42–48] Over the decades several different k.p models were developed, ranging from 6×6 band models for calculations around the Γ-point to 30×30 full Brillouin zone calculations, QW models incorporating strain effects, and spin-orbit coupling.[49–52] The time evolution of the photo-excited system is described via the semiconductor Bloch equations, abbreviated as **SBE**, a set of non-linear coupled differential equations used to simulate the optical excitations inside a semiconductor.[53, 54] The SBE can be used to describe numerous effects inside semiconductors, i.e., Bloch oscillations or the electron g-factor in a quantum well.[44, 55] The theoretical basics of k.p theory, in particular the extended Kane model, and the SBE are presented in this Chapter.

For theoretical simulations Cartesian standard grids are often used due to their uniformity and easy implementation, but they have the disadvantages of including non-important areas and bad scaling behavior. In contrast, non-standard grids, which are adapted for the specific problems and only include the important areas of the simulation space, have a better scaling having behavior leading to improved calculation times, but are harder to implement as a consequence. A non-standard **geodesic grid** is used for the photo current simulations and the exciton calculations in Chapter 6. Its advantages over an Cartesian grid are of great importance for the band edge calculations including Coulomb interaction. The basics and construction of a geodesic grid are described at the end of this Chapter.

3.1 Extended Kane Model

3.1.1 Basics of k.p Perturbation Theory

The band structure of GaAs is obtained by solving the extended Kane model, a 14-band Hamiltonian based on k.p perturbation theory[46, 52]. As the name implies, the k.p perturbation theory is a perturbative approach for solving the stationary Schrödinger equation $\hat{\mathrm{H}}|\varphi\rangle = E|\varphi\rangle$ of a particle in the periodic potential of a crystal. The theory starts with the Hamiltonian for a particle in a periodic potential V_0

$$\hat{\mathrm{H}} = \frac{\hat{p}}{2m_0} + V_0. \tag{3.1}$$

The eigenfunctions $|\varphi\rangle$ of Eq. (3.1) have to satisfy the Bloch theorem $|\varphi\rangle = e^{\mathbf{ik}\cdot\mathbf{r}}|\nu\rangle$. After solving the eigenvalue equation for the plane wave term $e^{\mathbf{ik}\cdot\mathbf{r}}$, the Hamiltonian for the unit cell periodic part $|\nu\rangle$ of the Bloch theorem is

$$\hat{\mathrm{H}}_0 = \hat{\mathrm{H}} + \frac{\hbar^2 k^2}{2m_0} + \frac{\hbar}{m_0}\mathbf{k}\cdot\mathbf{p}, \tag{3.2}$$

with $E_\nu(\mathbf{k})$ being its eigenvalues. Besides the quadratic term $\frac{\hbar^2 k^2}{2m_0}$ the Hamiltonian $\hat{\mathrm{H}}_0$ contains the name giving $\mathbf{k}\cdot\mathbf{p}$ coupling term. In addition to $\mathbf{k}\cdot\mathbf{p}$ coupling the extended Kane model also includes spin-orbit interaction. The spin-orbit interaction is responsible for a spin-splitting of electron states in inversion asymmetric systems even without an external magnetic field.[56–59] To include spin-orbit interaction in k.p theory, the spin-orbit Hamiltonian $\hat{\mathrm{H}}_{SO}$ is added to the Hamiltonian (3.1) as a small perturbation,

$$\hat{\mathrm{H}} + \hat{\mathrm{H}}_{SO} = \hat{\mathrm{H}} - \frac{\hbar}{4m_0^2c^2}\boldsymbol{\sigma}\cdot\hat{\mathbf{p}}\times(\nabla V_0), \tag{3.3}$$

with $\boldsymbol{\sigma} = (\sigma_x, \sigma_y, \sigma_z)$ being the vector of the Pauli spin matrices.[60] Solving the plane wave term $e^{\mathbf{ik}\cdot\mathbf{r}}$ for $\hat{\mathrm{H}}_{S0}$ leads to the full k.p Hamiltonian:

$$\begin{aligned}\hat{\mathrm{H}}_{k.p} &= \hat{\mathrm{H}}_0 + \frac{\hbar}{4m_0^2c^2}\left\{\hbar\mathbf{k} + \hat{\mathbf{p}}\right\}\cdot\boldsymbol{\sigma}\times(\nabla V_0)\\ &= \hat{\mathrm{H}} + \frac{\hbar^2k^2}{2m_0} + \frac{\hbar}{m_0}\mathbf{k}\cdot\mathbf{p} + \frac{\hbar}{4m_0^2c^2}\left\{\hbar\mathbf{k} + \hat{\mathbf{p}}\right\}\cdot\boldsymbol{\sigma}\times(\nabla V_0)\\ &= \frac{\hat{p}}{2m_0} + V_0 + \frac{\hbar^2k^2}{2m_0} + \frac{\hbar}{m_0}\mathbf{k}\cdot\mathbf{p} + \frac{\hbar}{4m_0^2c^2}\left\{\hbar\mathbf{k} + \hat{\mathbf{p}}\right\}\cdot\boldsymbol{\sigma}\times(\nabla V_0)\end{aligned} \tag{3.4}$$

The new eigenkets $|\lambda\mathbf{k}\rangle$ of Eq. (3.4) are expanded in a tensor product consisting of the old eigenkets $|\nu\mathbf{k}\rangle$ of the unperturbed Hamiltonian (3.2) and the spinor basis $|\sigma\rangle$,

$$|\lambda\mathbf{k}\rangle = \sum_{\nu;\sigma=\uparrow,\downarrow} c_{\lambda\nu\sigma}(\mathbf{k})|\nu\mathbf{k}=\mathbf{0}\rangle \otimes |\sigma\rangle. \tag{3.5}$$

Multiplying the bra vector $\langle\nu'\mathbf{k}=\mathbf{0}| \otimes \langle\sigma'|$ from the left to Eq. (3.5) gives the eigenvalue equation

$$\sum_{\nu',\sigma'} \left\{ \left[E_\nu(0) + \frac{\hbar^2 k^2}{2m_0} \right] \delta_{\nu\nu'}\delta_{\sigma\sigma'} + \frac{\hbar}{m_0}\mathbf{k}\cdot\mathbf{P}^{\nu\nu'}_{\sigma\sigma'} + \Delta^{\nu\nu'}_{\sigma\sigma'} \right\} c_{\lambda\nu'\sigma'}(\mathbf{k}) = E_\lambda(k) c_{\lambda\nu\sigma}(\mathbf{k}), \tag{3.6}$$

with $\mathbf{P}^{\nu\nu'}_{\sigma\sigma'}$ and $\Delta^{\nu\nu'}_{\sigma\sigma'}$ being material specific parameters obtained from experiment.

With infinite bands involved, Eq. (3.6) is an infinite eigenvalue problem and numerically unsolvable. For numerical calculations a reduction to a finite number of bands is required and done in three steps. First, the theory of invariants is applied to write the Hamiltonian in terms of its universal symmetry invariant form $\hat{\mathrm{H}}_I(\mathbf{k})$. Second, Löwdin partitioning is used to derive a finite Hamiltonian $\hat{\mathrm{H}}_L(\mathbf{k})$. Third, the invariant Hamiltonian $\hat{\mathrm{H}}_I(\mathbf{k})$ and the finite Hamiltonian $\hat{\mathrm{H}}_L(\mathbf{k})$ are matched to each other. Using this method one arrives at a finite eigenvalue problem usable for numerical simulations. A more detailed description of the theory of invariants and Löwdin partitioning can be found in Appendix A.1.1 and Appendix A.1.2.

3.1.2 Invariant Formulation of the Extended Kane Model

The extended Kane model is a 14 band k.p Hamiltonian for semiconductors with zincblende structure.[52, 61] The Hamiltonian consists of 6 valence bands, the split-off band $|7v\rangle$ and the heavy & light hole band $|8v\rangle$, and 8 conduction bands, the lowest conduction band $|6c\rangle$ with s-symmetry and the higher conduction bands $|7c\rangle$ & $|8c\rangle$ with p-symmetry. At the gamma point $\mathbf{k}=0$ the bands $|8v\rangle$ and $|8c\rangle$ are fourfold degenerate. The Hamiltonian of the extended Kane model is

$$\hat{\mathrm{H}}_{14\times14} = \begin{pmatrix} \hat{\mathrm{H}}_{8c8c} & \hat{\mathrm{H}}_{8c7c} & \hat{\mathrm{H}}_{8c6c} & \hat{\mathrm{H}}_{8c8v} & \hat{\mathrm{H}}_{8c7v} \\ \hat{\mathrm{H}}_{7c8c} & \hat{\mathrm{H}}_{7c7c} & \hat{\mathrm{H}}_{7c6c} & \hat{\mathrm{H}}_{7c8v} & \hat{\mathrm{H}}_{7c7v} \\ \hat{\mathrm{H}}_{6c8c} & \hat{\mathrm{H}}_{6c7c} & \hat{\mathrm{H}}_{6c6c} & \hat{\mathrm{H}}_{6c8v} & \hat{\mathrm{H}}_{7c7v} \\ \hat{\mathrm{H}}_{8v8c} & \hat{\mathrm{H}}_{8v7c} & \hat{\mathrm{H}}_{8v6c} & \hat{\mathrm{H}}_{8v8v} & \hat{\mathrm{H}}_{8v7v} \\ \hat{\mathrm{H}}_{7v8c} & \hat{\mathrm{H}}_{7v7c} & \hat{\mathrm{H}}_{7v6c} & \hat{\mathrm{H}}_{7v8v} & \hat{\mathrm{H}}_{7v7v} \end{pmatrix}. \tag{3.7}$$

The sub-Hamiltonians of the extended Kane model have the invariant form of:

$$
\begin{aligned}
\hat{\mathrm{H}}_{8c8c} =& E_0' + \Delta_0' \\
\hat{\mathrm{H}}_{7c7c} =& E_0' \\
\hat{\mathrm{H}}_{6c6c} =& E_0 + \frac{\hbar^2 k^2}{2m'} \\
\hat{\mathrm{H}}_{8v8v} =& \frac{-\hbar^2}{2m_0} \left\{ \gamma_1' k^2 - 2\gamma_2' \left[\left(J_x^2 - \frac{1}{3} J^2 \right) k_x^2 + cp \right] - 4\gamma_3' \left[\left\{ J_x, J_y \right\} \left\{ k_x, k_y \right\} + cp \right] \right\} \\
&+ \frac{2}{\sqrt{3}} C_k \left[\left\{ J_x, J_y^2 - J_z^2 \right\} k_x + cp \right] \\
\hat{\mathrm{H}}_{7v7v} =& -\Delta_0 - \frac{\hbar^2}{2m_0} \gamma_1' k^2 \\
\hat{\mathrm{H}}_{8c7c} =& 0 \\
\hat{\mathrm{H}}_{8c6c} =& -\sqrt{3} P' \left(U_x k_x + cp \right) \\
\hat{\mathrm{H}}_{8c8v} =& -\frac{2}{3} Q \left(\left\{ J_y, j_z \right\} k_x + c.p \right) + \frac{1}{3} \Delta^- \\
\hat{\mathrm{H}}_{8c7v} =& -2Q \left(U_{yz} k_x + cp \right) \\
\hat{\mathrm{H}}_{7c6c} =& \frac{1}{\sqrt{3}} P' \left(\sigma_x k_x + cp \right) \\
\hat{\mathrm{H}}_{7c8v} =& -2Q \left(T_{yz} + cp \right) \\
\hat{\mathrm{H}}_{7c7v} =& -\frac{2}{3} \Delta^- \\
\hat{\mathrm{H}}_{6c8v} =& \sqrt{3} P \boldsymbol{T} \cdot \mathbf{k} \\
\hat{\mathrm{H}}_{6c7v} =& -\frac{1}{3} P \boldsymbol{\sigma} \cdot \boldsymbol{k} \\
\hat{\mathrm{H}}_{8v7v} =& -\frac{\hbar^2}{2m_0} \left[-6\gamma_2' \left(U_{xx} k_x^2 + cp \right) - 12\gamma_3' \left(U_{xy} \left\{ k_x, k_y \right\} + cp \right) \right] \\
&- \mathrm{i}\sqrt{3} C_k \left(U_{yz} k_x + cp \right) \qquad (3.8)
\end{aligned}
$$

The abbreviation *cp* stands for cyclic permutation and $\{A, B\} = \frac{1}{2}(AB + BA)$.[62]

The first five terms are the diagonal terms of the Hamiltonian containing the fundamental band energies at $\mathbf{k} = \mathbf{0}$, i.e., the Γ-point. The remaining off-diagonal terms represent the inter- and intraband interaction. The parameters for the extended Kane model are material specific and are acquired from experiment, see the Appendix A.1.4 for the used values in this work. The GaAs band structure is obtained by a diagonalization of the eigenvalue equation

$$\hat{\mathrm{H}}_{14\times14}(\mathbf{k})|\lambda, \mathbf{k}\rangle = \epsilon_\lambda(\mathbf{k})|\lambda, \mathbf{k}\rangle \qquad (3.9)$$

for the desired number of **k**-points, with $\hat{\mathrm{H}}_{14\times14}$ being the full 14 band k.p

Table 3.1: Tensor matrices used in the extended Kane model. The explicit form of the sub matrices can found in Appendix A.1.3.

$$
\begin{aligned}
\boldsymbol{\sigma} &= (\sigma_x|\sigma_y|\sigma_z)\\
\boldsymbol{J} &= (J_x|J_y|J_z)\\
\boldsymbol{\mathcal{J}} &= (J_x^3|J_y^3|J_z^3)\\
\boldsymbol{T} &= (T_x|T_y|T_z)\\
\boldsymbol{U} &= (U_x|U_y|U_z)
\end{aligned}
$$

Hamiltonian. The extended Kane model includes **k**-terms up to the third order and accurately describes the band structure near the Γ-point, but for larger k-vectors k.p-models with a higher number of bands are required.

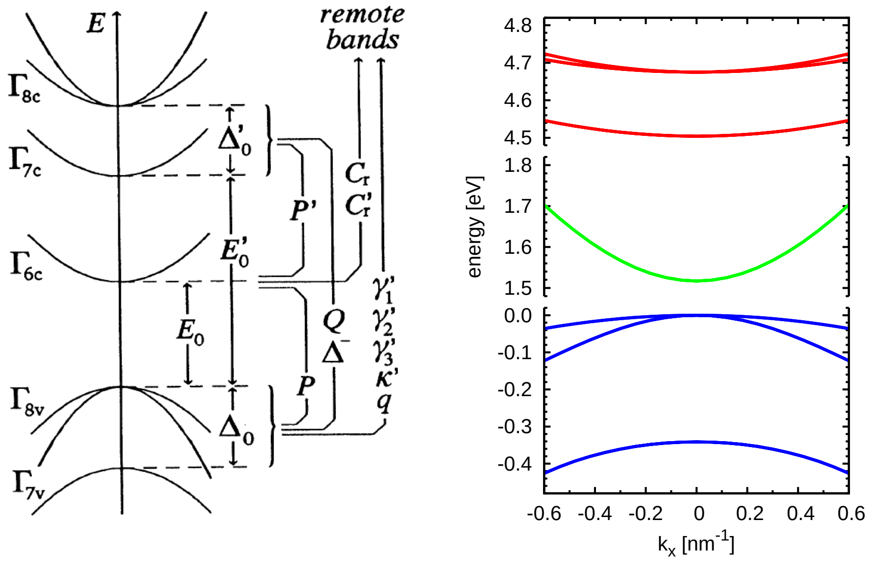

Figure 3.1: Left: The schematic band structure of the extended Kane model, taken from [46]. The parameters E_0, E'_0, Δ_0 and Δ'_0 stand for the energy separation of the bands at the Γ-point. The parameter P, P', Q and Δ^- represent coupling between the bands of the extended Kane model. Contributions of higher bands are factored in by the remaining parameters. Right: A calculated band structure for GaAs using the extend Kane model along the $\mathbf{k} = k_x\mathbf{e}_x$ direction. The valence bands $|7v\rangle$ & $|8v\rangle$, blue, the lowest conduction band $|6c\rangle$, green, and the higher conduction bands $|7c\rangle$ & $|8c\rangle$, red, are displayed.

3.2 Semiconductor Bloch Equations

The semiconductor Bloch equations (SBE) are a set of coupled first-order nonlinear differential equations and are used for the simulation of the time evolution of optical excitations in the system. The Hamiltonian for a particle inside the band structure of a semiconductor has the form

$$\hat{\mathrm{H}} = \hat{\mathrm{H}}_0 + \hat{\mathrm{H}}_{LM} + \hat{\mathrm{H}}_C. \tag{3.10}$$

The Hamiltonian

$$\hat{\mathrm{H}}_0 = \sum_{\lambda\mathbf{k}} \epsilon^\lambda_{\mathbf{k}} \hat{a}^{\dagger\lambda}_{\mathbf{k}} \hat{a}^\lambda_{\mathbf{k}} \tag{3.11}$$

represents the unperturbed system. $\epsilon^\lambda_{\mathbf{k}}$ is the energy of band λ at a point $\mathbf{k}$ in reciprocal space and $\hat{a}^{\dagger\lambda}_{\mathbf{k}}$ & $\hat{a}^\lambda_{\mathbf{k}}$ the corresponding electron creation and annihilation operators.

The Hamiltonian $\hat{\mathrm{H}}_{LM}$ represents the light-matter interaction and its explicit form depends on the used gauge. In this work the velocity gauge is used in which the electric field is described via the electromagnetic vector potential $\mathbf{A}(t)$.[63] In the velocity gauge the Hamiltonian for a particle in an external electric field has the form

$$\hat{\mathrm{H}} = \frac{1}{2m}\left[\hat{\mathbf{p}} - \frac{e}{c}\mathbf{A}(t)\right]^2 + V(\mathbf{r}), \tag{3.12}$$

with e being the electron charge and c the speed of light. This is the so-called minimal coupling Hamiltonian. Solving the brackets, the homogeneous term

$$\hat{\mathrm{H}}_0 = \frac{\hat{\mathbf{p}}^2}{2m} + V(\mathbf{r}) \tag{3.13}$$

represents an unperturbed particle in a potential $V(\mathbf{r})$. For a periodic crystal potential, the Hamiltonian in Eq. (3.13) is equivalent to the band structure Hamiltonian in Eq. (3.11). The remaining term

$$\hat{\mathrm{H}}^{\pi A}_{LM} = -\frac{e}{2mc}\mathbf{A}(t)\cdot\hat{\mathbf{p}} + \frac{e^2}{2mc^2}\mathbf{A}^2(t) \tag{3.14a}$$

$$= -\frac{e}{2mc}\mathbf{A}(t)\cdot\sum_{\lambda\lambda'}\mathbf{\Pi}^{\lambda\lambda'}_{\mathbf{k}}\hat{a}^{\dagger\lambda}_{\mathbf{k}}\hat{a}^{\lambda'}_{\mathbf{k}} + \frac{e^2}{2mc^2}\mathbf{A}^2(t) \tag{3.14b}$$

represents the light-matter interaction, with $\mathbf{\Pi}^{\lambda\lambda'}_{\mathbf{k}}$ being the so-called velocity matrix element.

Alternatively, the light-matter interaction can be expressed in the dipole gauge, also called length gauge[64], where the light-matter Hamiltonian has the form

$$\hat{\mathrm{H}}_{LM}^{qE} = -e\hat{\mathbf{r}}\cdot\mathbf{E} \tag{3.15a}$$

$$= -\mathbf{E}\cdot\sum_{\lambda\lambda'}\mathbf{d}_{\mathbf{k}}^{\lambda\lambda'}\hat{a}_{\mathbf{k}}^{\dagger\lambda}\hat{a}_{\mathbf{k}}^{\lambda'}, \tag{3.15b}$$

with $\mathbf{E} = -\frac{\dot{\mathbf{A}}}{\mathbf{c}}$ being the external electric field and $\mathbf{d}_{\mathbf{k}}^{\lambda\lambda'}$ the so-called dipole matrix element. Because physics has to be gauge independent, both gauges should be equivalent. But due to approximations and numerical constraints, e.g. an infinite number of bands cannot be evaluated in a numerical simulation, the gauges may yield different results depending on the optical excitation, especially for below band gap excitation.[65]

The last Hamiltonian $\hat{\mathrm{H}}_C$ represents the Coulomb interaction in the system. In the first half of this dissertation Coulomb interaction is omitted and therefore the Hamiltonian is considered to be

$$\hat{\mathrm{H}}_C = 0 \tag{3.16}$$

at this point. From a numerical point of view the incorporation of Coulomb interaction for an anisotropic multi-band system is very demanding and will be discussed in detail in Chapter 6.

The two point operator $\hat{x}_k^{\lambda\lambda'} = \hat{a}_{\mathbf{k}}^{\dagger\lambda}\hat{a}_{\mathbf{k}}^{\lambda'}$ describes the state of the system at a given time t, with λ and λ' being band indices. For $\lambda = \lambda'$ the operator $\hat{x}_{\mathbf{k}}^{\lambda\lambda'} = \hat{n}_{\mathbf{k}}^{\lambda}$ represents the population in band λ. For $\lambda \neq \lambda'$, $\hat{x}_{\mathbf{k}}^{\lambda\lambda'} = \hat{p}_{\mathbf{k}}^{\lambda\lambda'}$ represents the inter- or intraband polarization between band λ and λ'. The equation of motion for an arbitrary operator $\hat{A}$ can be obtained from the Heisenberg equation[60]

$$\frac{\partial A}{\partial t} = \left\langle\frac{\partial\hat{A}}{\partial t}\right\rangle = -\frac{\mathrm{i}}{\hbar}\left\langle\left[\hat{\mathrm{H}},\hat{A}\right]\right\rangle. \tag{3.17}$$

Evaluating Eq. (3.17) for $\hat{A} = \hat{x}_k^{\lambda\lambda'} = \hat{a}_{\mathbf{k}}^{\dagger\lambda}\hat{a}_{\mathbf{k}}^{\lambda'}$ and $\hat{\mathrm{H}} = \hat{\mathrm{H}}_0 + \hat{\mathrm{H}}_{LM}^{\pi A}$ leads to the SBE. A full derivation of the Heisenberg equation can be found in the Appendix A.1.5. The SBE have the explicit form of:

$$\frac{d}{dt}x_{\mathbf{k}}^{\lambda\lambda'} = \frac{\mathrm{i}}{\hbar}\left(\epsilon_{\mathbf{k}}^{\lambda}-\epsilon_{\mathbf{k}}^{\lambda'}\right)x_{\mathbf{k}}^{\lambda\lambda'} + \frac{i}{\hbar}\frac{e_0}{m_0}\mathbf{A}(t)\cdot\sum_{\mu}\left(\mathbf{\Pi}_{\mathbf{k}}^{\mu\lambda}x_{\mathbf{k}}^{\mu\lambda'} - \mathbf{\Pi}_{\mathbf{k}}^{\lambda'\mu}x_{\mathbf{k}}^{\lambda\mu}\right) - \frac{1}{T_{1/2}}x_{\mathbf{k}}^{\lambda\lambda'} \tag{3.18}$$

The homogeneous part of the SBE contains the band energies $\epsilon_{\mathbf{k}}^{\gamma}$ and $\epsilon_{\mathbf{k}}^{\gamma'}$ and represents the transition energies between band γ and γ' at reciprocal point $\mathbf{k}$. In this work the dephasing and relaxation processes in the material are described by phenomenological dephasing and relaxation times T_2 & T_1. In this form the SBE describe non-interacting particles since effects caused Coulomb interaction are omitted here.

The inhomogeneous part of the SBE describes the light-matter interaction which is here written in the velocity gauge $\mathbf{\Pi} \cdot \mathbf{A}$. The advantage of the velocity gauge is that the $\mathbf{k}$-points can be treated independently of each other. Using the eigenvectors $|\lambda, \mathbf{k}\rangle$ the momentum matrix elements are calculated via[50, 66]

$$\mathbf{\Pi}_{\mathbf{k}}^{\lambda\lambda'} = \frac{m_0}{\hbar} \langle \nabla_{\mathbf{k}} H(\mathbf{k}) \rangle_{\lambda\lambda'} . \tag{3.19}$$

In comparison the dipole gauge $\mathbf{d} \cdot \mathbf{E}$ contains gradient terms in the SBE, connecting $\mathbf{k}$ and $\mathbf{k}'$. The elements are connected by the simple relation $\mathbf{\Pi}^{\lambda\lambda'} = -\mathrm{i}\omega^{\lambda\lambda'} \mathbf{d}^{\lambda\lambda'}$. Due to the inconvenience that the wave function can have a random phase factor $\varphi_{\mathbf{k}}$ at each $\mathbf{k}$-point, a phase correction has to be made. Otherwise solving the SBE will lead to incorrect results.[65]

When solving the SBE as in Eq. (3.15a) all orders of the external electric field $\mathbf{E}$ are included in the equation of motion. With effects proportional to different orders of $\mathbf{E}$ all summed up together, a distinction between them can be difficult, especially if the orders have different magnitudes. To circumvent this problem, the SBE can be expanded powers of the external field $\mathbf{E}$. The expansion scheme has the form:

$$\begin{aligned}
\frac{\partial x^{(1)}}{\partial t} &\propto \Omega x^{(1)} + x^{(0)} \cdot E(t) \\
\frac{\partial x^{(2)}}{\partial t} &\propto \Omega x^{(2)} + x^{(1)} \cdot E(t) \\
\frac{\partial x^{(3)}}{\partial t} &\propto \Omega x^{(3)} + x^{(2)} \cdot E(t) \\
&\vdots \\
\frac{\partial x^{(n)}}{\partial t} &\propto \Omega x^{(n)} + x^{(n-1)} \cdot E(t)
\end{aligned} \tag{3.20}$$

The term $\Omega x^{(n)}$ stands for the homogeneous and $x^{(n-1)} \cdot E(t)$ for the inhomogeneous part of the SBE. For each order $x^{(i)}$, $i > 0$, the SBE have to be solved which leads to an increased numerical effort. The zeroth-order $x^{(0)}$ represents the starting condition of the system which normally refers to an unexcited semiconductor, i.e., no excited excitations or polarizations are present in the system. The advantage of this approach is that the different orders of $\mathbf{E}$ and consequently effects belonging to the corresponding orders are separated and can be analyzed individually. Here the expansion scheme is explain at the more intuitive example of an external electric field $\mathbf{E}$, but it can also be applied for the vector potential $\mathbf{A}$.

3.3 $\chi^{(2)}$ Photo Currents in Semiconductor Systems

The linear response of a semiconductor system to an external electric field is given by its susceptibility tensor χ:

$$\mathbf{P}(t) = \chi \cdot \mathbf{E}(t) \tag{3.21}$$

The polarization $\mathbf{P}$ can be expanded in powers of the external electric field $\mathbf{E}$. Each polarization of the nth-order has its specific susceptibility tensor $\chi^{(n)}$,

$$\mathbf{P}(t) = \sum_{i}^{\infty} \mathbf{P}^{(i)}(t) = \sum_{i}^{\infty} \chi^{(i)} \cdot \mathbf{E}^{i}(t). \tag{3.22}$$

Due to frequency mixing occurring in non-linear orders, the second-order susceptibility and therefore the system response can be further broken down into the different mixing possibilities

$$\mathbf{P}^{(2)}_{\omega_\Sigma}(t) = \chi^{(2)}(-\omega_\Sigma; \omega_\beta, \omega_\gamma)\mathbf{E}_{\omega_\beta}(t)\mathbf{E}_{\omega_\gamma}(t), \tag{3.23}$$

with $\omega_\Sigma = \omega_\beta + \omega_\gamma$. In non-centrosymmetric semiconductor systems the finite second-order optical susceptibility $\chi^{(2)}(0, \omega_g, \omega_g)$ allows the generation of optically induced electric currents using optical excitation with single frequency ω_g. It is noteworthy that the susceptibility tensor $\chi^{(2)}(0, \omega_g, \omega_g)$ can exist without applying an external bias, thus the photo current is created purely by the symmetry properties of the crystal. Because of different microscopic origins, one can distinguish between three different currents, the injection current $\mathbf{J}_{inj}$, the shift current $\mathbf{J}_{shift}$, and the rectification current $\mathbf{J}_{rec}$.[39]

The injection current $\mathbf{J}_{inj}$, also known as circular photogalvanic effect, arises from an asymmetric distribution of spin-polarized carriers in k-space. The asymmetric distribution of spin-carriers is due to spin-splitted bands caused by the

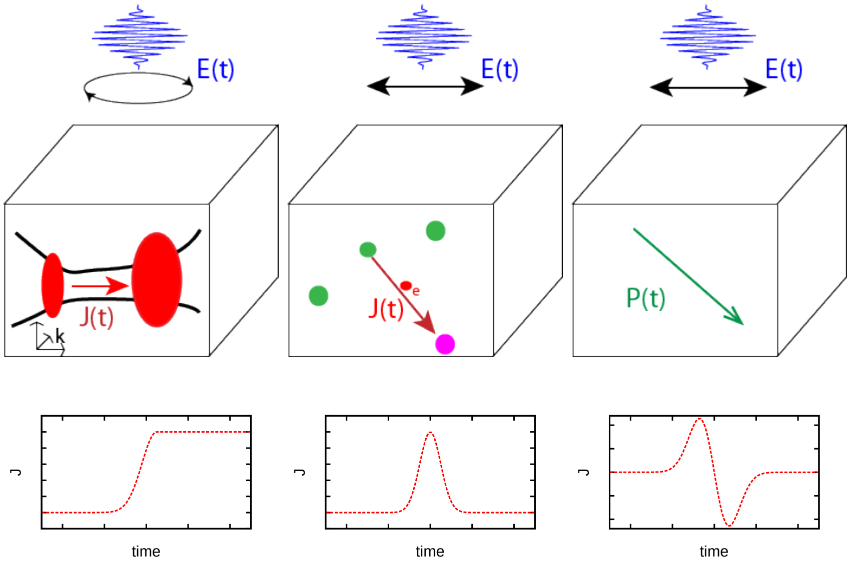

Figure 3.2: A schematic representation and comparison of the three photo currents, from left to right: injection, shift, and rectification current.
In the upper row depicted, the optical polarizations required for the excitation and the microscopic cause of each current. In the case of the injection current the circular polarized excitation causes an asymmetric distribution of carriers in **k**-space. For the shift current, the linear polarized excitation leads to a spatial movement of carriers from one atom to another. A linear polarized excitation also causes a static polarization in the material, the optical rectification. Known from Maxwell's equations that $\mathbf{J} \propto \dot{\mathbf{P}}$, the time derivative of the optical rectification is the rectification current.
In the lower row an idealized form of the currents as function of time. In a system without relaxation the injection current emerges with the optical excitation and remains constant afterwards. In the analytical limit of pure off resonant excitation, the shift current follows the square of the pulse envelope $E^2(t)$. The off resonant limit predicts for the rectification current that it follows the time derivative of envelope $\partial_t E^2(t)$.

Dresselhaus and/or Rashba effect in systems lacking spatial inversion symmetry. In this model $\mathbf{J}_{inj}$ is obtained from the populations in both conduction and valence band $n_{\mathbf{k}}^{\lambda} = x_{\mathbf{k}}^{\lambda\lambda}$ via

$$\mathbf{J}_{inj}(t) = \sum_{\lambda,\mathbf{k}} \mathbf{\Pi}_{\mathbf{k}}^{\lambda\lambda} n_{\mathbf{k}}^{\lambda}. \tag{3.24}$$

While bulk GaAs lacks inversion symmetry, the GaAs band structure is still inversion symmetric in $\mathbf{k}$-space due to the fact that the Schrödinger equation of the system still has to fulfill the time-reversal symmetry.[67] The inversion asymmetry instead lifts the spin degeneracy of the band structure. Only along the high symmetry lines (100) and (111) a spin degeneracy exists in bulk GaAs. The inversion symmetric of the band structure in bulk GaAs forbids the generation of an injection current, but in systems of further reduced symmetry like GaAs quantum wells a non-vanishing injection current may exist. Due to the required spin-polarized carriers, circularly polarized light is needed for the generation of an injection current.

The shift and rectification currents will be discussed at the beginning of Chapter 4 and Chapter 7, respectively.

3.4 Geodesic Grid

Looking at the symmetry, the point group T_d, the point group of a tetrahedron and the zincblende structure, is a subgroup of the point group O_h, the point group of a cube and the diamond structure. In practical manner, the zincblende structure is a derivation of the diamond structure. The diamond structure is derived by overlaying a face centric cubic (fcc) lattice with a second fcc lattice of the same atom basis, displaced by the vector $\frac{a_0}{4}(1|1|1)$ with a_0 being the lattice constant. The zincblende structure is obtained the same way, except that the second fcc lattice has a different atom basis. As a result of the different atom basis the zincblende structure lacks inversion symmetry. In point group terms this can be written as $O_h = T_d \otimes C_i$, with C_i being the group only including the identity and the inversion. A generalization of this idea by Lipari and Baldareschi [68] introduces that the cube symmetry is a sub group of the full rotation group R,

$$R \supset O_h \supset T_d. \tag{3.25}$$

The symmetry reduction manifests itself as new terms in the band structure of the respective subgroup. It is known that this new terms are small compared with the shared terms between the subgroups.[69] Based on this a symmetry hierarchy can be build for the Hamiltonian:

$$\hat{\mathrm{H}} = \hat{\mathrm{H}}_{sphere} + \hat{\mathrm{H}}_{cube} + \hat{\mathrm{H}}_{tetra} \tag{3.26}$$

For small $\mathbf{k}$-vectors around the Γ-point the Hamiltonian $\hat{\mathrm{H}}_{sphere}$ is the largest term. As a consequence, the band structure around the Γ-point can be described by a parabolic k^2 dispersion in good approximation.

When solving the SBE numerically, the continuous $\mathbf{k}$-space has to be discretized. A Cartesian grid is the easiest to implement, but based on the above mentioned symmetry considerations, a spherical $\mathbf{k}$-grid may be better suited for the discretization of the band structure. While a discretization based on spherical coordinates would be a candidate, spherical coordinates have the problem that the $\mathbf{k}$-points have a non-homogeneous distribution on the sphere surface. This leads to the well know problem of the increasing point density towards the poles resulting in a singularity at the poles themselves. Another type of spherical grid is the so-called geodesic grid which has a highly homogeneous point density on its surface. For this reason geodesic grids are often used when modeling the surface of a sphere, e.g. the surface of planet earth in global climate simulations.[70, 71] The starting point of a geodesic grid is a polyhedron, usually a convex regular icosahedron as seen in Fig. 3.3. The surface is further discretized using equilateral triangles. The final step is to project the new grid onto a sphere resulting in a very homogeneous distribution of points on the sphere surface.

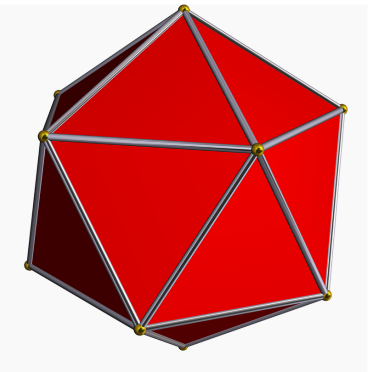

Figure 3.3: A convex regular icosahedron which is often used as a starting point in the construction of a geodesic grid. The picture is taken from the website *https://en.wikipedia.org/wiki/Icosahedron*.

In this work the geodesic grid has two essential parameters, the total number of used spheres N_R and the number of points on a sphere surface N_A. The total grid consists of several spheres, starting from a sphere with radius k_{min}. The spheres are placed with linear increasing radius until the last sphere with radius k_{max}. Depending on the problem the parameters k_{min} and k_{max} are either set by hand or determined by the program in such a manner that for a given central photon energy $\hbar\omega_L$ the band structure is properly resolved in **k**-space. The advantage of the later method is that for a fix number of **k**-points the grid can adjust itself to varying photon energies $\hbar\omega_L$ without losing much convergence for higher energies.

The product of $N_R \times N_A$ determines the total number of **k**-points in a simulation. This seems trivial, but it has the effect that the number of total **k**-points N_k is now linear in either N_R or N_A. In contrast, in a three-dimensional Cartesian grid the number of grid points growths cubic N^3, with N being the number of grid points per axis. This alone is a huge improvement for optimizing the resolution of a geodesic grid and will be of major importance for including the Coulomb interaction into the SBE, see Chapter 6.4.

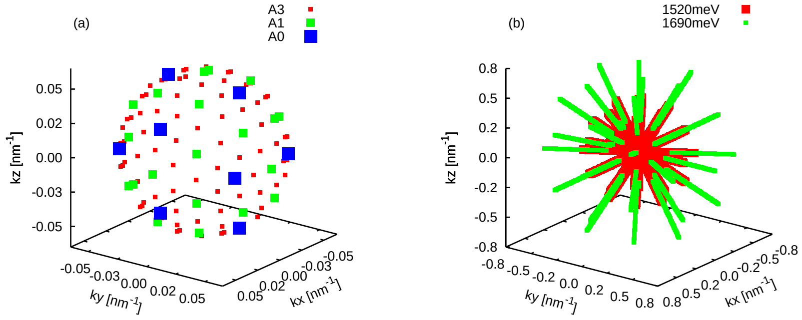

Figure 3.4: (a) A geodesic grid sphere in **k**-space. The labels A0, A1 and A3 stand for $N_A = 12$, $N_A = 48$, and $N_A = 162$ grid points per sphere surface, respectively. (b) Two geodesic grids with $N_R = 60$ spheres and $N_A = 48$ points per sphere. The grid parameters k_{min} and k_{max} are chosen in such a manner that the grid resolves the area of the band structure in which the transition from the valence band to the lowest conduction band is resonant to the optical excitation energy $\hbar\omega_L$. Displayed are two grids for an excitation energy of $\hbar\omega_L = 1520\,\text{meV}$ and $\hbar\omega_L = 1690\,\text{meV}$. As it can be seen, for $\hbar\omega_L = 1520\,\text{meV}$, 3 meV above the fundamental band gap of 1517 meV the grid fully encompasses the Γ-point. For $\hbar\omega_L = 1690\,\text{meV}$ the grid instead forms a sphere shell which does not include the Γ-point.

Chapter 4

Shift Currents in Bulk GaAs

The shift current $\mathbf{J}_{shift}$ is created by the motion of excited carriers in real-space during the moment of optical excitation. In inversion symmetric systems each microscopic current $\mathbf{j}$, which is caused by the movement of electrons from the valence band to the conduction band, has an anti-parallel current $-\mathbf{j}$ resulting in a zero net current $\mathbf{J} = 0$. In systems with spatial inversion asymmetry such as GaAs a microscopic current $\mathbf{j}$ can be created for certain optical polarizations while the corresponding anti-current $-\mathbf{j}$ is symmetry forbidden. The non-vanishing net current is the so-called shift current, one current responsible for the bulk photovoltaic effect.[17, 38]
In the combined approach of k.p theory and SBE the shift current $\mathbf{J}_{shift}$ is the $\omega = 0$ frequency component of the polarization current

$$\mathbf{J}_{pol}(t) = \sum_{\lambda,\lambda' \neq \lambda,\mathbf{k}} \mathbf{\Pi}_{\mathbf{k}}^{\lambda\lambda'} x_{\mathbf{k}}^{\lambda\lambda'}. \tag{4.1}$$

The polarization current $\mathbf{J}_{pol}$ is dominated by optically-induced first-order contributions with $\omega > 0$, whereas the shift current is a much smaller second-order effect. To obtain the shift current a Fourier frequency filtering method is applied, see Fig. 4.1.

This Chapter begins by confirming that the combined approach is indeed suitable to describe shift currents in bulk GaAs. After the confirmation, a comparison between a standard Cartesian and a geodesic grid is made, focusing on the convergence properties. Afterwards, the shift current is investigated regarding non-linear effects like Rabi-flopping and coherent control properties.

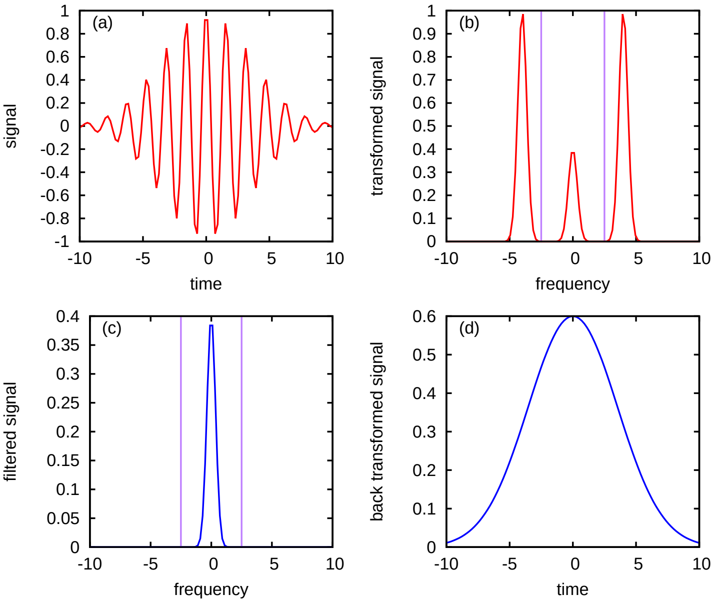

Figure 4.1: (a) To separate the shift current $\mathbf{J}_{shift}$ from other contributions in $\mathbf{J}_{pol}$ a Fourier transformation $\mathcal{F}$ is performed on the full signal. (b) In frequency domain a filter is applied on $\mathbf{J}_{pol}(\omega)$ around $\omega = 0$ which removes higher frequency components. (c) The so obtained signal in frequency space is back transformed $\mathcal{F}^{-1}$ to the time domain. (d) The calculated current is the shift current $\mathbf{J}_{shift}(t)$.

4.1 General Shift Current Properties

For the simulations of the shift current first the band structure and momentum matrix elements are obtained by matrix diagonalization of the extended Kane Hamiltonian $\hat{\mathrm{H}}(\mathbf{k})$. The eigenvalues $\epsilon_{\mathbf{k}}^{\lambda}$ form the band structure while eigenvectors $|\lambda, \mathbf{k}\rangle$ are used in the calculation of the momentum matrix elements via Eq. (3.11). With the band structure and the matrix elements the time evolution of the optically induced coherencies and polarizations in the system can be simulated via the SBE. The shift current $\mathbf{J}_{shift}$ is obtained after applying a frequency filter on the calculated polarization current $\mathbf{J}_{pol}$.

Fourier transformations at $\omega = 0$ are prone to numerical unphysical artifacts due to numeric difficulties. To see if the calculated currents are indeed shift currents, and consequently, to confirm that the combined method of k.p theory and SBE is viable to describe the shift current $\mathbf{J}_{shift}$, the symmetry properties of the calculated current are tested and compared with the known properties for bulk GaAs. In addition, the scaling of shift current is analyzed to see if it confirms the second order nature of the shift current.

4.1.1 Symmetry Analysis

In zincblende type crystals like GaAs the lack of inversion symmetry allows for the existence of a non-vanishing shift current. In order to generate a shift current the optical linear polarization has to fulfill the symmetry conditions of the crystal structure. In GaAs four gallium atoms form a tetrahedron around one arsenic atom in its center and vice versa, see Fig. 4.2. Setting the arsenic atom is in the origin of the coordinate system, the coordinates of the four gallium atoms are (1|1|1), (-1|-1|1), (1|-1|-1) and (-1|1|-1). Is the system excited with a linear polarization parallel to one of the crystallographic axis, (100), (010) or (001), the electron has an equal transition probability to all four neighbor atoms and on average the individual micro-currents will cancel out each other resulting in a zero-net shift current.

For (110)-polarization the transitions to (1|1|1) & (-1|-1|1) are viable while (1|-1|-1) & (-1|1|-1) are orthogonal to the light field. While the x- and y-components still cancel out each other, the z-component now has a preferred propagation direction resulting in a non-vanishing net current in z-direction, see Fig. 4.3. For the case of low excitation intensities the shift currents in GaAs follow the envelope of the incident pulses due to off-resonant excitation being

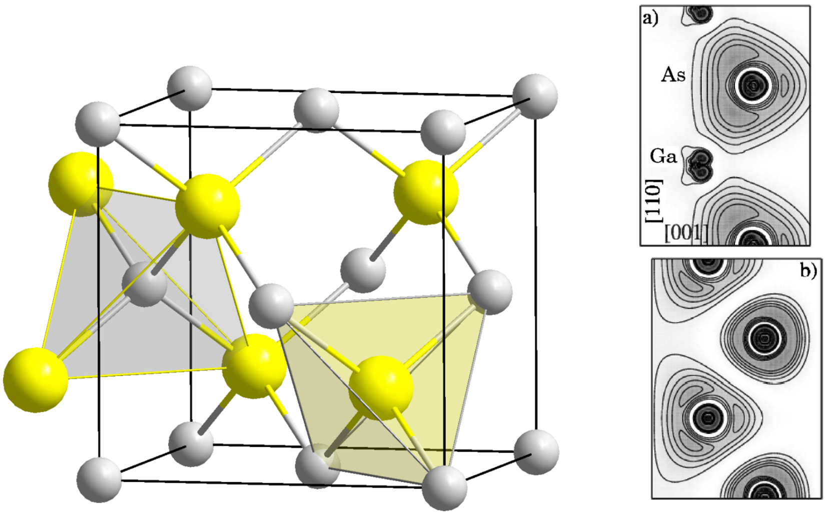

Figure 4.2: Left: The zincblende crystal structure with its two different sorts of atoms. In GaAs the larger yellow atoms represent arsenic and the smaller gray atoms represent gallium. As illustrated in the figure each atom is surrounded by 4 atoms of the other sort forming a tetrahedron. The picture is taken from the website *en.wikipedia.org/wiki/Zinc_ blende*.
Right: The electron density in GaAs in a [110] lattice plane. In a) the electron density for the highest valence band is depicted in the ground state. The electron density is localized around the arsenic atoms. In b) the electron density for the lowest conduction band is depicted after the system was optically excited with a photon energy larger than the band gap. The electron density is now localized also around the gallium atoms, taken from [39].

involved. The shift current is described by

$$J^z(t) = \sigma_{xyz} E^x(t) E^y(t), \tag{4.2}$$

with σ_{xyz} being the response tensor of GaAs and $E^x(t)$ and $E^y(t)$ are the pulse envelopes. For GaAs and other zinkblende structures the response tensor has only non-vanishing elements for the xyz-combination and its permutations.[72]

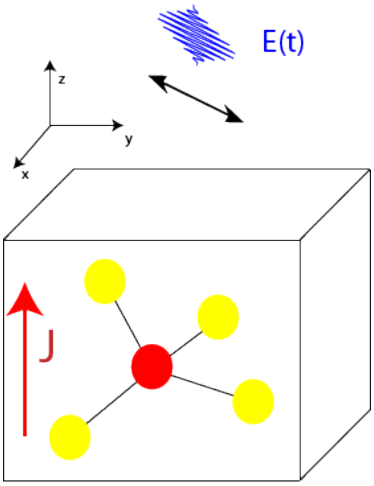

Figure 4.3: Schematic illustration of the simulated setup. The bulk crystal is excited with a linear polarized light, here in (110)-direction, which generates a shift current in (001).

Based on the symmetry properties, Eq. (4.2), shift currents only exist for xyz-combinations and its permutations. In Fig. 4.4 the respective J_x, J_y, and J_z currents are calculated for an array of polarizations. For linear polarizations parallel to the crystallographic axis the symmetry properties forbid a shift current. But the corresponding currents, the diagonal in Fig. (4.2), show a non-zero current flowing in the polarization direction. For the diagonal polarizations, off-diagonal currents in Fig. (4.2), the simulations show currents flowing in the directions of the applied electric fields. The predicted perpendicular shift currents are zero on this scale. The parallel flow and small visible oscillations lead to the assumptions that these are artifacts caused by the first-order polarization which is magnitudes larger than the second-order polarization. Even with the application of a frequency filter, the Lorentzian decaying contributions of the first-order are still larger at $\omega = 0$ than the second-order contributions.

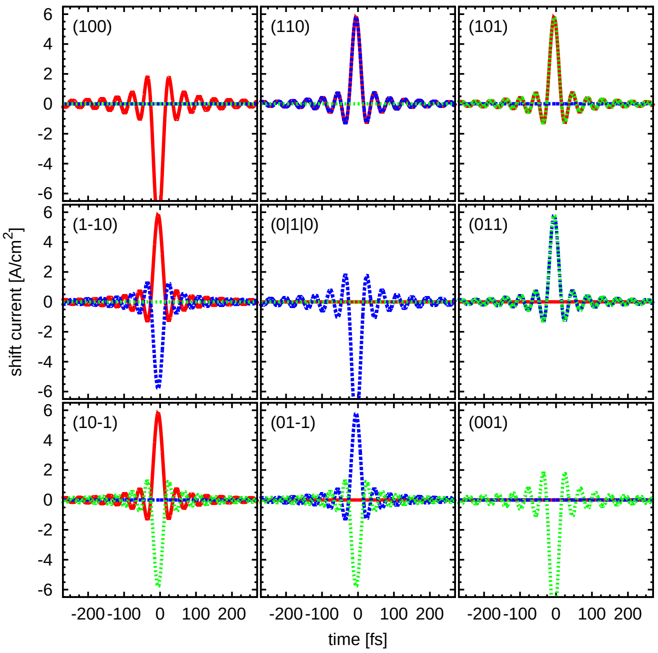

Figure 4.4: Bulk GaAs is excited with a linearly polarized Gaussian pulses, FWHM $2\Delta t = 200\,\mathrm{fs}$, peak intensity $I_0 = 0.1\,\mathrm{W/cm^2}$ and central frequency $\hbar\omega_L = 1.617\,\mathrm{meV}$ which lies $100\,\mathrm{meV}$ above the fundamental band gap $E_g = 1.517\,\mathrm{eV}$. Shown are the created currents in x, y, and z-directions for varying linear polarizations, color marked red, blue, and green, respectively. The columns represent the polarizations of the first electric field component E_i^1 while the rows represent the second field component E_j^2. The shift currents are obtained by solving the SBE. The simulations parameters are $T = 0.1\,\mathrm{K}$, $T_1 = T_2 = 100\,\mathrm{fs}$.

To test the assumption that the visible currents in Fig. 4.4 are numerical artifacts, the currents are simulated by the SBE in an order expansion up to second-order in the optical field. In Fig. 4.5 only the second-order currents are displayed. On the diagonal no currents are visible for linear polarizations parallel to the crystallographic axis. This is in agreement with the GaAs symmetry and confirms that the previous visible currents are caused by first-order contributions. For the diagonal polarization on the off-diagonals in Fig. 4.5 Gaussian-shaped currents perpendicular to the corresponding optical polarization are visible while the parallel currents vanish. In addition, the in-plane orthogonal polarization, e.g., (110) to (1-10), creates a shift current in the respective opposite direction which is expected by the tetrahedron symmetry.

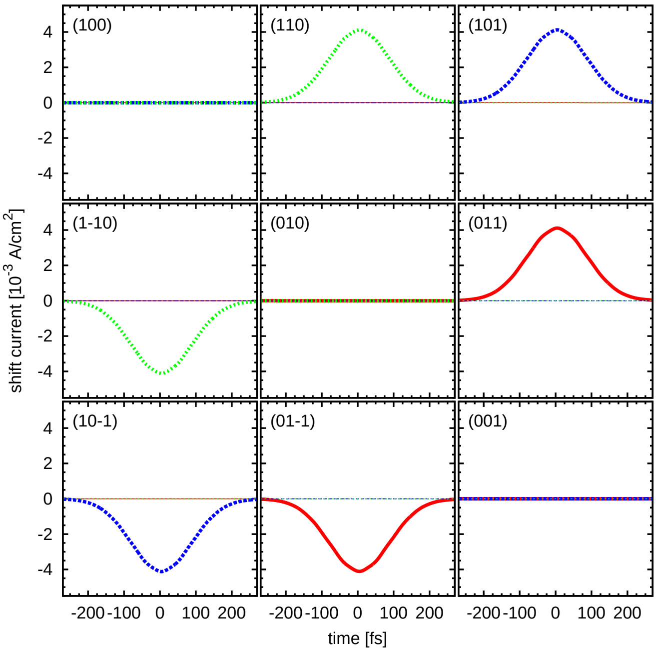

Figure 4.5: The simulation setup is identical to Fig. 4.4. Instead of solving the SBE for the full electric field, a second-order expansion in the electric field is done. Shown are the second-order currents in x, y, and z-directions in red, blue, and green, respectively.

4.1.2 Second-Order Analysis

From the expansion scheme it is known, that charge carrier populations in the band structure are at minimum second-order effects. The shift current is created by the spatial shift of real carriers, i.e., electrons have to be lifted from the valence band to the conduction band. With the shift current being associated with the creation of charge carrier populations, it has to be at minimum a second-order effect too. Consequently, for low intensities, Eq. (4.2), it is expected that the shift current scales linearly with E^2, i.e., the intensity I_0.

In Fig. 4.6 the shift current is simulated for increasing excitation intensities I_0. The shift current scales linearly and follows the Gaussian form of the exciting pulses for low intensities in the $\frac{\mathrm{mW}}{\mathrm{cm}^2}$-range up to high intensities in the $\frac{\mathrm{MW}}{\mathrm{cm}^2}$-range. Starting at $I_0 = 10\,\frac{\mathrm{GW}}{\mathrm{cm}^2}$ the shift current deviates from the low intensity behavior and shows saturation effects. The temporal shape of the current also deviates from the Gaussian shape and has a more complex dynamic. This will be analyzed more in detail in Chapter 4.5.

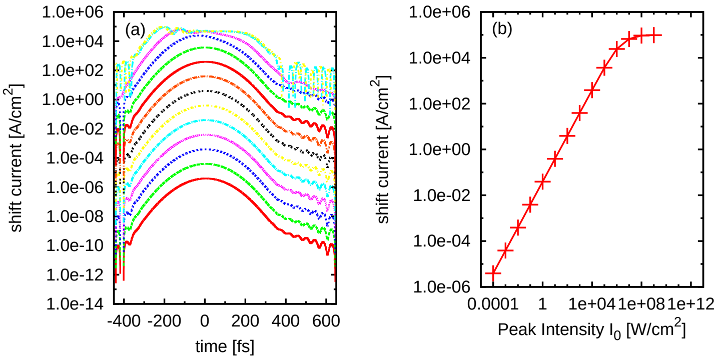

Figure 4.6: Left: Logarithmic plotting of the shift current for different excitation intensities I_0. Starting from the smallest peak intensity $I_{min} = 10^{-4}\,\frac{\mathrm{W}}{\mathrm{cm}^2}$ the shift current is simulated for a Gaussian pulse with in powers of 10 increasing peak intensities until $I_{max} = 10^8\,\frac{\mathrm{W}}{\mathrm{cm}^2}$. Right: Peak shift current as function of peak intensity I_0, both axis are in logarithmic scale.

It is shown that the simulated shift currents do follow the symmetry rules of GaAs and are of second-order nature in the low intensity range. Therefore the combined approach of k.p-theory and SBE in the velocity gauge is indeed suitable for the description of shift currents in bulk GaAs.

4.2 Shift Current in a Geodesic Grid

A discretization of **k**-space, which takes into account that around the Γ-point the band structure has a high spherical symmetry, could be advantageous for the numerical evaluation of the SBE, mainly due to the reduced number of required **k**-points for a converged result, see Chapter 3.4. In this section the convergence behavior of the a geodesic grid is analyzed and compared to a standard Cartesian grid.

For the Cartesian case a cubic grid with 21 points per axis, i.e. $N_k = 21^3 = 28781$ points, is used. It has the Γ-point at its center and its width is $2k_{max}$, with the parameter k_{max} being largest k-value per axis. For better comparison the convergence of a Cartesian grid is also a point of interest. Shift currents are simulated for different point densities, achieved by varying the parameter k_{max}.

For the geodesic case a grid is used with the smallest radius $k_{min} = 0$ and the largest radius $k_{max} = 0.45\,\mathrm{nm}^{-1}$. Unlike the Cartesian grid, the geodesic grid has two parameters, the amount of spheres N_R and the points per sphere N_A. Thus a set of simulation with fix sphere number $N_R = 31$ and varying number of point per sphere N_A is done and vice versa. The parameters of the Cartesian simulations, labeled C, for the the geodesic simulations with constant sphere number, labeled GA, and for constant points per sphere, labeled GR, can be found in table 4.1. It should be noted that the largest geodesic grids, GA4 & GR4, have with 7812 and 4692 points still less than half the points of the Cartesian grid. The smallest grid, GA1 & GR1, have with 1302 and 1932 points even less than 10% of the Cartesian grid.

Table 4.1: Cartesian and Geodesic Grid Parameters

$d_k = 31$	C1	C2	C3	C4
$k_{max}[nm^{-1}]$	0.6	0.5	0.4	0.3

$N_R = 31$	GA1	GA2	GA3	GA4
A_n	42	92	162	252

$A_n = 92$	GR1	GR2	GR3	GR4
N_R	21	31	41	51

The simulation using a Cartesian grid, C1-C4, as well as the geodesic grids, GA1-GA4 and GR1-GR4, in Fig. 4.7 show overall good convergence behaviors. Close-ups of the currents reveal a small time delay of the peak current, showing that the maximum lies at $J(t \approx 5\,\mathrm{fs})$. Also a small oscillation is visible at the end of the shift current $J(t \approx 260\,\mathrm{fs})$, deviating slightly from the analytic $E(t)^2$

form. Both are explained by small resonant contributions to the shift current and by the small asymmetry in the number of oscillators between $\omega_g - \omega_\Delta$ and $\omega_g + \omega_\Delta$ which are excited by the finite line width of the Gaussian pulse. The asymmetry is due to the density of states $D(\omega)$ increasing with $\sqrt{\omega}$ for a bulk band structure.

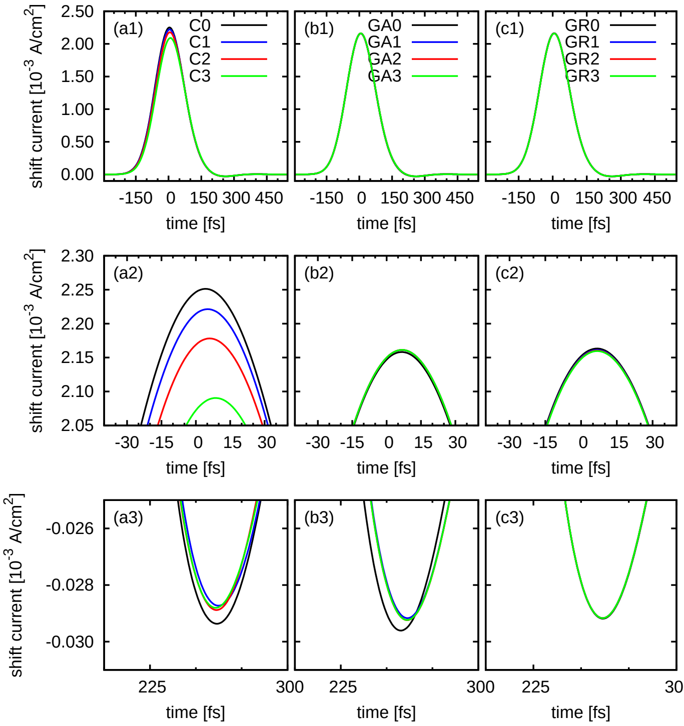

Figure 4.7: Shift currents for a Cartesian grid, column (a), and two geodesic grids, column (b) & (c). In row (1) the whole current is displayed, while row (2) and row (3) are close-up of the maximum and the small oscillation at the end of the shift currents, respectively. The system is excited by a Gaussian pulse, FWHM $2\Delta t = 150\,\text{fs}$ and central frequency of $\hbar\omega_L = 1.550\,\text{eV}$. The simulations parameters are $T = 0.1\,\text{K}$, $T_1 = T_2 = 100\,\text{fs}$.

In the case of the Cartesian grid, the close-up of the peak current reveals that a Cartesian grid overestimates the shift current for a low density of grid points. The close-up of the small oscillation also shows an overestimation but to a smaller degree. With increasing density the convergence improves, simulation C3 having the best convergence. For higher densities, simulation C4, the shift current is now slightly underestimated. A picture of the excited carrier population in the conduction band, Fig. 4.8, shows that simulation C3 has a good discretization of the excited region. Simulation C4 has an even better resolution but cuts of parts of **k**-space which have still small contributions to the shift current. Consequently, besides having the very disadvantageous cubic scaling of grid points, a Cartesian grid also has the problem of properly choosing the grid boarders to ensure a proper resolution of the relevant **k**-space as well as not cutting of still contributing regions of **k**-space. The simulations were done for a photon energy of $\hbar\omega_L = 1.550\,\mathrm{eV}$, still in a region relatively close to the Γ-point. For higher photon energies a higher number of grid-points would be required to ensure good converged results. Due to the cubic scaling this results in drastic increase of computational time.

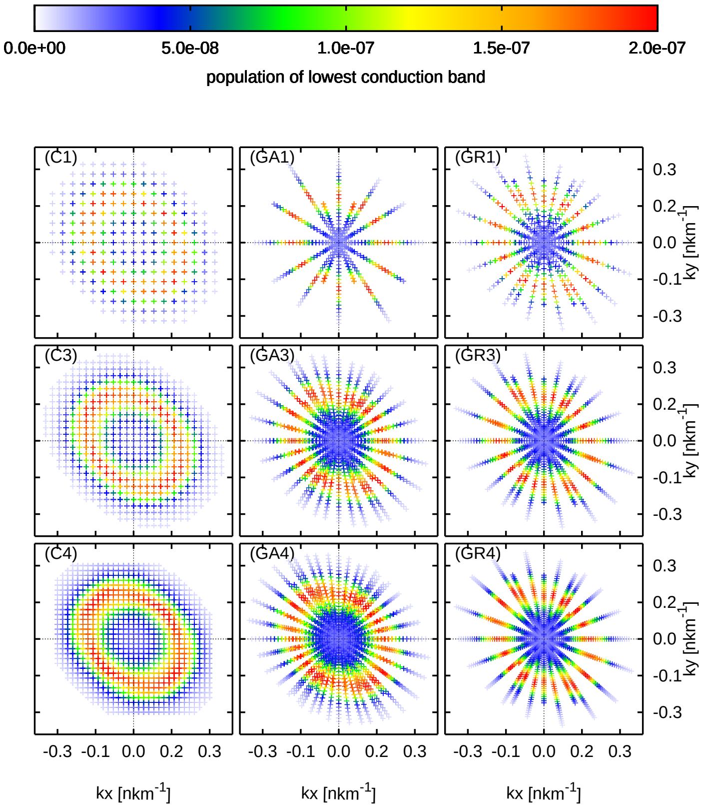

Figure 4.8: Cross-section of the lowest conduction band. Displayed is the population $n(\mathbf{k}) > 0.1 \cdot 10^{-9}$ at the time $t = 0$ for all **k**-points with $|k_z| < 0.1\,\mathrm{nm}^{-1}$. On the left the Cartesian grids C, in the middle and right the geodesic grids GA & GR.

For the geodesic grid the close-up of the peak current in Fig. 4.7 shows an extremely high convergence. With the same resolution as for the Cartesian case, the geodesic results are almost identical. For the small oscillation small differences can be seen for the geodesic grids with varying points per sphere, but overall a high convergence behavior is displayed. This means that even the two smallest geodesic grids, GA1 & GR1, have a better resolution of the important parts of **k**-space than a Cartesian grid with 10 times more points.

Given that the geodesic parameters k_{min} & k_{max} can be adjusted to only resolve the important areas of **k**-space and that a geodesic grid scales linear in sphere number N_R or number of point per sphere N_A, simulations for higher photon energies can be done without or only a small increase of computational time. The high convergence behavior and the advantageous numeric properties makes a geodesic grid better suited than a Cartesian grid for most excitation conditions. Thus the geodesic grid is used for the remaining shift current simulations in bulk GaAs.

4.3 Photon Energy Dependence

The shift current represents the spatial movement of electrons caused by optical excitation. For below band gap excitation no electrons are lifted from the valence band to the conduction band and consequently no shift current should exist. For above band gap excitation the amount of excitable electrons increases with the photon energy due to the growing density of states. This should reflect itself in a growing shift current strength as function of the excitation energy $\hbar\omega_L$.

In Fig. 4.9 (a) the currents for a photon energy of $\hbar\omega_L = 1.48\,\text{eV}$, $\hbar\omega_L = 1.52\,\text{eV}$, and $\hbar\omega_L = 1.57\,\text{eV}$ are shown. The red current, 27 meV below the band gap, does not follow the Gaussian E^2 envelope and is in comparison to the two other currents very small. This current is not a shift current, but an off-resonant contribution to the $\omega = 0$ signal created by the small off-resonant overlap of the Gaussian pulse with the finite line width of the band structure. The green current, 3 meV above the band gap, follows the E^2 envelope, but its peak is slightly before $t = 0$. The spectral width of the excitation pulse contains above band gap contributions, responsible for the shift current, as well as below band gap contributions, responsible for the slight shift of the current maximum. The blue current, 43 meV above the band gap, follows the Gaussian E^2 envelope shape. The spectral width of the optical pulse is fully resolved in the band structure and thus does not contain below band gap contributions.

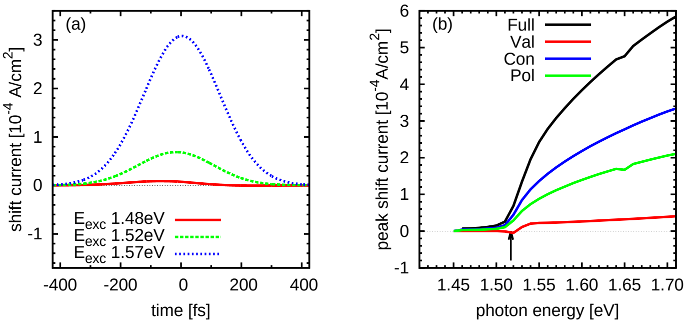

Figure 4.9: In (a) three currents are shown for three different photo energies, below, above and far above the band gap $\hbar\omega_{gap} = 1.517\,\text{eV}$; FWHM $2\Delta t = 150\,\text{fs}$. In (b) the peak shift current is shown as function of the central photon energy $\hbar\omega_L$ of the Gaussian pulse. In addition, the individual contributions of the valence & conduction band as well as the interband polarization are shown which add up to the full shift current.

In Fig. 4.9(b) the peak current is plotted as function of the central photon energy $\hbar\omega_L$. For below band gap excitation only a very small current exists due to the overlap of the pulse with the finite line width of the band structure. For above band gap excitation the shift current follows a

$$J_{peak}(\omega) \propto \sqrt{\hbar\omega} \tag{4.3}$$

pattern, which shows that the shift current mirrors the density of states. This is in agreement with the interpretation of the shift current as movement of excited electrons. At this point it has to be mentioned that the results here were calculated without Coulomb effects and thus excitonic effects, which are present at the band gap, are not included. The influence of excitonic effects on the shift current will be discussed in-depth in Chapter 6.

Besides the full shift current $\mathbf{J}_{shift}(t)$ also the individual contributions of the valence & conduction band as well as the interband polarization are shown. The comparison shows that the conduction band has the largest contribution to the shift current while the valence band has the smallest. The valence band contribution remains relatively flat as function of the photon energy, displaying only a slight increase in comparison with the other contributions. In the full current a small dip of the peak shift current is visible at $\approx 1.65\,\text{eV}$ which is caused by a dip in the interband contribution at the same position. The energy distance to the band gap is comparable to the energy gap between the two highest conduction bands $\Delta_0' = 0.171\,\text{eV}$.

4.4 Shift Current Band Analysis

As previously demonstrated in Chapter 4.1.1, the origin of the shift current can be traced back to the inversion asymmetry of GaAs. In the extended Kane model specifically three parameters are the result of the inversion asymmetry in the zincblende structure and do not exist in the corresponding inversion symmetric diamond structure. They are the parameter Δ^-, an interband coupling in $\hat{\mathrm{H}}_{7c7v}$, the parameter P', the inter-subband coupling strength of the conduction bands in $\hat{\mathrm{H}}_{8c6c}$ and $\hat{\mathrm{H}}_{7c6c}$, and the parameter C_k, an intra-band and intra-subband coupling factor in $\hat{\mathrm{H}}_{8v8v}$ and $\hat{\mathrm{H}}_{8v7v}$. By switching of these parameters the band contributions of specific bands can be studied.

In Fig. 4.10(a) the shift current in normal GaAs, T_d symmetry, is compared with an artificial inversion symmetric GaAs, O_h symmetry. The direct comparison shows that in the artificial O_h symmetry the shift current vanishes which is in agreement with its microscopic symmetry explanation. The small non-zero signal in the O_h symmetry is due to an inter-subband polarization between the heavy and light hole band which has a spectral range of 20 meV and lies in the energy range of the applied frequency filter.

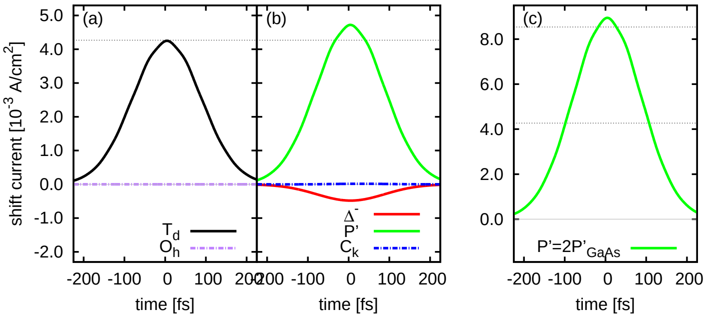

Figure 4.10: Dynamics of the shift current $J^z(t)$ excited by a laser pulse with linear (110)-polarization and FWHM $2\Delta t = 100\,\mathrm{fs}$. (a) Comparison between the full extended Kane model with T_d and O_h symmetry. In the O_h symmetry calculations the parameters Δ^-, P', and C_k have been set to zero. (b) Simulations where only Δ^-, P', or C_k is non-zero, respectively. (c) Simulation with parameter P' set to twice of the normal value for GaAs.

In Fig. 4.10(b) the individual contributions of the three parameters are studied. The parameters Δ^- and C_k have small contributions to the shift current which actually have the shift current flow in the opposite direction. The parameter P' has by far the largest contribution to the shift current. An artificial doubling of its value in Fig. 4.10(c) leads to an increased shift current slightly larger than twice its original value. This shows that the non-resonant conduction bands $|8c\rangle$ and $|7c\rangle$, which are coupled by P' to the lowest conduction band, are mainly responsible for the shift current in GaAs.

4.5 Rabi Flopping

In Sec. 4.1.2 it is shown that the low intensity E^2 scaling remains valid even for large intensities up to the $\frac{\mathrm{GW}}{\mathrm{cm}^2}$-range. For higher intensities the shift current diverges from the E^2 scaling and shows saturation. As known from a simple two level system, high excitation intensities lead to a large transition of electrons from the valence state to the conduction state, eventually causing population inversion where more electrons are in the conduction state than in the valence state. Once population inversion is reached optical excitation now leads to stimulated emission, transferring an electron from the conduction state down to the valence state. The intensity dependence of injection currents in quantum well systems has been investigated previously and it was confirmed that the direction of the charge flow change due to population inversion.[23, 27] Given that the shift current is created by spatial motion of carriers, for the case of population inversion the shift current should logically flow in the reversed direction. To achieve population inversion extremely high excitation intensities are used in the simulations and dephasing and relaxation are neglected to maximize the coherent effects.

In Fig. 4.11(a)-(c) and Fig. 4.12(a)-(c) the angle integrated population density of the conduction band $n(|\mathbf{k}|)$ is shown as a function of time. After the pulse two population traces are visible in Fig. 4.11(a) which stems from the heavy and light hole transitions, both within the spectral width of the excitation pulse, are resonant at different $|\mathbf{k}|$. While corresponding shift current, Fig. 4.11(d), shows now sign of current reversal, with the exception of a small oscillation caused by the intra-band coherence between heavy and light hole, the small shift of the peak current to negative times indicates saturation effects. With increasing excitation intensity the shift current in Fig. 4.11(e) now undergoes a clear current reversal. This coincides with heavy hole trace, $|\mathbf{k}| \approx 23\,\mathrm{nm}^{-1}$, vanishing in the integrated population density in Fig. 4.11(b). This means that during the excitation the population of the heavy hole has undergone a Rabi-flop which is reflected by the sign change of the shift current. The remaining light hole trace at $|\mathbf{k}| \approx 18\,\mathrm{nm}^{-1}$ shows that heavy and light hole have different transitions strength and thus contribute to the shift current reversal at different times which makes a one-to-one correlation between population and shift current difficult.

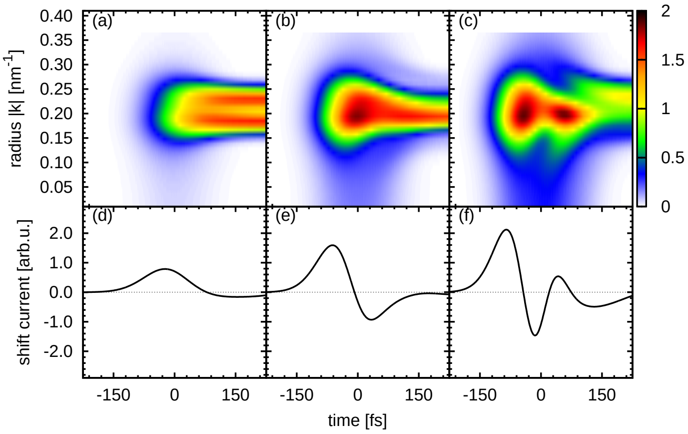

Figure 4.11: The upper row (a)-(c) shows the dynamics of the angle-integrated population n over the radius $|\mathbf{k}|$ in the conduction band for intensities (a) $I = 0.06\,\mathrm{GW/cm^2}$, (b) $I = 0.22\,\mathrm{GW/cm^2}$, and (c) $I = 0.48\,\mathrm{GW/cm^2}$, respectively. Because of summing over spin ↑ and ↓ the density reaches 2 as a maximal value. In the lower row (d)-(f) the corresponding dynamics of the currents $J^z(t)$ are displayed. The results where published in [73].

This becomes more evident in Fig. 4.11(c) where the excitation pulse has now such a high intensity that the heavy hole trace completes a full Rabi cycle and starts a new cycle at the end of the excitation pulse. In comparison the light hole trace almost completes its second Rabi cycle. The corresponding shift current in Fig. 4.11(f) also displays two Rabi cycle with the first cycle being a considerable amount larger than the second cycle.

In Fig. 4.12 displayed are the population dynamics and the shift currents for even higher excitation intensities. With increasing excitation intensity the amount of Rabi cycles and the Rabi frequency increases in the population, (a)-(c), as well as corresponding shift currents, (d)-(f). In Fig. 4.12(c) and Fig. 4.12(f) three full Rabi oscillations in the population as well as in the shift current are visible.

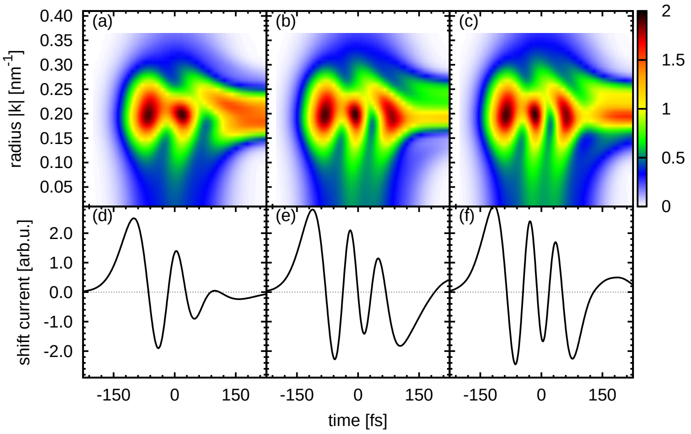

Figure 4.12: Analogous to Fig. 4.11, Rabi oscillations in the angle-integrated population n, (a)-(c), and the corresponding shift currents, (d)-(f), for intensities (a) $I = 0.85\,\mathrm{GW/cm^2}$, (b) $I = 1.33\,\mathrm{GW/cm^2}$, and (c) $I = 1.61\,\mathrm{GW/cm^2}$, respectively. The results where published in [73].

4.6 Coherent Control of Shift Currents

Using two or more light pulses, it is possible to control dynamic processes in a variety of systems. Experimental and theoretical research on coherent control was done on quantum dots, excitons in quantum wells, centro-symmetric bulk semiconductors and even for currents at metal surfaces.[74–77] In this section a brief investigation about the coherent control properties of shift currents is done for chirped pulses and two pulse excitation with a delay time τ.

4.6.1 Chirped Pulse Excitation

As shown by A. M. Racu et al. the dynamics of the shift current can be controlled by application of optical excitation with chirped pulses.[78] A chirped pulse is a pulse with a time-dependent frequency $\omega(t)$. By introducing a temporal delay δ_t between two incident chirped pulses the different frequency components of the electric fields interfere and causes the shift current, normally a direct current (DC), to acquire alternating current (AC) contributions.

Two chirped Gaussian pulses, one polarized in (100) and the other in (010)-direction, are considered to qualitatively reproduce the chirp-induced ac contributions. The pulses have a central frequency $\omega_L = 1.55\,\frac{\mathrm{eV}}{\hbar}$ and a fixed linear chirp $\omega(t) = \omega_L + \delta\omega \cdot t$, $\delta\omega = \pm 0.5\,\frac{\mathrm{meV}}{\hbar\mathrm{fs}}$. The shift current is simulated for varying time delay δ_t between the two incident pulses. For negative, Fig. 4.13(a),

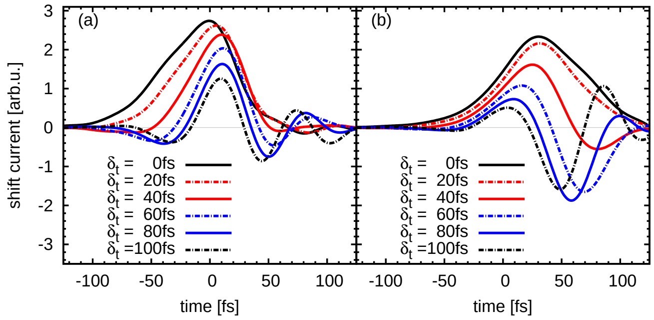

Figure 4.13: Dynamics of the shift current $J^z(t)$ excited by chirped laser pulses with (100) and (010)-polarization directions. Shown are shift currents for different pulse delays δ_t between the incident two laser pulses for negative (a) and positive (b) chirp. The results where published in [73].

and positive chirp, Fig. 4.13(b), the shift current dynamics change significantly with the time delay δ_t. As in the experiment the AC contribution increase with longer delay times δ_t, showing no AC contributions for $\delta_t = 0$. For a negative chirp the peak current positions remains around $t = 0$. In comparison, for a positive chirp the peak current changes sign due to the growing AC-components and shifts to later t-times. This is also in agreement with experimental observation. The qualitative agreement between experiment and theory reaffirms the strength of the combined microscopic theory of k.p and SBE to accurately describe shift currents in GaAs.

4.6.2 Two-Pulse Phase Control

With the exception of very high intensities seen at the example of Rabi flopping, the shift current excitation is a second-order process. In the first-order the generation of the shift current requires above band gap excitation. An identical pulse with a relative phase of π will cause an extinction of a first-order polarization excited by a previous pulse, see Fig. 4.14. But in second-order the off-resonant higher conduction bands are involved in the creation of the shift current. Therefore, the second-order shift current response may differ due to the required off-resonant excitations. In this section the coherent control properties of the shift current are analyzed. The system is excited directly at the band gap by two Gaussian pulses at times $t_0 = 0$ and τ, with (110)-polarization & FWHM $2\Delta t = 50\,\text{fs}$. To ensure that the two pulses are not directly interfering, the time delay τ is chosen to be large enough so that the electric fields of the two pulses do not have a temporal overlap, unless stated otherwise $\tau = 800\,\text{fs}$. In addition dephasing and relaxation are turned off to maximize the coherent control effects present in the shift current.

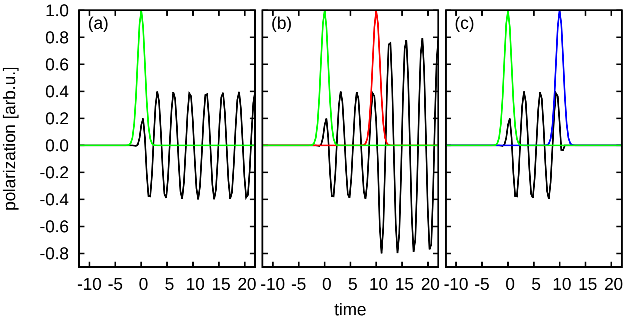

Figure 4.14: The coherent control scheme: (a) An optical pulse creates an polarization in the material at time $t = 0$. (b)A second optical pulse at $t = \tau$ has a relative phase of 2π which creates a constructive interference with the previously excited polarization. (c) The second optical pulse at $t = \tau$ has a relative phase of π which results in a destructive interference.

A pulse with a relative phase of φ can either cause a strong enhancement or an extinction of the first-order polarization. In Fig. 4.15(a) the corresponding shift current response is displayed and shows only a small modification of the shift current by the second pulse. The shift current amplitudes at time τ varies around the height of the first peak and remains in the same magnitude as the first shift current at $t = 0$. With a phase of $\varphi = 0$ the second shift current peak is smaller than the first peak while for a phase of $\varphi = \pi$ the second peak is larger. A phase resolved look at the second peak amplitude in Fig. 4.15(b) shows that the shift current follows sine/cosine dependence. Unexpectedly, the shift current displays an intrinsic phase factor of approximately $\frac{1}{4}\pi$ in its dependence. In addition, the minimum of the amplitude is around $\varphi = 0$, which is in contrast to the known linear response which would display the minimum at $\varphi = 1\pi$.

Further analysis in Fig. 4.16 reveals that the effect also depends on the photon energy and that the intrinsic phase factor differs depending on the photon excitation energy $\hbar\omega_L$. In Fig. 4.16 (a) & (b) the peak current shows a sine dependence with an intrinsic shift of $\frac{1}{4}\pi$ in (a) and $-\frac{1}{4}\pi$ in (b). This indicates that unlike in a two level system, which only has one transition energy, the different transition energies present in a band structure are responsible for this effect.

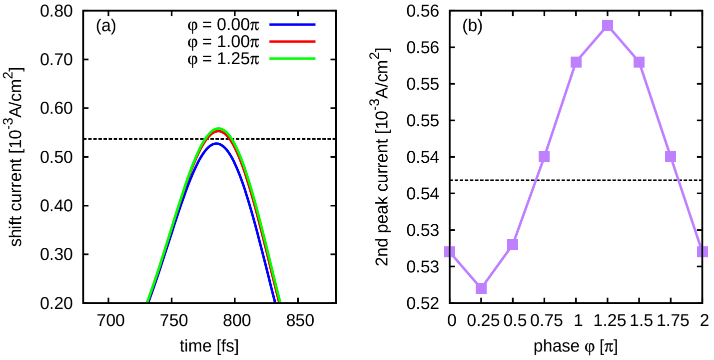

Figure 4.15: The shift current generated by two optical pulses at times $t = 0\,\text{fs}$ and $\tau = 800\,\text{fs}$. (a) Displayed is the second shift current peak. The second pulse has the phase $\varphi = 0$, $\varphi = 1\pi$, and $\varphi = 1.25\pi$ in respect to the first pulse. (b) The peak amplitude of the current generated by the second pulse as function of phase φ. The black dashed line in (a) & (b) is the height of the first peak.

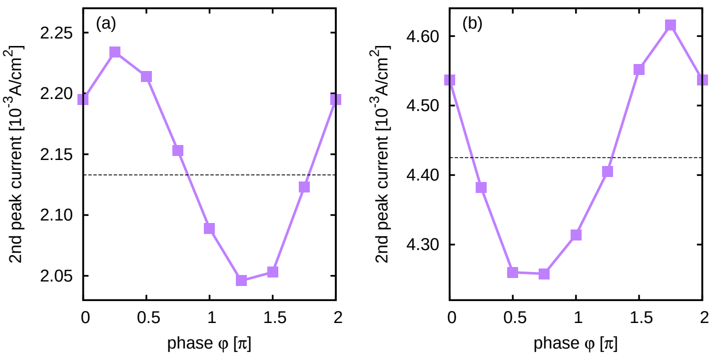

Figure 4.16: As in Fig. 4.15(b), the peak amplitude of the shift current generated by the second pulse is displayed with a photon energy of (a) $\Delta\hbar\omega_L = 30\,\text{meV}$ and (b) $\Delta\hbar\omega_L = 100\,\text{meV}$ above the fundamental band gap.

To find the reason for this behavior, especially the intrinsic phase, an order expansion into field components is applied. Starting with the SBE

$$\frac{\partial}{\partial t} x^{ab}_{\mathbf{k}} = \mathrm{i}\omega^{ab}_{\mathbf{k}} x^{ab}_{\mathbf{k}} - \frac{\mathrm{i}}{\hbar}\mathbf{A}(t) \sum_{\mu} \Pi^{\mu a}_{\mathbf{k}} x^{\mu b}_{\mathbf{k}} - \Pi^{b\mu}_{k} x^{a\mu}_{\mathbf{k}} \tag{4.4}$$

and the approximation that pulse envelope $\mathbf{E}(t)$ is sufficient long enough, the the $\mathbf{A}$-field can be written as

$$\mathbf{A}(t) \approx \frac{1}{\omega_L}\mathbf{E}(t)\cos(\omega_L t). \tag{4.5}$$

Normally the differential equation (4.4) is analytically not solvable, but here t-times after the first pulse are considered where the envelope $\mathbf{E}$ is assumed to be zero. With this the first-order polarization takes on the form

$$\begin{aligned}
p^{ab}_{\mathbf{k}}(t) &= e^{\mathrm{i}\omega^{ab}_{\mathbf{k}} t} \int_{-\infty}^{t} dt' e^{-\mathrm{i}\omega^{ab}_{\mathbf{k}} t'} \frac{-\mathrm{i}}{\hbar}\frac{1}{\omega_L}\mathbf{E}(t')\cos(\omega_L t')\Pi^{ba}_{\mathbf{k}} \underbrace{x^{(0)bb}_{\mathbf{k}}}_{=1} \\
&= \frac{-\mathrm{i}}{\hbar\omega_L}\left\langle \Pi^{ba}_{\mathbf{k}} | E_1 \right\rangle e^{\mathrm{i}\omega^{ab}_{\mathbf{k}} t} \int_{-\infty}^{t} dt' \frac{1}{2} E(t') (e^{\mathrm{i}(\omega_L - \omega^{ab}_{\mathbf{k}})t'} + e^{\mathrm{i}(-\omega_L - \omega^{ab}_{\mathbf{k}})t'}) \\
&= \frac{-\mathrm{i}\left\langle \Pi^{ba}_{\mathbf{k}} | E_1 \right\rangle}{2\hbar\omega_L} (E_1(-\omega_L - \omega^{ab}_{\mathbf{k}}) + E_1(\omega_L - \omega^{ab}_{\mathbf{k}})) e^{\mathrm{i}\omega^{ab}_{\mathbf{k}} t},
\end{aligned} \tag{4.6}$$

with $\left\langle \Pi^{ba}_{k} | E_1 \right\rangle$ representing the scalar product between the momentum matrix elements and the electric field vector. The functions $E_1(-\omega_L - \omega^{ab}_{\mathbf{k}})$ and $E_1(\omega_L - \omega^{ab}_{\mathbf{k}})$ are the Fourier transform of the envelope $E(t)$ and represent the spectral overlap of $E(t)$ with frequency $\omega^{ab}_{\mathbf{k}}$. Trivially, the first-order can only contain one field component and thus cannot show any coherent control effects visible in a shift current due to its second-order nature. At least second-order is required to describe the phase dependence. The general expression for the second-order SBE is

$$\begin{aligned}
\frac{\partial}{\partial t} x^{(2)dd'}_{\mathbf{k}} &= \mathrm{i}\omega^{dd'}_{\mathbf{k}} x^{(2)dd'}_{\mathbf{k}} - \frac{\mathrm{i}}{\hbar}\mathbf{A}(t) \sum_{\mu} \Pi^{\mu d}_{\mathbf{k}} x^{(1)\mu d'}_{\mathbf{k}} - \Pi^{d'\mu}_{\mathbf{k}} x^{(1)d\mu}_{\mathbf{k}} \\
&= \mathrm{i}\omega^{dd'}_{\mathbf{k}} x^{(2)dd'}_{\mathbf{k}} - \frac{\mathrm{i}}{\hbar}\mathbf{A}(t) (\underbrace{\sum_{\bar{d}'} \Pi^{\bar{d}'d}_{\mathbf{k}} x^{(1)\bar{d}'d'}_{\mathbf{k}}}_{A} - \underbrace{\sum_{\bar{d}} \Pi^{d'\bar{d}}_{\mathbf{k}} x^{(1)d\bar{d}}_{\mathbf{k}}}_{B})
\end{aligned} \tag{4.7}$$

Similar as in four-wave-mixing experiments the excited coherences can be ordered according to combinations of the four electric field components, E^1_x & E^1_y from the first pulse and E^2_x & E^2_y from the second pulse. In second order, coherences belonging to $E_x^1 \cdot E_y^1$, $E_x^2 \cdot E_y^2$, or $(E_x^1)^2$ and the three analogous terms cannot show any coherent control effects in the shift current. The first two terms are responsible for a shift current at $t = 0$ and at $t = \tau$, respectively, while $(E_x^1)^2$, $(E_x^2)^2$, $(E_y^1)^2$ & $(E_y^2)^2$ cannot contribute to a shift current since they are not fulfilling the symmetry conditions. In a similar vein the terms $E_x^1 \cdot E_x^2$ and $E_y^1 \cdot E_y^2$ cannot contribute to a shift current either since they are also not fulfilling the symmetry conditions. Thus the only terms containing the phase factor τ and contribution to the shift current are $E_x^1 \cdot E_y^2$ and $E_y^1 \cdot E_x^2$. It becomes clear that the second shift current is a superposition of a normal shift current created by the τ-pulse and an additional current created by the overlap of the first-order polarization created at $t = 0$ and pulse at $t = \tau$

Based the previous evaluation of the electric field components, only the second order terms are further evaluated which contain $E_1 \cdot E_2$. Because of the symmetry, the second order results are written with generalized E_1 and E_2 vector components, where it is assumed that E_1 and E_2 belong to different polarization directions. The evaluation of the terms A and B can be found in the Appendix A.2. The final result is:

$$
\begin{aligned}
x_{\mathbf{k}}^{(2)dd'} &= e^{\mathrm{i}\omega_{\mathbf{k}}^{dd'}t} \int_{-\infty}^{t} dt' \frac{-1}{(2\hbar\omega_L)^2} E(t')(\\
&+ \sum_{\bar{d}'} \left\langle \Pi_{\mathbf{k}}^{\bar{d}'d} | E_2 \right\rangle \left\langle \Pi_{\mathbf{k}}^{d'\bar{d}'} | E_1 \right\rangle (E_1(-\omega_L - \omega_{\mathbf{k}}^{\bar{d}'d'}) + E_1(\omega_L - \omega_{\mathbf{k}}^{\bar{d}'d'})) \\
&\times (e^{\mathrm{i}(\omega_{\mathbf{k}}^{\bar{d}'d'} - \omega_L - \omega_{\mathbf{k}}^{dd'})t'} e^{-\mathrm{i}\varphi} + e^{\mathrm{i}(\omega_{\mathbf{k}}^{\bar{d}'d'} + \omega_L - \omega_{\mathbf{k}}^{dd'})t'} e^{\mathrm{i}\varphi}) \\
&- \sum_{\bar{d}} \left\langle \Pi_{k}^{d'\bar{d}} | E_2 \right\rangle \left\langle \Pi_{\mathbf{k}}^{\bar{d}d} | E_1 \right\rangle (E_1(-\omega_L - \omega_{\mathbf{k}}^{d\bar{d}}) + E_1(\omega_L - \omega_{\mathbf{k}}^{d\bar{d}})) \\
&\times (e^{\mathrm{i}(\omega_{\mathbf{k}}^{d\bar{d}} - \omega_L - \omega_{\mathbf{k}}^{dd'})t'} e^{-\mathrm{i}\varphi} + e^{\mathrm{i}(\omega_{\mathbf{k}}^{d\bar{d}} + \omega_L - \omega_{\mathbf{k}}^{dd'})t'} e^{\mathrm{i}\varphi}))
\end{aligned}
\tag{4.8}
$$

Further analytical evaluations are not possible at this point and numerical evaluation is necessary.

The numerical evaluation of the current belonging to Eq. (4.8) is shown in Fig. 4.17 for a simple three band system with parabolic band structure which consist of one valence, one conduction and one additional higher conduction band. The parameters of the three band model, effective mass and band distance, are based on known parameters from bulk GaAs. The numerical evaluation shows that the overlap current is maximal at the band gap and becomes smaller with larger detuning. The detuning also determines the intrinsic phase of the current and shows a periodicity of approximately 6 meV in the detuning. For an one-dimensional band structure, Fig. 4.17 column (a), the intrinsic phase is zero for band gap excitation and the current shows the π and 2π phase relation as known from linear excitation. For a two- and three-dimensional band structure, Fig. 4.17 column (b) & (c), the intrinsic phases are $\varphi \approx 1.5\pi$ and $\varphi \approx 1.25\pi$, respectively. The analytic result in Fig. 4.17(1c) matches the observed detuning dependence of the intrinsic phase seen in Fig. 4.16, with (2c) showing the same intrinsic phase $\varphi \approx 1.25\pi$ seen in the shift current in Fig. 4.15.

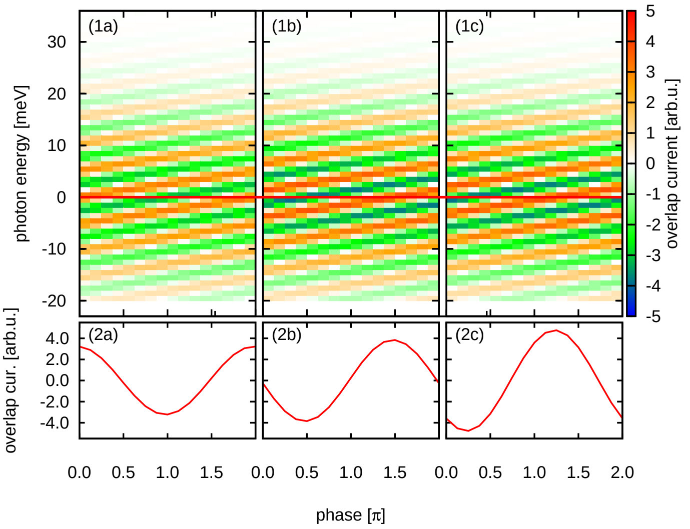

Figure 4.17: Numerical analysis of Eq. (4.8) for a three band system with parabolic band structure in (a) 1D, (b) 2D & (c) 3D. In the upper row, a two-dimensional scan of the peak current at $J(t = \tau)$, with $\tau = 800\,\text{fs}$ being the delay of the second optical pulse, is shown as function of the relative phase φ and the photon energy $\hbar\Delta\omega_L$, here given as detuning to the band gap. In the lower row the current for an optical excitation at the band gap, $\hbar\Delta\omega_L = 0$, is plotted.

The explanation for the unusual phase dependence can be explained by the term

$$e^{\mathrm{i}(\omega_{\mathbf{k}}^{d\bar{d}}-\omega_L-\omega_{\mathbf{k}}^{dd'})t'}e^{\mathrm{i}\varphi} = e^{\mathrm{i}(\Delta\omega_{\mathbf{k}}^{d\bar{d}}-\omega_{\mathbf{k}}^{dd'})t'}e^{\mathrm{i}\varphi}, \tag{4.9}$$

with $\Delta\omega_{\mathbf{k}}^{d\bar{d}} = \omega_{\mathbf{k}}^{d\bar{d}} - \omega_L$. At $\mathbf{k}$-points resonant to ω_L it is $\Delta\omega_{\mathbf{k}}^{d\bar{d}} = 0$ and the phase of the current is determined solely by the pulse phase φ. But besides the resonant $\mathbf{k}$-points, the finite spectral width of the optical pulse also excites the neighboring $\mathbf{k}$-points in the band structure with $\Delta\omega_{\mathbf{k}}^{d\bar{d}} \neq 0$. In addition to the pulse phase φ, the current phase is now also determined by $\Delta\omega_{\mathbf{k}}^{d\bar{d}}t'$. This is related to the phenomena of fringes in the spectrum of two pulses separated by a time delay τ.

In Fig. 4.18(a) and Fig. 4.19(a) the total current J as well as the total excited population n are shown as function of time. For band gap excitation the total current J as well as total excited population n are maximal for a relative pulse phase of $\varphi = 1.25\pi$ which is in agreement with Fig. 4.15 and Fig. 4.17(2c). The total current displays an oscillation after the optical pulses. This oscillation is caused by the intraband coherence between heavy and light hole band, its energy range of a few meV lies within the spectral range of the shift current. Due to the lack of dephasing and relaxation, the oscillation of the intraband coherence is visible while under normal conditions it would have declined on the used time scale. The corresponding radial population pictures show the formation of population fringes after the second pulse. For the resonant **k**-points at $k_{rad} \approx 0$ the population follows the expected coherent control phase relation, being maximal for a phase of $\varphi = 0\pi$ (1b) and minimal for a phase of $\varphi = 1\pi$ (2b). The radial population demonstrates why the current follows a sine dependence and not the expected cosine dependence. For a phase of $\varphi = 0\pi$ the population at the Γ-point is maximal, but the Γ-point has a minimal density of states. Thus by introducing a phase difference, the fringes of the population move to higher **k**-points which have an increased density of states allowing for more excited carriers and consequently a larger current.

In Fig. 4.19 the situation for an excitation for 100 meV above the band gap is shown. In comparison with Fig. 4.18, two population traces are now visible in the radial population. The two traces correspond to the heavy hole transition for the larger **k**-values and to the light hole transition for the smaller **k**-values. Both traces show the formation of phase dependent fringes in the radial population, but since heavy hole and light hole have different dispersion as well as different density of states, a simple correlation between the shift of fringes in **k**-space and maximal population becomes difficult. In comparison with band gap excitation in Fig. 4.18 the total population n displays only small changes due to the varying phase. Unlike the Γ-point, the curvature of the density of states becomes flatter for larger **k**-values. In addition, the whole spectral width of the optical pulse contributes to the excitation while for band gap excitation only half of the spectral width contributes. This causes the movement of the fringes to become less noticeable. The total current J shows larger deviations for different phases which is caused by the already mentioned intraband coherence between light and heavy hole.

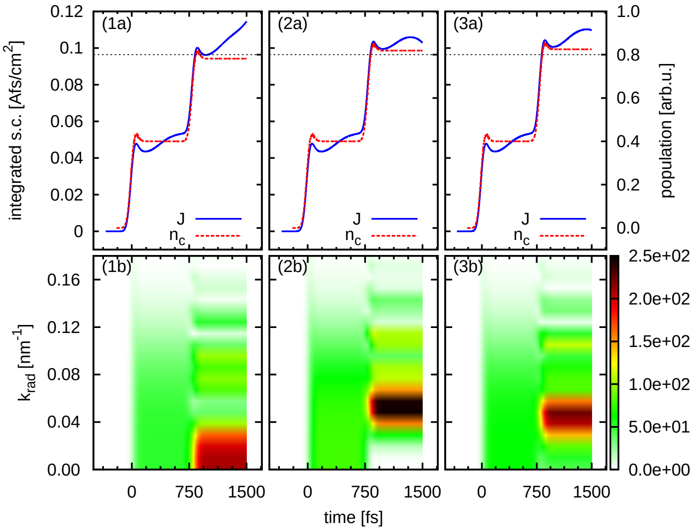

Figure 4.18: Excitation of the system with two pulses at $t = 0$ fs and $\tau = 800$ fs for a photon energy $\hbar\omega_L = E_{gap}$. This setup corresponds to Fig. 4.15. (a) The total current J and the total population n are shown for a relative phase of (1a) $\varphi = 0\pi$, (2a) $\varphi = 1\pi$, and (3a) $\varphi = 1.25\pi$ which corresponds to the largest current increase in Fig. 4.15. The population only increases during the moment of excitation while the total current fluctuates. The dotted black line is a visual aid for better comparison between the different excitation. (b) The radial-resolved population in **k**-space, color-coded in arbitrary units, is shown as a function of time and $|k_{rad}|$. Phase dependent fringes are seen in the radial population after the second pulse.

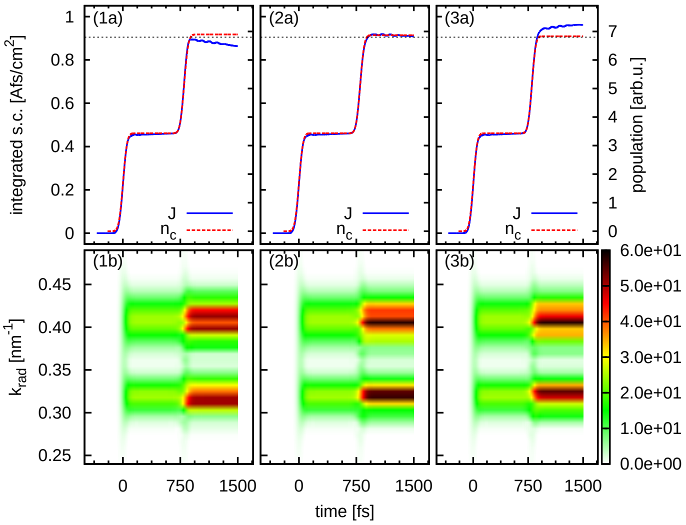

Figure 4.19: Excitation of the system with two pulses at $t = 0\,\text{fs}$ and $\tau = 800\,\text{fs}$ for a photon energy $\hbar\omega_L = E_{gap} + 100\,\text{meV}$. This setup corresponds to Fig. 4.16(b). (a) The total current J and the total population n are shown for a relative phase of (1a) $\varphi = 0\pi$, (2a) $\varphi = 1\pi$, and (3a) $\varphi = 1.75\pi$ which corresponds to the the biggest current increase in Fig. 4.16(b). As in Fig. 4.18 the population only increases during the moment of excitation. (b) Shown is the radial-resolved population in $\mathbf{k}$-space with two population traces. After the second pulse phase dependent fringes are seen in the radial population.

The investigation shows that the phase-dependent fringes in the population do modify the shift current. The effect is maximal at the band gap due to the strong slope of the density of stats $D(\omega)$ and the only partially resolution of the spectral width of the optical pulse. Both amplify the effects caused by the shifting fringes in the population. However, in a real semiconductor the Coulomb interaction modifies the band structure, causing the density of state to become constant at the bad gap. In addition, the exciton will further modify the absorption. Both effects are not present in these simulations, but are for experimental comparison critical.

Chapter 5

Shift Currents in GaAs Quantum Wells

While the zincblende structure is inversion asymmetric, it is still a crystal structure with a high symmetry which leads to an inversion symmetry of the band structure in **k**-space. But in systems of reduced dimensionality like a quantum well (QW) the symmetry of the crystal structure can be further reduced which reflects itself in the band structure. The injection current, a current caused by an asymmetric distribution of carriers in **k**-space, is normally symmetry forbidden in the inversion symmetric band structure of bulk GaAs. But in QW systems grown in (100)-direction the reduced symmetry leads to a spin-splitting of the band structure which breaks the inversion symmetry. Consequently, it is possible to generate injection currents in (110)-grown QW systems. Several aspects of injection currents in GaAs QW systems have been investigated before and therefore will not be discussed in this work.[23–27]

As it was discussed in the previous chapter, the shift current is an effect caused by the lack of inversion symmetry of the GaAs crystal structure. In this chapter, the influence of the reduced symmetry of a QW system on the shift current will be investigated.

5.1 Quantum Well Band Structure

The band structure of the QW system is obtained by solving the extended Kane model. But the 14 band model was developed for bulk systems and thus has to be modified to account for the reduced dimensionality of a QW. The envelop function approach is used to describe the electronic wave function $\Psi^{\lambda}_{\mathbf{k}_{\parallel}}(\mathbf{r})$ in the QW, $\mathbf{k}_\parallel$ being a two-dimensional in-plane wave vector.[61, 79] The electron wave function has the form

$$\Psi^{\lambda}_{\mathbf{k}_\parallel}(\mathbf{r}) = e^{\mathrm{i}\mathbf{k}_\parallel \mathbf{r}_\parallel} \sum_n f^{\lambda}_{n\mathbf{k}_\parallel}(z) u_n(\mathbf{r}), \tag{5.1}$$

with the z-axis chosen to be the growth direction and λ the band index of the 14-band model. The electron wave function consists of two terms, the unit cell periodic part $u_n(\mathbf{r})$ of the Bloch wave function, which accounts for the in-plane periodicity, and a slowly varying envelop function $f^{\lambda}_{n\mathbf{k}_\parallel}(z)$ which is used to describe the wave function in z-direction. The envelop function $f^{\lambda}_{n\mathbf{k}_\parallel}(z)$ satisfies the effective mass equation

$$\sum_{m=1}^{14} \left[\hat{\mathrm{H}}_{nm}(\mathbf{k}_\parallel, -\mathrm{i}\partial_z) + V_n(z)\delta_{nm} \right] f^{\lambda}_{m\mathbf{k}_\parallel}(z) = E^{\lambda}_{\mathbf{k}_\parallel} f^{\lambda}_{n\mathbf{k}_\parallel}(z), \tag{5.2}$$

with $\hat{\mathrm{H}}_{nm}$ being the bulk Hamiltonian and $V_n(z)$ being the well potential. Because of the confinement in z-direction, the operator $\hat{k}_z$ is replaced by $-\mathrm{i}\partial/\partial_z$. The envelop function is expanded into a set of confinement functions $\varphi_l(z)$ via

$$f^{\lambda}_{n\mathbf{k}_\parallel}(z) = \sum_{l=1}^{N} a^{\lambda l}_{n\mathbf{k}_\parallel} \varphi_l(z). \tag{5.3}$$

This leads to a $14N \times 14N$ eigenvalue problem

$$\sum_{m=1}^{14} \sum_{l'=1}^{N} \langle \varphi_l | H_{nm} + V_n \delta_{nm} | \varphi_{l'} \rangle a^{\lambda l'}_{m\mathbf{k}_\parallel} = E_{\lambda \mathbf{k}_\parallel} a^{\lambda l}_{n\mathbf{k}_\parallel}. \tag{5.4}$$

The confinement functions have the explicit form

$$\varphi_l(z) = \sin\left[\frac{\pi l}{L} \left(z + \frac{L}{2} \right) \right] \tag{5.5}$$

for $|z| \leq L/2$ and zero otherwise. The width L is chosen in such a way that numerically convergent results are ensured.

To obtain the band structure of a $\mathbf{Z}$-grown QW, with $\mathbf{Z}$ being the z-direction in an arbitrary coordinate system, the envelop function approach has to be applied to the corresponding Hamiltonian $\hat{\mathrm{H}}^{\mathbf{Z}}(\mathbf{k})$. This of course requires to know the explicit form of $\hat{\mathrm{H}}^{\mathbf{Z}}(\mathbf{k})$ which has to be derived for each growth direction $\mathbf{Z}$. Using the concept of Euler rotation matrices a more elegant approach is possible.[60] Euler rotation matrices are a method to describe the rotation in three-dimensions. The transformation from the the old coordinates k_x,k_y, and

k_z to the rotated coordinates $\tilde{k}_x$,$\tilde{k}_y$, and $\tilde{k}_z$ is given by

$$\begin{aligned}\tilde{\mathbf{k}} &= R(\alpha,\beta,\gamma)\mathbf{k}\\ \mathbf{k} &= R^T(\alpha,\beta,\gamma)\tilde{\mathbf{k}},\end{aligned} \tag{5.6}$$

with $R(\alpha,\beta,\gamma)$ being the Euler rotation matrix; $R^{-1}(\alpha,\beta,\gamma) = R^T(\alpha,\beta,\gamma)$ due to orthogonality and α, β, and γ the Euler angles describing the rotation. The invariant description of the extended Kane model $\hat{\mathrm{H}}_{14\times14}(\mathbf{k})$ given in Chapter 3.1.2 is for a standard coordinate system with $\mathbf{x} = \mathbf{e}_x$, $\mathbf{y} = \mathbf{e}_y$, and $\mathbf{z} = \mathbf{e}_z$. Using Euler rotations the Hamiltonian can be evaluated for an arbitrary coordinate systems via

$$\hat{\mathrm{H}}_{14\times14}(\mathbf{k}) = \hat{\mathrm{H}}_{14\times14}(R^T(\alpha,\beta,\gamma)\tilde{\mathbf{k}}) = \hat{\mathrm{H}}_{14\times14}^{R(\alpha,\beta,\gamma)}(\tilde{\mathbf{k}}), \tag{5.7}$$

with the Hamiltonian $\hat{\mathrm{H}}_{14\times14}^{R(\alpha,\beta,\gamma)}$ being the rotated extended Kane Hamiltonian. Instead of rotating the coordinate system, the Hamiltonian is rotated. While for the three-dimensional case the rotation of either the coordinate system or the Hamiltonian are equivalent, for a two-dimensional system this gives the advantage of having the direction $\tilde{\mathbf{Z}}$ as an universal growth direction for an arbitrary oriented crystal system. By applying the envelop function approach on $\tilde{k}_z$ an two-dimensional Hamiltonian $\hat{\mathrm{H}}_{QW}^{R(\alpha,\beta,\gamma)}(\tilde{k}_x,\tilde{k}_y)$ can be constructed without the need to derive the explicit form of the Hamiltonian for a growth direction $\mathbf{Z}$.

The semiconductor Bloch equations (SBE) are again used to determine the time evolution of the optical excitations in the system. The SBE for a QW are structurally identical to the bulk equations (3.10), only the three-dimensional $\mathbf{k}$-vector has to be replaced by the two-dimensional in-plane $\mathbf{k}_{\|}$-vector:

$$\frac{d}{dt}x_{\mathbf{k}_{\|}}^{\lambda\lambda'} = \frac{i}{\hbar}\left(\epsilon_{\mathbf{k}_{\|}}^{\lambda} - \epsilon_{\mathbf{k}_{\|}}^{\lambda'}\right)x_{\mathbf{k}_{\|}}^{\lambda\lambda'} + \frac{i}{\hbar}\frac{e_0}{m_0}\mathbf{A}(t)\cdot\sum_{\mu}\left(\mathbf{\Pi}_{\mathbf{k}_{\|}}^{\mu\lambda}x_{\mathbf{k}_{\|}}^{\mu\lambda'} - \mathbf{\Pi}_{\mathbf{k}_{\|}}^{\lambda'\mu}x_{\mathbf{k}_{\|}}^{\lambda\mu}\right) - \frac{1}{T_{1/2}}x_{\mathbf{k}_{\|}}^{\lambda\lambda'}. \tag{5.8}$$

The momentum matrix elements are calculated in the same manner as in the bulk case, Eq. (3.11), again replacing $\mathbf{k}$ by $\mathbf{k}_{\|}$:

$$\mathbf{\Pi}_{\mathbf{k}_{\|}}^{\lambda\lambda'} = \frac{m_0}{\hbar}\left\langle\nabla_{\mathbf{k}_{\|}}H(\mathbf{k}_{\|})\right\rangle_{\lambda\lambda'} \tag{5.9}$$

5.2 Shift Currents in (110)-grown Quantum Wells

5.2.1 Polarization Direction Dependence

While it is not explicitly shown in this work, the shift current angle dependence can be simply conducted from a basic vector analysis. Any vector in the xy-plane can be composed into (110) and (1-10) components, which respectively create a shift current in (00-1) or the reverse (001)-direction. Thus the shift current for any given polarization angle θ, the angle between the x-direction and the pulse polarization in the xy-plane, is:

$$\begin{aligned} J^z &\propto -\left(\begin{pmatrix}1\\1\\0\end{pmatrix} \cdot E\begin{pmatrix}\sin\theta\\ \cos\theta\\ 0\end{pmatrix}\right)^2 + \left(\begin{pmatrix}1\\-1\\0\end{pmatrix} \cdot E\begin{pmatrix}\sin\theta\\ \cos\theta\\ 0\end{pmatrix}\right)^2 \\ &\propto -\sin\theta\cos\theta - \sin\theta\cos\theta \end{aligned} \tag{5.10}$$

Applying the trigonometric addition formulas gives

$$J^z \propto -\sin 2\theta \tag{5.11}$$

In a (110)-grown QW the further reduced symmetry may lead to changes in the angle dependence of the shift current. In the QW the new coordinate axes $\mathbf{X} = (001)$ and $\mathbf{Y} = (1-10)$ are used. Like for the bulk case the electric field of the incident pulse can be decomposed into $\mathbf{X}$ and $\mathbf{Y}$ components:

$$\mathbf{E} = E\begin{pmatrix}0\\0\\ \cos\theta\end{pmatrix} + E\begin{pmatrix}\sin\theta\\ -\sin\theta\\ 0\end{pmatrix} \tag{5.12}$$

In the same vein, the currents in x, y, and z-direction can be determined as function of θ. Doing an analogous vector analysis results in:

$$\begin{aligned} J^x &\propto -\sin 2\theta \\ J^y &\propto +\sin 2\theta \\ J^z &\propto 1 + 1 - 2(\cos\theta)^2 = -\cos 2\theta + 1 \end{aligned} \tag{5.13}$$

Based on this, it can be expected that the shift current has a

$$\begin{aligned} J^{\mathbf{X}} &\propto -\cos 2\theta + 1 \\ J^{\mathbf{Y}} &\propto \sin 2\theta \end{aligned} \tag{5.14}$$

angle dependence.

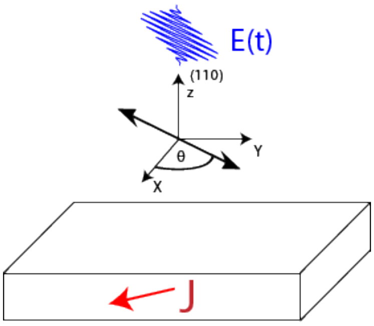

Figure 5.1: Schematic illustration of the simulated setup. The system is excited with a linearly polarized optical pulse by polarization direction in the **XY**-plane which generates a shift current in the QW. The **X**, **Y**, and **Z**-axis of the QW are not the crystallographic axes but depend on the QW growth direction, here $\mathbf{X} = (001)$, $\mathbf{Y} = (1\text{-}10)$ and $\mathbf{Z} = (001)$. For the simulations a QW with a thickness of 8 nm and a growth direction $\mathbf{Z} = (110)$ is considered. The angle θ lies between polarization direction of the incident excitation pulse in the xy-plane and the new **X**-direction. For sufficient convergence of the shift current 12 valence bands and 28 conduction bands are included when solving the SBE. Phenomenological dephasing and relaxation times are $T_1 = T_2 = 200$ fs.

In Fig. 5.2 the shift currents in **X** and **Y**-direction are shown. In **Y**-direction the shift current has the $E^2_{env}(t)$ shape apart of a small time delay due to the finite line width of the Gaussian pulse which is already known from the bulk simulations. For **X**-parallel as well as **Y**-parallel polarization the shift current vanishes. The **X**-polarization direction corresponds to a (001)-polarization in bulk which forbids a shift current. The **Y**-polarization direction corresponds to a (1-10)-polarization which creates a shift current only in (001)-direction, i.e., the **X**-direction of the QW. The polarization dependence of the shift current amplitude in **Y**-direction is described by

$$J^{\mathbf{Y}}_{shift}(\theta) = C\sin(2\theta), \tag{5.15}$$

which is in agreement with the previous symmetry consideration.

In **X**-direction, see Fig. 5.2(a), the shift current has a negative offset. For **Y**-parallel polarized excitation the creation of a shift current in **X**-direction is in agreement with the bulk symmetry rules. However, for **X**-parallel excitation the bulk symmetry rules forbid a shift current in **X**-direction. The visible offset for **X**-parallel excitation is due to the shift current tensor element σ_{xxx} which exists in (110)-grown QWs due to the reduced symmetry[33, 34] and allows for a finite shift current to exist. The polarization dependence of the shift current amplitude in **X**-direction is described by

$$J^{\mathbf{X}}_{shift}(\theta) = A\cos(2\theta) + B. \tag{5.16}$$

In Fig. 5.3 the **X**- and **Y**-shift currents are simulated for excitation at the band edge of the QW. Clearly visible are the sine and cosine dependence of the currents, the offset in **X**-shift current manifests itself as a shift of the white zero-line in the two-dimensional plot. The position change of the zero-line indicates that the offset depends on the excitation energy $\hbar\omega_L$.

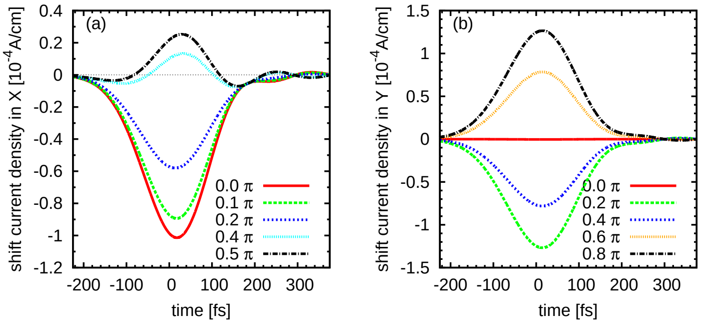

Figure 5.2: The shift current in (a) **X**-direction and in (b) **Y**-direction. The currents are calculated for a linearly polarized Gaussian pulses with central frequency $\hbar\omega_L = 1.6\,\text{eV}$, a FWHM of 200 fs. The angle θ lies between the **X**-axis and the linear polarization of the pulse. The results were puplished in [80].

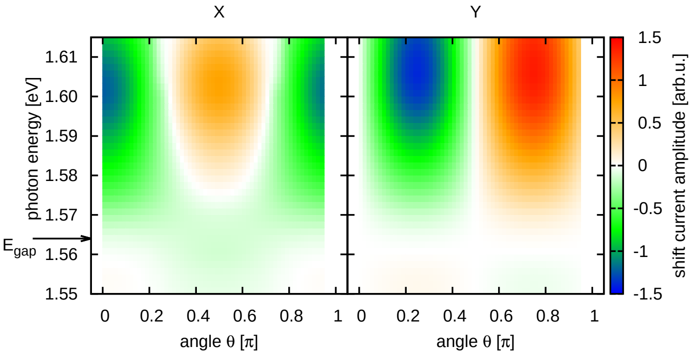

Figure 5.3: Two-dimensional scan of the shift current for a QW at a temperature $T = 0.1\,\text{K}$. Visible are the $\sin(2\theta)$ and $\cos(2\theta)$ dependencies of the shift current components $J^{\mathbf{X}}$ and $J^{\mathbf{Y}}$.

5.2.2 Photon Energy Dependence

As it was shown, the reduced symmetry in the QW results in a new shift current tensor element which slightly modifies the angle dependence of the shift current in comparison to the bulk case. In bulk the photon energy dependence of the shift current mirrors the density of states. In a QW the density of states has the form of step function at the transition energies of the band structure. In addition, the symmetry reduction breaks the inversion symmetry of the band structure. Therefore the photon energy dependence of the shift current in a QW can be expected to drastically differ from the bulk dependence beyond the change in the density of states.

In Fig. 5.4(a), the shift current intensity grows with increasing photon energy as in bulk. But with further increasing photon energy the shift current undergoes a current reversal. Analysis of the valence, conduction and interband sub-currents reveals that the shift current is generated in the valence band with the remaining bands having almost vanishing contribution. Both effects are in stark contrast to the bulk case where the shift current follows the density of states and is mainly generated in the conduction band and the interband polarization, see chapter 4.3.
In analogy to chapter 4.4, in Fig. 5.4(b) the parameters reflecting the inversion asymmetry Δ^-, P', and C_k are set to zero and the shift current is calculated for *inversion symmetric* GaAs. The simulations show that the reduced symmetry itself does not cause a shift current. Even in a QW system the base crystal structure has to be inversion asymmetric to allow for a shift current to exist. The small current visible at 1.5 eV is caused by the GaAlAs environment the GaAs QW is embedded in.

To find the reason for the current reversal, the behavior of the valence band shift current is compared with the corresponding population in the two highest valence bands, Fig. 5.5. The comparison reveals that the energy range of the current reversal overlaps with band crossing in **k**-space. Especially Fig. 5.6(2a) shows a strong deviation from the Gaussian shape which corresponds to an excitation at the band crossing.

A **k**-resolved map of the shift current J_x is done in Fig. 5.6 for the photon energies $\hbar\omega_L = 1.500\,\text{eV}$, $\hbar\omega_L = 1.525\,\text{eV}$, and $\hbar\omega_L = 1.550\,\text{eV}$, respectively. For a photon energy of $\hbar\omega_L = 1.500\,\text{eV}$ the shift current has its negative minimum. In the corresponding 2D picture, Fig. 5.6(1b), most areas of **k**-space have for each current $j_{\mathbf{k}}$ at k_x a corresponding anti-current at $-k_x$ which leads to zero

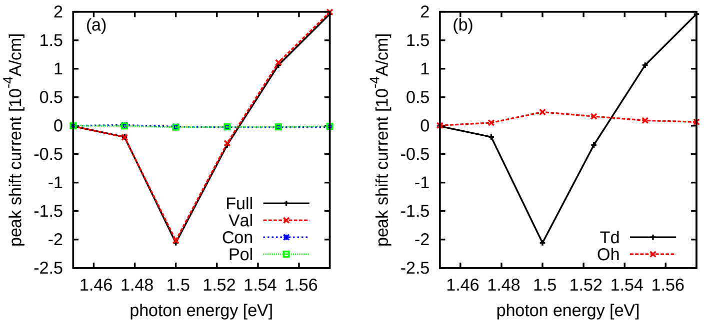

Figure 5.4: Calculated peak amplitude of the shift current $J^{\mathbf{X}}$ as function of the photon energy $\hbar\omega_L$ for **X**-parallel polarized light at room temperature. (a) Displayed is the total shift current and its three subcurrents stemming from the valence band, the conduction band, and the interband current. (b) The shift current is compared with GaAs QW with an artificial Oh symmetry, see Chapter 4.4 for the equivalent bulk calculation.

net contribution. In addition, the microscopic currents display a sign change at the resonant **k**-points which have the highest carrier population in Fig. 5.5(1b). Noticeable the area around the gamma point shows a symmetry break and has predominantly negative current contribution. It is therefore the area in **k** space in which the shift current is generated.

For a photon energy $\hbar\omega_L = 1.525\,\text{eV}$, Fig. 5.6(2), the shift current transitions from a negative to a positive current direction and divergences strongly from the Gaussian shape. The excited **k**-area around the Γ-point still has mostly negative current contribution, but the total non-canceling contributions are less. The areas beyond the band mixing at $k_y \approx \pm 0.2nm^{-1}$ have more positive current contributions which causes a decease of the total shift current. In addition, resonant contributions exist, mainly the valence band intraband coherence which energy range overlaps with the shift current in frequency space and therefore is included in the frequency filtering process. They are responsible for the deviation from the Gaussian shape. This makes a distinction between shift current and intraband current difficult.

For the photo energy $\hbar\omega_L = 1.550\,\text{eV}$, Fig. 5.6(3), the shift current has a positive current direction and follows a Gaussian shape. The 2D surface plots reveal that the area around the Γ-point is too off-resonant and has no current contributions. Except of the areas beyond the bandmixing at $k_y \approx \pm 0.2nm^{-1}$ most areas of **k**-space are canceling each other. The areas beyond the bandmixing display both positive and negative current contributions, but with a predominance of positive contribution this region of **k**-space is responsible for the positive shift current.

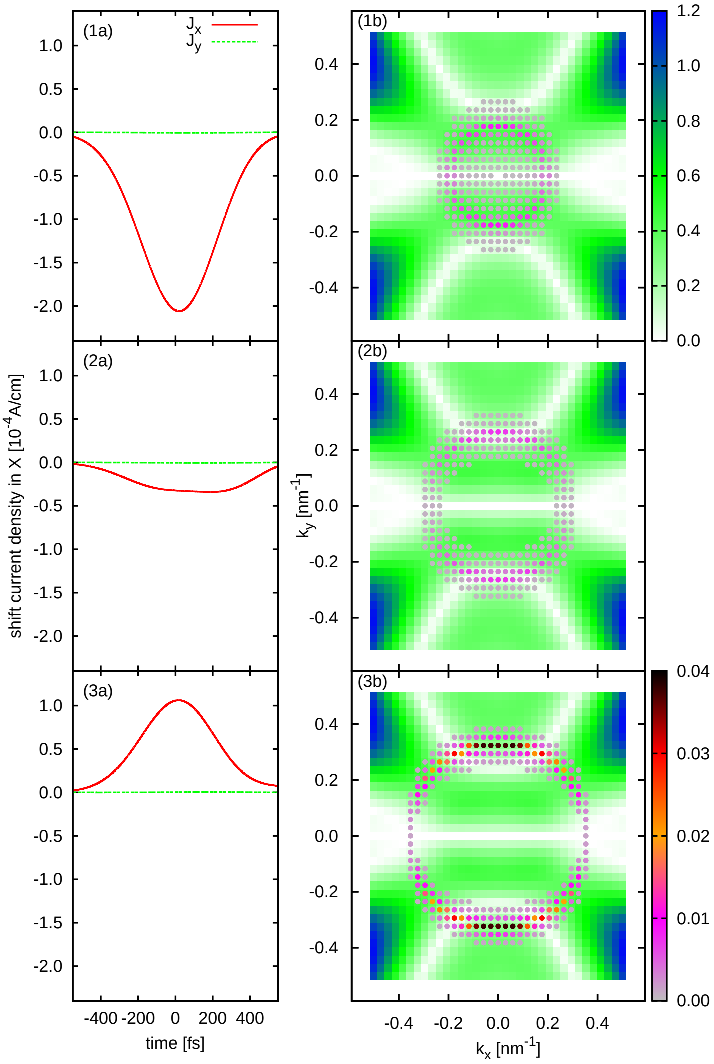

Figure 5.5: The shift current for a photon energy of (1a) $\hbar\omega_L = 1.500\,\text{eV}$, (2a) $\hbar\omega_L = 1.525\,\text{eV}$, and (3a) $\hbar\omega_L = 1.550\,\text{eV}$. In (1b) - (3b) the energy difference $\Delta\epsilon(k_x, k_y)$ between the two highest valence bands is displayed, color-scaled in meV. To the different photon energies the corresponding populations $n(k_x, k_y, t = 0)$ of the two highest valence bands are overlaid, color-scale in arbitrary units.

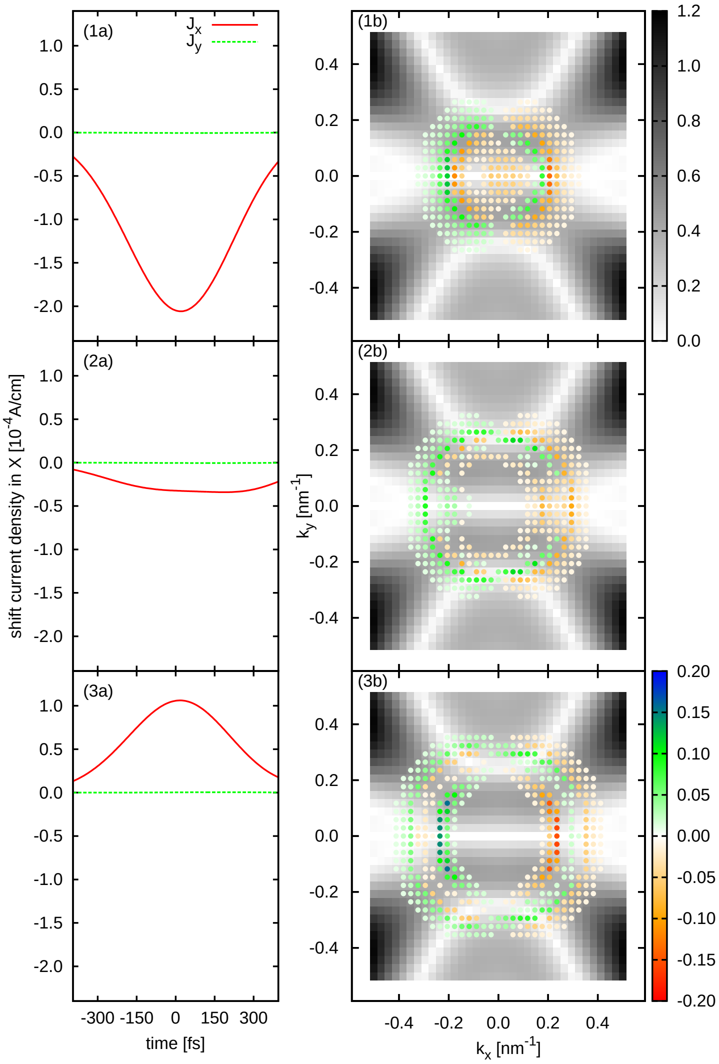

Figure 5.6: The shift current for a photon energy of (1) $\hbar\omega_L = 1.500\,\mathrm{eV}$, (2) $\hbar\omega_L = 1.515\,\mathrm{eV}$ & (3) $\hbar\omega_L = 1.550\,\mathrm{eV}$. In (1b) to (3b) the $\mathbf{k}$ resolved shift current J_x generated in the QW is shown at the time $t = 0\,\mathrm{fs}$, scale in arbitrary units, overlayed over the energy difference between the two highest valence bands, scale in meV.

In conclusion, shift currents created in the area of **k**-space before and after the band crossing have different signs and increasing the photon energy leads to a shift in **k**-space from one region to the other. These results were published in [81].

Chapter 6

Shift Currents near the Band Gap

The interaction of charged particles due to the Coulomb force is a fundamental interaction which can be found in all kinds of systems, ranging from bulk materials to quantum wires(QW) and quantum dots(QD), and many different materials, e.g., metals, semiconductors, and organic materials. Consequently, Coulomb effects are a topic in a huge variety of research fields. [82–87] For the simulation of shift currents near the band gap the inclusion of the many-body Coulomb interaction is necessary since excitonic effects are relevant.[11] But from a numerical point of view the simulations of excitons has two challenges.

First, the exciton binding energy in GaAs is very small in comparison to the band gap, literature values being $E_{exc} = -4.2\,\mathrm{meV}$ close to $0\,\mathrm{K}$ and $E_{exc} = -3.27\,\mathrm{meV}$ at $T = 17\,\mathrm{K}$.[88, 89] Consequently, long integration times are required for a good separation of the exciton from the continuum.
The second challenge is the many-body nature of the Coulomb interaction which couples the whole simulation space. Many body correlation effects, e.g., biexcitons and triexcitons, lead to a drastic increase of computational effort.[90, 91] Limiting the Coulomb interaction to only describe exciton correlations still leads to a quadratic increase of the numerical effort. Due to these numerical requirements, theoretical investigation of excitonic effects often uses approximations such as parabolic bands and/or a small number of bands to decrease the numerical effort.[92–96] Only recently more complex simulations of excitons via (time-dependent) density-functional theory were reported.[97–99]

In this chapter the necessary steps to include Coulomb interaction into the combined theory of k.p and SBE will be laid down and an analysis of the numerical obstacle will be given. Thereafter, the results for the shift currents with exciton enhancement near the band gap will be presented and discussed.

6.1 Coulomb Matrix Elements

The Coulomb Hamiltonian has the general form

$$\hat{H}_C = \frac{1}{2}\int\int dV dV' \Psi^\dagger(\mathbf{r})\Psi^\dagger(\mathbf{r}')V(\mathbf{r}-\mathbf{r}')\Psi(\mathbf{r}')\Psi(\mathbf{r}), \tag{6.1}$$

where Ψ are Fermionic field operators. The field operators are expanded in a basis of creation and annihilation operators $a_{\mathbf{k}}^{\dagger\lambda}$ & $a_{\mathbf{k}}^{\lambda}$ and in yet undetermined basis functions φ:

$$\Psi(\mathbf{r}) = \sum_{\mathbf{k},\lambda} \hat{a}_{\mathbf{k}}^{\lambda}\varphi_{\mathbf{k},\lambda}(\mathbf{r}) \tag{6.2}$$

Inserting Eq. (6.2) in Eq. (6.1) the Coulomb Hamiltonian takes the form:

$$\begin{aligned}\hat{H}_C = \frac{1}{2} &\sum_{\substack{\lambda_1,\lambda_2,\lambda_3,\lambda_4\\ \mathbf{k}_1,\mathbf{k}_2,\mathbf{k}_3,\mathbf{k}_4}} \hat{a}_{\mathbf{k}_1}^{\dagger\lambda_1}\hat{a}_{\mathbf{k}_2}^{\dagger\lambda_2}\hat{a}_{\mathbf{k}_3}^{\lambda_3}\hat{a}_{\mathbf{k}_4}^{\lambda_4}\\ &\times\int\int dV dV' \varphi^*_{\lambda_1,\mathbf{k}_1}(\mathbf{r})\varphi^*_{\lambda_2,\mathbf{k}_2}(\mathbf{r}')V(\mathbf{r}-\mathbf{r}')\varphi_{\lambda_3,\mathbf{k}_3}(\mathbf{r}')\varphi_{\lambda_4,\mathbf{k}_4}(\mathbf{r})\end{aligned} \tag{6.3}$$

The double integral is now called the Coulomb matrix element $V_{\mathbf{k}_1,\mathbf{k}_2,\mathbf{k}_3,\mathbf{k}_4}^{\lambda_1,\lambda_2,\lambda_3,\lambda_4}$. To evaluate the double integral the previously undetermined basis φ is now expanded in a Bloch function basis

$$\varphi_{\mathbf{k},\lambda}(\mathbf{r}) = \frac{1}{\sqrt{V}}\sum_{l} c_{\mathbf{k},\lambda}^{l} u^{l}(\mathbf{r})e^{\mathrm{i}\mathbf{k}\cdot\mathbf{r}}, \tag{6.4}$$

with V being the unit cell volume. Inserted into $V_{\mathbf{k}_1,\mathbf{k}_2,\mathbf{k}_3,\mathbf{k}_4}^{\lambda_1,\lambda_2,\lambda_3,\lambda_4}$ the Coulomb matrix elements read

$$\begin{aligned}V_{\mathbf{k}_1,\mathbf{k}_2,\mathbf{k}_3,\mathbf{k}_4}^{\lambda_1,\lambda_2,\lambda_3,\lambda_4} = \frac{1}{V^2}&\int\int dV dV' e^{-\mathrm{i}\mathbf{k}_1\cdot\mathbf{r}}e^{-\mathrm{i}\mathbf{k}_2\cdot\mathbf{r}'}e^{\mathrm{i}\mathbf{k}_3\cdot\mathbf{r}'}e^{\mathrm{i}\mathbf{k}_4\cdot\mathbf{r}}V(\mathbf{r}-\mathbf{r}')\\ &\times\sum_{l_1}\bar{c}_{\mathbf{k}_1,\lambda_1}^{l_1}\bar{u}^{l_1}(\mathbf{r})\sum_{l_2}\bar{c}_{\mathbf{k}_2,\lambda_2}^{l_2}\bar{u}^{l_2}(\mathbf{r}')\sum_{l_3}c_{\mathbf{k}_3,\lambda_3}^{l_3}u^{l_3}(\mathbf{r}')\sum_{l_4}c_{\mathbf{k}_4,\lambda_4}^{l_4}u^{l_4}(\mathbf{r}).\end{aligned} \tag{6.5}$$

If a periodic function $\varphi(\mathbf{r})$ consists of a slow varying part $f(\mathbf{r})$ and a fast varying part $u(\mathbf{r})$ the volume integral can be approximated as

$$\begin{aligned}\int_{L^3} f(\mathbf{r})u(\mathbf{r})dV &= \sum_N \int_{l^3} f(\mathbf{r}+\mathbf{R}_N)u(\mathbf{r}+\mathbf{R}_N)dV \\ &\approx \sum_N f(\mathbf{R}_N)\int_{l^3} u(\mathbf{r})dV,\end{aligned} \tag{6.6}$$

with $\int_{l^3}$ going over one unit cell. Defining $u_c = \int_{l^3} u(\mathbf{r})dV$, the final expression is

$$\begin{aligned}\int_{L^3} f(\mathbf{r})u(\mathbf{r})dV &\approx \sum_N f(\mathbf{R}_n)u_c \\ &\approx u_c \cdot \int_{L^3} f(\mathbf{r})dV.\end{aligned} \tag{6.7}$$

The individual integrals in Eq. (6.5) can be rewritten as

$$\int dV \bar{f}'(\mathbf{r})\bar{u}'(\mathbf{r})V(\mathbf{r}-\mathbf{R})f(\mathbf{r})u(\mathbf{r}) = \int dV \tilde{f}(\mathbf{r})\tilde{u}(\mathbf{r})V(\mathbf{r}-\mathbf{R}), \tag{6.8}$$

with $\tilde{f}(\mathbf{r}) = \bar{f}'(\mathbf{r})f(\mathbf{r})$ and $\tilde{u}(\mathbf{r}) = \bar{u}'(\mathbf{r})u(\mathbf{r})$. If $V(\mathbf{r}-\mathbf{R})$ varies slowly on the scale of $\tilde{u}(\mathbf{r})$, the integral can be split into two parts

$$\begin{aligned}\int_{L^3} dV \tilde{f}(\mathbf{r})\tilde{u}(\mathbf{r})V(\mathbf{r}-\mathbf{R}) &\approx \int_{L^3} \tilde{f}(\mathbf{r})V(\mathbf{r}-\mathbf{R})\int_{l^3} dV'\tilde{u}(\mathbf{r}') \\ &\approx u_c \cdot \int_{L^3} \tilde{f}(\mathbf{r})V(\mathbf{r}-\mathbf{R})\end{aligned} \tag{6.9}$$

using the approximation described in Eq. (6.7). This approximation is valid for effects which are characterized by length scales much larger than the unit cell. In the case of GaAs the lattice constant is $a_{\mathrm{GaAs}} \approx 0.5\,\mathrm{nm}$. In comparison the Bohr radius of the exciton $a_B^{3d} \approx 12\,\mathrm{nm}$ is more than twenty times larger, thus fulfilling the approximation condition.

Table 6.1: A comparison of exciton binding energies and Bohr radii in direct band gap semiconductors.[100]

	GaAs	GaN	ZnSe
ϵ_R^{3d}	4 meV	23 meV	19 meV
a_B^{3d}	12 nm	3 nm	5 nm

6.1.1 Calculating the Coulomb Matrix Elements with k.p

By averaging the Coulomb potential inside the unit cell, the Coulomb matrix element can be rewritten as

$$\begin{aligned}V^{\lambda_1,\lambda_2,\lambda_3,\lambda_4}_{\mathbf{k}_1,\mathbf{k}_2,\mathbf{k}_3,\mathbf{k}_4} \approx \frac{1}{V^2}\int\int & e^{-\mathrm{i}\mathbf{k}_1\cdot\mathbf{r}} e^{-\mathrm{i}\mathbf{k}_2\cdot\mathbf{r}'} e^{\mathrm{i}\mathbf{k}_3\cdot\mathbf{r}'} e^{\mathrm{i}\mathbf{k}_4\cdot\mathbf{r}} V(\mathbf{r}-\mathbf{r}')dVdV' \\ \times & \int_{l^3}\int_{l'_3}\sum_{l_1}\bar{c}^{l_1}_{\mathbf{k}_1,\lambda_1}\bar{u}^{l_1}(\mathbf{r})\sum_{l_2}\bar{c}^{l_2}_{\mathbf{k}_2,\lambda_2}\bar{u}^{l_2}(\mathbf{r}') \\ & \times\sum_{l_3}c^{l_3}_{\mathbf{k}_3,\lambda_3}u^{l_3}(\mathbf{r}')\sum_{l_4}c^{l_4}_{\mathbf{k}_4,\lambda_4}u^{l_4}(\mathbf{r})dVdV'. \end{aligned} \tag{6.10}$$

Because the two integrals over the unit cell are not connected anymore, they can be evaluated independently. The integral over the whole space $\mathbf{r}'$ is replaced by $\mathbf{r}-\mathbf{r}''$,

$$\begin{aligned}V^{\lambda_1,\lambda_2,\lambda_3,\lambda_4}_{\mathbf{k}_1,\mathbf{k}_2,\mathbf{k}_3,\mathbf{k}_4} \approx & \frac{1}{V^2}\int e^{\mathrm{i}(\mathbf{k}_4-\mathbf{k}_1+\mathbf{k}_3-\mathbf{k}_2)\cdot\mathbf{r}}\int e^{\mathrm{i}(\mathbf{k}_2-\mathbf{k}_3)\cdot\mathbf{r}''}V(\mathbf{r}'')dV''dV \\ & \times\sum_{l_1,l_4}\bar{c}^{l_1}_{\mathbf{k}_1,\lambda_1}c^{l_4}_{\mathbf{k}_4,\lambda_4}\int_{l^3}\bar{u}^{l_1}(\mathbf{r})u^{l_4}(\mathbf{r})dV \\ & \times\sum_{l_2,l_3}\bar{c}^{l_2}_{\mathbf{k}_2,\lambda_2}c^{l_3}_{\mathbf{k}_3,\lambda_3}\int_{l'_3}\bar{u}^{l_2}(\mathbf{r}')u^{l_3}(\mathbf{r}')dV'. \end{aligned} \tag{6.11}$$

The integral over r'' is the Fourier transform of the Coulomb potential for a fixed $\mathbf{k}_2-\mathbf{k}_3$. For a $\frac{1}{\mathbf{r}}$ potential the Fourier transform is $\frac{4\pi}{(\mathbf{k}_2-\mathbf{k}_3)^2}$. For the unit cell periodic functions $u(\mathbf{r})$ the basis functions of the k.p Hamiltonian can be used. While the connection between the k.p basis functions and the real-space electronic wave functions is incomplete, here they are evaluated over the unit cell where only the properties of an orthonormal basis are important. With this two considerations the Coulomb matrix element becomes

$$\begin{aligned}V^{\lambda_1,\lambda_2,\lambda_3,\lambda_4}_{\mathbf{k}_1,\mathbf{k}_2,\mathbf{k}_3,\mathbf{k}_4} \approx & \frac{1}{V^2}\int e^{\mathrm{i}(\mathbf{k}_4-\mathbf{k}_1+\mathbf{k}_3-\mathbf{k}_2)\cdot\mathbf{r}}dV\frac{4\pi V_0}{(\mathbf{k}_2-\mathbf{k}_3)^2} \\ & \times\sum_{l_1,l_4}\bar{c}^{l_1}_{\mathbf{k}_1,\lambda_1}c^{l_4}_{\mathbf{k}_4,\lambda_4}\delta_{l_1,l_4} \\ & \times\sum_{l_2,l_3}\bar{c}^{l_2}_{\mathbf{k}_2,\lambda_2}c^{l_3}_{\mathbf{k}_3,\lambda_3}\delta_{l_2,l_3}, \end{aligned} \tag{6.12}$$

with $V_0=\frac{e^2}{4\pi\epsilon\epsilon_0}$ and $\epsilon=12.9$ being the dielectric constant of GaAs.[101] Using the fact that the remaining integral can be written as a Kronecker-delta, Eq. (6.12) turns into:

$$V^{\lambda_1,\lambda_2,\lambda_3,\lambda_4}_{\mathbf{k}_1,\mathbf{k}_2,\mathbf{k}_3,\mathbf{k}_4} \approx \frac{1}{V}\delta_{\mathbf{k}_1,\mathbf{k}_4+\mathbf{k}_2-\mathbf{k}_3}\frac{4\pi V_0}{(\mathbf{k}_2-\mathbf{k}_3)^2}$$

$$\begin{aligned} &\times \sum_{l_1,l_4} \bar{c}^{l_1}_{\mathbf{k}_1,\lambda_1} c^{l_4}_{\mathbf{k}_4,\lambda_4} \delta_{l_1,l_4} \\ &\times \sum_{l_2,l_3} \bar{c}^{l_2}_{\mathbf{k}_2,\lambda_2} c^{l_3}_{\mathbf{k}_3,\lambda_3} \delta_{l_2,l_3} \end{aligned} \tag{6.13}$$

Evaluation of the Kronecker-deltas and substituting $\mathbf{q} = \mathbf{k}_2 - \mathbf{k}_3$ the final form of the Coulomb matrix element is

$$V^{\lambda_1,\lambda_2,\lambda_3,\lambda_4}_{\mathbf{k}_3,\mathbf{k}_4,\mathbf{q}} \approx \frac{1}{V} \frac{4\pi V_0}{\mathbf{q}^2} \sum_{l_4} \bar{c}^{l_4}_{\mathbf{k}_4+\mathbf{q},\lambda_1} c^{l_4}_{\mathbf{k}_4,\lambda_4} \sum_{l_3} \bar{c}^{l_3}_{\mathbf{k}_3-\mathbf{q},\lambda_2} c^{l_3}_{\mathbf{k}_3,\lambda_3}. \tag{6.14}$$

Inserting this matrix element into the Hamiltonian $\hat{H}_C$ gives:

$$\hat{\mathrm{H}}_C \approx \frac{1}{2} \sum_{\substack{\lambda_1,\lambda_2,\lambda_3,\lambda_4 \\ \mathbf{k}_3,\mathbf{k}_4,\mathbf{q}}} \hat{a}^{\dagger\lambda_1}_{\mathbf{k}_4+\mathbf{q}} \hat{a}^{\dagger\lambda_2}_{\mathbf{k}_3-\mathbf{q}} \hat{a}^{\lambda_3}_{\mathbf{k}_3} \hat{a}^{\lambda_4}_{\mathbf{k}_4} \times V^{\lambda_1,\lambda_2,\lambda_3,\lambda_4}_{\mathbf{k}_3,\mathbf{k}_4,\mathbf{q}} \tag{6.15}$$

The number of Coulomb matrix elements grows proportional to the fourth power of the number of involved bands λ_i. Because of the fourfold degeneracy of the valence band at the Γ-point, the Coulomb matrix elements must be calculated for $6^4 = 1296$ different band combinations. In addition, the matrix elements grow cubic in the number of included $\mathbf{k}$-points. As seen later, this can be reduced to a quadratic increase. While better, this still leads to a large number of matrix elements. Unlike the number of involved bands, the number of $\mathbf{k}$-points is not predetermined. It is therefore highly advantageous to minimize the number of grid-points to such a degree that the computational time remains within reasonable limits, but that the exciton is also reasonably well resolved.

6.2 Semiconductor Bloch Equations with Coulomb Interaction

To include the Coulomb interaction into the SBE, the Hamilton operator $\hat{\mathrm{H}}_C$ has to be included when evaluating the Heisenberg equation. A detailed evaluation can be found in Appendix A.3. Using the time-dependent Hartree-Fock approximation, the Heisenberg equations for $\hat{\mathrm{H}}_C$ is

$$\begin{aligned} \left\langle \frac{\mathrm{i}}{\hbar} \left[\hat{\mathrm{H}}_C, x^{\lambda\lambda'}_{\mathbf{k}} \right] \right\rangle = &- \frac{\mathrm{i}}{\hbar} \sum_{\substack{\mu,\mu' \\ \lambda'',\mathbf{q}}} V^{\mu\lambda''\mu'\lambda}_{\mathbf{k}+\mathbf{q},\mathbf{k},\mathbf{q}} x^{\mu\mu'}_{\mathbf{k}+\mathbf{q}} x^{\lambda''\lambda}_{\mathbf{k}} \\ &+ \frac{\mathrm{i}}{\hbar} \sum_{\substack{\mu,\mu' \\ \lambda'',\mathbf{q}}} V^{\mu\lambda'\mu'\lambda''}_{\mathbf{k}+\mathbf{q},\mathbf{k},\mathbf{q}} x^{\mu\mu'}_{\mathbf{k}+\mathbf{q}} x^{\lambda\lambda''}_{\mathbf{k}}. \end{aligned} \tag{6.16}$$

Adding the Coulomb inhomogeneity to the previously derived SBE, Eq. (3.18) in Sec. 3.2, the SBE take the form[25]

$$\frac{d}{dt}x_{\mathbf{k}}^{\lambda\lambda'} = \frac{\mathrm{i}}{\hbar}\left(\epsilon_{\mathbf{k}}^{\lambda}-\epsilon_{\mathbf{k}}^{\lambda'}\right)x_{\mathbf{k}}^{\lambda\lambda'} + \frac{i}{\hbar}\sum_{\mu}\left(\Omega_{\mathbf{k}}^{\mu\lambda}x_{\mathbf{k}}^{\mu\lambda'} - \Omega_{\mathbf{k}}^{\lambda'\mu}x_{\mathbf{k}}^{\lambda\mu}\right) - \frac{1}{T_{1/2}}x_{\mathbf{k}}^{\lambda\lambda'}, \tag{6.17}$$

with

$$\Omega_{\mathbf{k}}^{\lambda\lambda'} = \frac{e_0}{m_0}\mathbf{A}(t)\cdot\mathbf{\Pi}_{\mathbf{k}}^{\lambda\lambda'} + \sum_{\mu\mu'\mathbf{q}} V_{\mathbf{k},\mathbf{q}}^{\lambda\mu\lambda'\mu'}x_{\mathbf{k}+\mathbf{q}}^{\mu\mu'}(t). \tag{6.18}$$

The $\sum_{\mathbf{q}} V_{\mathbf{q}}$ term in Coulomb inhomogeneity couples all previous independent **k**-points. This causes at least a quadratic increase in the computational time proportional to the square of the number of k-points. In an unexcited semiconductor the valence band population $n_{\mathbf{k}}^{V} = 1$ leads to a renormalization of the band energies. For a numerical evaluation the renormalization is problematic and leads to instabilities. In this Chapter only very low intensity excitations are considered which excite a negligible population in the conduction band. To avoid the numerical instabilities, the populations are omitted in Eq. (6.18).

6.3 Cartesian Grid Consideration

To obtain a first estimation of the needed **k**-space size and resolution, a quadratic energy matrix

$$\tilde{V}_{ij} = \epsilon_i\delta_{ij} - V_{ij} \tag{6.19}$$

is constructed and diagonalized. The diagonal elements ϵ_i are the band gap energies obtained from the extended Kane model and

$$V_{ij} = V_0\frac{1-\delta_{ij}}{|\mathbf{k}_i - \mathbf{k}_j|^2} \tag{6.20}$$

the off-diagonal Coulomb matrix elements. For this method the three-dimensional **k**-space is projected onto an one-dimensional array, assigning a **k**-vector to a number i. A Cartesian grid is used for this method, thus the number of total **k**-points grows with N_k^3 and the quadratic matrix V_{ij} with N_k^6.

For the calculation of the true Coulomb matrix elements the sums of the coefficients $c_{\mathbf{k},\lambda}^{l}$ have to be evaluated. As in the case of the momentum matrix elements, the coefficients are obtained from the eigenvectors of the k.p-theory.

The sum

$$\sum_l \bar{c}^l_{\mathbf{k},\lambda} c^l_{\mathbf{k}',\lambda'} = \langle \mathbf{k}, \lambda | \mathbf{k}', \lambda' \rangle \,. \tag{6.21}$$

represents the overlap integral between two eigenvectors. Due to the normalization of the eigenvectors, the relation

$$\langle \mathbf{k}, \lambda | \mathbf{k}', \lambda' \rangle \leq 1 \tag{6.22}$$

holds. This means that the real Coulomb matrix elements are smaller than the ones used in the energy matrix V_{ij}, thus the obtained exciton energies represent an upper limit for the true ones.

The matrix V_{ij} is diagonalized and the lowest energy eigenvalue is taken as the exciton energy while the next eigenvalue is assumed to be the band gap. In Fig. 6.1 the obtained exciton binding energies are plotted. From Fig. 6.1(a) it becomes clear that at least 19^3 **k**-points are required for a sufficient converged exciton. In Fig. 6.1(b) the exciton energy reaches its minimum for $k_{max} \approx 0.25\,\text{nm}^{-1}$. For smaller values the resolved region of **k**-space is too small and parts of the exciton wave function are prematurely cut off. For higher values the **k**-space resolution becomes too bad to properly resolve the exciton wave function. The values in Fig. 6.1(b) are obtained for $N_k = 21$, thus for larger N_k the necessary k_{max} may be even larger.

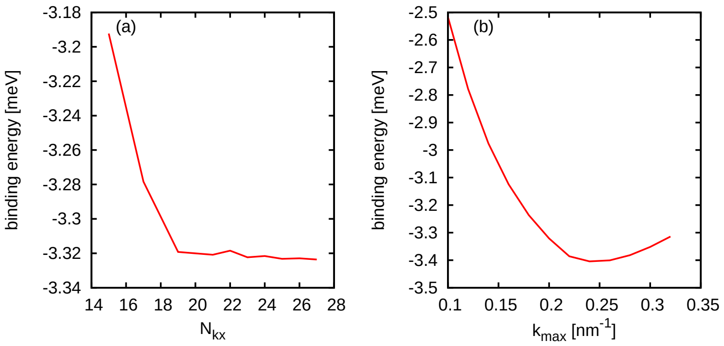

Figure 6.1: In (a) the exciton binding energy is plotted as function of N_{kx}, the number of **k**-points per axis, for $k_{max} = 0.2\,\text{nm}^{-1}$. In (b) the binding energy is plotted as function of k_{max}, calculated with $N_{kx} = 21$, which corresponds to $21^3 = 9261$ **k**-points.

While Fig. 6.1 only shows a lower estimation for the necessary Cartesian grid size, this alone is already enough. For a $N_k = 13^3$ grid the necessary Coulomb matrix would have the size of $6^4 \cdot 13^3 \cdot 13^3 = 6,255,544,462$ entries. Using double precision and complex values(16 byte per entry) this matrix would occupy a memory of approximately 100 GB. For a $N_k = 21^3$ the Coulomb matrix would have $6^4 \cdot 21^3 \cdot 21^3 = 111,152,892,816$ entries and occupy a memory of approximately 1.8 TB. For a numerical evaluation the Coulomb matrix is too large without ensuring good resolution of the exciton wave function and consequently convergence. Thus in conclusion, exciton calculations for bulk with a Cartesian grid are not feasible.

6.4 Modified Geodesic Grid

Based on the considerations in the previous section, another type of **k**-grid is required for the exciton calculations. For a parabolic band dispersion the exciton wave functions assume the form of the hydrogen wave functions, with the lowest exciton taking the shape of the $|1s\rangle$ wave function. In the k.p band structure spherical symmetry dominates, thus it can be assumed that the exciton is also dominated by spherical symmetry. As it was the case for the shift current, a spherical grid may be advantageous in resolving the exciton wave function. Therefore a geodesic grid is again applied for the calculations. A second advantage of the geodesic grid is the fact that its number of **k**-points scales linearly in either N_R or N_A. While this seemed trivial previously, at this point it becomes crucial because the Coulomb matrix scales quadratically with the number of used points. In comparison to the power of six scaling in a Cartesian grid, the quadratic scaling in a geodesic grid is numerically very advantageous.

A problem which remains is the singularity at $\mathbf{k} - \mathbf{k}' = 0$ of the Coulomb potential. From an analytic perspective normally this is not a problem because in spherical coordinates

$$\int \int V(\mathbf{k}, \mathbf{k}') k^2 \, dk \, dA \tag{6.23}$$

the k^2 from the radial element cancels the $\frac{1}{(\mathbf{k}-\mathbf{k}')^2}$ term in the potential for $\mathbf{k}' = 0$ and removes the singularity. For $k' \neq 0$ the integration space can simply be redefined to a new coordinate system $\mathbf{q}' = \mathbf{k}'$ which always ensures the removal of the singularity. For obvious reasons this cannot be done with a discrete **k**-grid used in numerics. To ensure correct results, a detailed understanding how the singularity affects the numerical stability is necessary. For this, the integral

$$\begin{aligned} I_i &= \int \frac{1}{(\mathbf{k}_i - \mathbf{k}')^2 + c^2} dV \\ &= \sum_j \frac{1}{(\mathbf{k}_i - \mathbf{k}_j)^2 + c^2} dV(k_j) \end{aligned} \tag{6.24}$$

is evaluated for various grid combinations, with $\mathbf{k}_i$ denoting $\mathbf{k}(k_i)$. The constant c represents screening and is defined as

$$c = \frac{1}{n \cdot a_B}, \tag{6.25}$$

with $a_B = 12\,\text{nm}$ being the exciton Bohr radius in GaAs and n being a scaling factor.

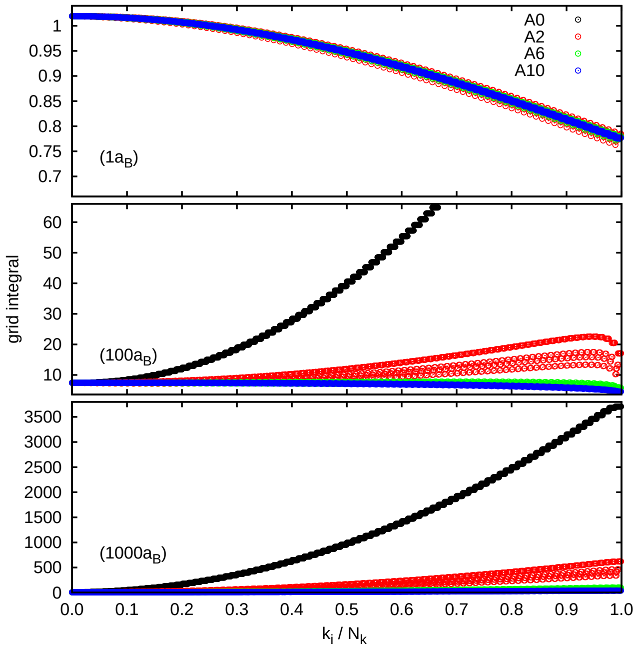

Figure 6.2: Evaluation of the Coulomb singularity according to Eq. (6.24) for a geodesic grid with $N_R = 90$ and varying N_A. The labels $A0$, $A2$, $A6$, and $A10$ correspond to grids with $N_A = 12$, $N_A = 92$, $N_A = 362$, and $N_A = 1212$, respectively. The integrals are evaluated for screening constants $c = \frac{1}{1 \cdot a_B}$, $c = \frac{1}{100 \cdot a_B}$, and $c = \frac{1}{1000 \cdot a_B}$, respectively. For better comparison the **k**-point index k_i is normalized over the total number of grid points N_k.

In Fig. 6.2 the numerical values of various geodesic grids are displayed and compared. The comparison shows that for a screening constant $c = \frac{1}{1 \cdot a_B}$ the grids yield the same numerical value with only slight discrepancy. Due to how the grid points are ordered in the program, the distance from the Γ-point for a point k_i grows with its integer value. This is reflected by the integral I_i becoming smaller for larger k_i caused by the shift of the singularity at k_i to the border of the numerical space and therefore less of it contributing to the integral. For a smaller screening constant $c = \frac{1}{100 \cdot a_B}$ the integrals I_i show high divergence for different N_A. The less grid points are on a sphere, the more the grid overestimates the integral value for higher k_i, resulting in the continuous growth of the integral value I_i till slightly before the end of the numerical space. The explanation for this lies in the volume element $dV(k_i) = \mathbf{k}_i^2 dA(k_i)$. For larger k_i the volume element $dV(k_i)$ grows quadratically which is expected for a spherical grid. For a low number of points per sphere N_A the resolution on a grid sphere is too low to properly resolve the singularity at $\mathbf{q} = 0$ and consequently the value for $\mathbf{q} = 0$ is estimated to high.

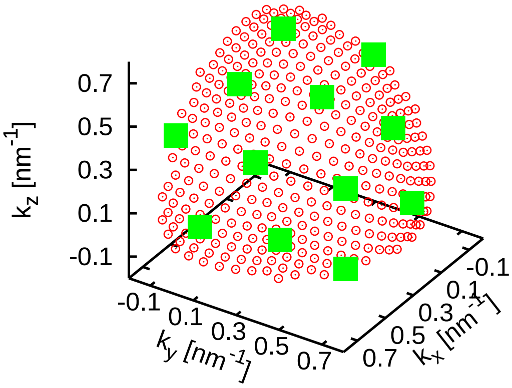

Figure 6.3: A geodesic sphere with two different angular resolutions. The green grid is the actual grid used for the matrix elements $V_{\mathbf{k},\mathbf{q}}$ and during the time integration of the SBE. The red grid is an auxiliary grid used during the calculations of the matrix elements $V_{\mathbf{k},\mathbf{q}}$ to deal with the singularity $\frac{1}{\mathbf{q}^2}$.

Consequently, a high number of points on the sphere surface is needed to properly resolve the $\frac{1}{\mathbf{q}^2}$ potential which would lead to high computational times. The problem of the singularity arises during the calculations of the Coulomb matrix elements. Thus it is advantageous to use a high resolution grid in the calculations of the matrix elements and a grid with far lower resolution in the SBE which would accomplish a great reduction of the needed computational time. In Fig. 6.3 the two grids are displayed. The green colored squares represent the main grid which is used during the SBE. The Coulomb matrix elements $V^{\lambda_1,\lambda_2,\lambda_3,\lambda_4}_{\mathbf{k},\mathbf{k}+\mathbf{q},\mathbf{q}}$ from Eq. (6.14) are calculated between the points $\mathbf{k}$ and $\mathbf{k}+\mathbf{q}$ with the coefficients $c^{\lambda}_{\mathbf{k}}$ being the $k.p$-eigenvector coefficients obtained from matrix diagonalization. To deal with the singularity $\frac{1}{\mathbf{q}^2}$ a local integral

$$I_{loc} = \int_{\mathbf{q}_{loc}} \frac{1}{\mathbf{q}'^2} d\mathbf{q}' \qquad (6.26)$$

is solved at $\mathbf{k}+\mathbf{q}$. The sub-integral goes over the auxiliary points nearest to the main point. In this work the auxiliary grid has a $N_A = 10$ which correspond to 1212 points on a sphere.

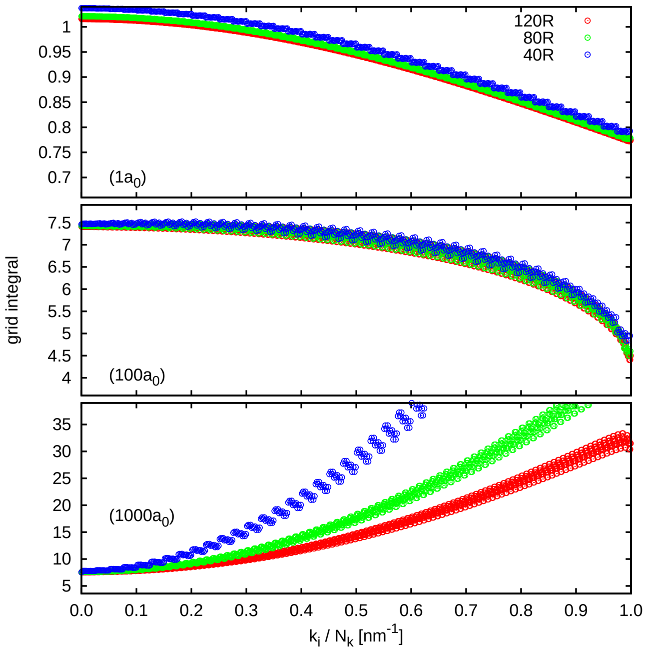

Figure 6.4: Similar to Fig. 6.2, the Coulomb singularity is evaluated according to Eq. (6.24) for a geodesic grid with $N_A = 12$ which uses a sub-grid for the evaluation of the singularity $\frac{1}{\mathbf{q}^2}$. The evaluation is done for grids with 40, 80, and 120 spheres and screening constants $c = \frac{1}{1 \cdot a_B}$, $c = \frac{1}{100 \cdot a_B}$, and $c = \frac{1}{1000 \cdot a_B}$, respectively. For better comparison the $\mathbf{k}$-point index k_i is normalized over the total number of grid points N_k.

In Fig. 6.4 the results for a geodesic grid using a sub grid are displayed and compared for different radial resolutions. For a screening constant of $c = \frac{1}{1 \cdot a_B}$ the grids are identical to the corresponding results in Fig. 6.2. This is due the screening being too large and causing the singularity $V_{\mathbf{q}=0}$ to disappear, but also due to the Coulomb matrix elements becoming too small overall. For a screening constant $c = \frac{1}{1000 \cdot a_B}$ the values heavily depend on the radial resolution and still show a large divergence. But in direct comparison to the corresponding values in Fig. 6.2 the use of a sub-grid results in an improved evaluation. For a screening constant $c = \frac{1}{100 \cdot a_B}$ the grids are converged and have improved values in comparison to a screening of $c = \frac{1}{1 \cdot a_B}$. Consequently a screening equivalent to 100 Bohr radii a_B is the optimum for numerical evaluations and used in the simulations.

6.5 Absorption Spectrum of Bulk GaAs

Based on the known effects of the Coulomb interaction at the band gap, a very well defined exciton peak and the Coulomb enhancement of the continuum absorption are expected. The literature value of the exciton binding energy $E_{lit} = 4.2\,\mathrm{meV}$[88] is quite small and as such the position of the exciton peak can be obscured by line broadening of the spectrum. Therefore the simulations are done with a long dephasing time $T_2 = 800\,\mathrm{fs}$ to minimize said line broadening. To obtain an absorption spectrum the system is excited with a quasi δ-pulse $\mathbf{E}(t) = E_0\delta(t)\mathbf{e}_x$, where $\delta(t)$ represents a function which is only unequal zero for a single time step. For δ-pulse excitation conditions the velocity gauge is unsuitable due to

$$\mathbf{A}(t) = \int dt'\delta(t') = \Theta(t) \tag{6.27}$$

which is numerical unstable. Therefore for the calculation of the linear absorption the length gauge is used. Normally the length gauge would require the inclusion of gradient terms in the SBE which is challenging due to the random phase in $\mathbf{k}$-space. But the gradient terms are higher order terms which do not contribute to the first-order polarization and thus can be omitted from first-order calculations. For testing and verification simulations are also performed with a parabolic band structure. Its known analytic solutions can be used to estimate the influence of numerical limitations such as finite k_{max} or the influence of screening. For $k.p$ band structure simulations the wave functions are used in the Coulomb and dipole matrix elements while for the parabolic band structure the wave functions are assumed to be plane waves and the dipole matrix elements are considered to be $\mathbf{k}$-independent.

In Fig. 6.5 the absorption spectra for a parabolic band structure and the GaAs band structure obtained from the extended Kane model are shown. The simulations are done with different k_{max} values to check if the used $\mathbf{k}$-space grids are large enough to achieve converged results. For the parabolic as well as for the $k.p$ band structure a grid size with $k_{max} = 0.5\,\mathrm{nm}^{-1}$ is sufficient large to ensure quantitatively converged results. Both spectra display the Coulomb enhancement and very well defined exciton peaks. For the parabolic band structure, Fig. 6.5(2a), the exciton has a binding energy of $E_{para} \approx -3.9\,\mathrm{meV}$ which is approx. 85% of the analytic value. Besides the main peak a smaller peak is visible at $E_{para2} \approx -2\,\mathrm{meV}$ which corresponds to approx. 80% of the analytic value of the light hole exciton. For the $k.p$ band structure, Fig. 6.5(2b), only one peak at $E_{k.p} \approx -3.2\,\mathrm{meV}$ is visible which is approx. 60% of the analytic value. Part of the deviation from the analytics results in the parabolic case can be explained by the finite line broadening caused by the spectrum and the light hole peak even with a very weak dephasing of $T_2 = 800\,\mathrm{fs}$.

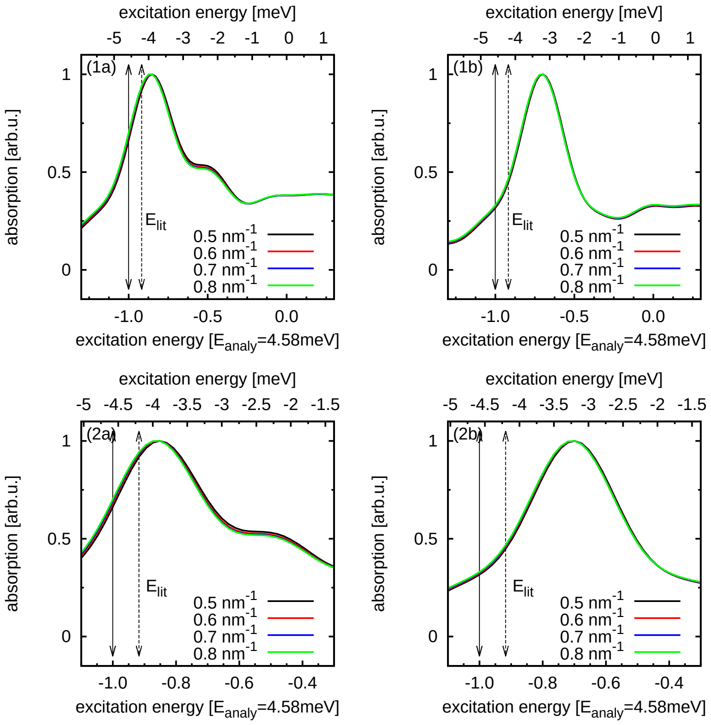

Figure 6.5: Absorption spectra for (1a) a parabolic and (1b) k.p band structure. Plotted are four different lines for different $\mathbf{k}_{max}$. (2a) and (2b) are zoomed spectra around the exciton peaks of spectra (1a) and (2a), respectively.

Besides the binding energy, the wave function form can be used to judge the accuracy of the results. To obtain the exciton wave function the system is excited with a slowly switched-on cosine excitation

$$\mathbf{E}(t) = \begin{cases} E_0 \mathbf{e}_x exp\left\{-\left(\frac{t}{\Delta t}\right)^2\right\} \cos(\omega_L t) & t < 0 \\ E_0 \mathbf{e}_x \cos(\omega_L t) & t \geq 0, \end{cases} \tag{6.28}$$

with $\Delta t = 500\,\mathrm{fs}$. Such an excitation has a very small line width which ensures that mainly the exciton will be excited by the excitation energy $\hbar\omega_L \approx E_{exc}$. For numerical stability the excitation amplitude E_0 is very small and the system has the dephasing $T_2 = 800\,\mathrm{fs}$. After a sufficient long time, here $t = 3000\,\mathrm{fs}$, the system is in a stationary state and the $\mathbf{k}$-resolved interband polarization $P_{|\mathbf{k}|}(t)$ should reflect the exciton wave function.

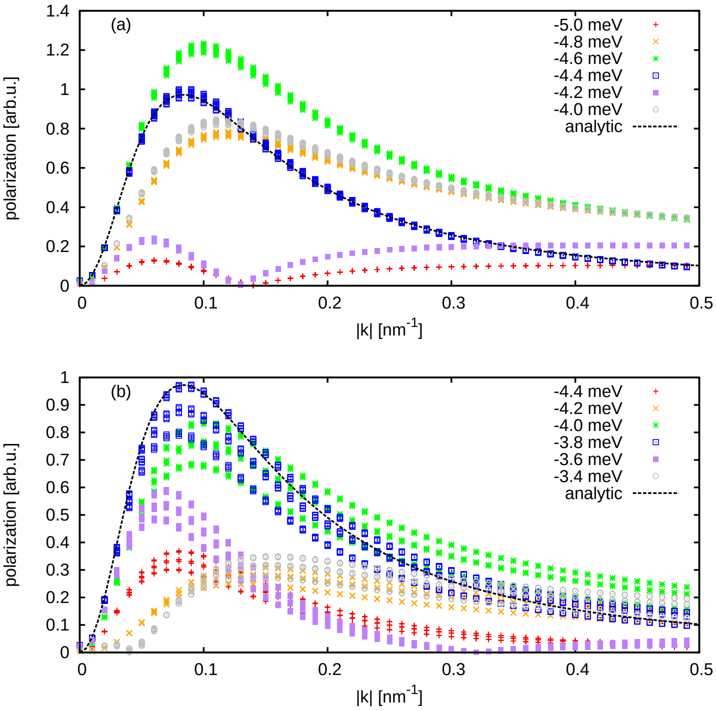

Figure 6.6: Shown is the absolute value of the interband polarization at $t = 3000\,\mathrm{fs}$ for a band structure with (a) parabolic and (b) $k.p$ dispersion. For visualization the three-dimensional $|P_{\mathbf{k}}(t)|$ are plotted as function of the radius $|\mathbf{k}|$. The interband polarization corresponds to the probability density $|\Psi(\mathbf{k})|^2 dV$.

In Fig. 6.6 the interband polarization $|P_{\mathbf{k}}(t = 3000\,\mathrm{fs})|$ is plotted as a function of the radius $\mathbf{k}$. Due to the mentioned line broadening the exciton energy position could be larger than Fig. 6.5 suggests. Therefore simulations are done with an array of small varying photon energies $\hbar\omega_L$. The results for the parabolic band structure in Fig. 6.6(a) show that the polarization has a extremely high match with the analytic solution for the density probability in $\mathbf{k}$-space

$$|\Psi(\mathbf{k})|^2 dV = \left(\frac{c}{k^2 + a_B^{-2}}\right)^2 dV \tag{6.29}$$

at a binding energy of $E_{para} = -4.4\,\mathrm{meV}$ which is $0.5\,\mathrm{meV}$ lower than the absorption spectrum suggests. This shows that the position of the exciton peak is still influence by the line broadening of the continuum states. Unlike in the parabolic band structure, the polarization in the $k.p$ band structure is highly anisotropic. In Fig. 6.6(b) the three-dimensional polarization is plotted as function of the radius $|\mathbf{k}|$. For a high isotropic polarization, see Fig. 6.6(a), the polarization appears as one thick line. In the k.p case, Fig. 6.6(b), for one excitation energy different lines are visible reflecting the anisotropy caused by the band structure and its optical matrix elements. This makes a comparison with the analytic solution more difficult. The approximately best match is at a binding energy of $E_{k.p} \approx -3.8\,\mathrm{meV}$, $0.6\,\mathrm{meV}$ lower than the spectrum value. Even with the expected deviations from the analytical solution, the comparison of the wave functions suggests that also for a $k.p$ band structure the exciton position is significantly shifted by line broadening.

For better comparison, in Fig. 6.7(a) only the results for parabolic and k.p band structure are plotted which have the highest match with the analytical result. As previously mentioned, the results for the parabolic band structure have a very good agreement with the analytical results with only minor differences due to numerics. The anisotropy of the k.p wave function leads to a decrease of the wave function to 80% at $k = \frac{1}{a_B}$ for certain directions, visible through the three distinct lines. If the maximum of the wave function at $k = \frac{1}{a_B}$ is matched to the analytic result, the k.p wave function displays slightly larger values for larger $\mathbf{k}$ vectors. This can be explained by the step size $\hbar\Delta\omega_L = 0.2\,\mathrm{meV}$ being not small enough to hit the exciton fully resonant and thus slightly exciting higher states of the continuum. But the match is sufficient enough to say that the exciton binding energy is $E_{k.p} \approx -3.8\,\mathrm{meV}$. For completion, in Fig. 6.7(b) a comparison of the radial part of the wave functions is made. Both, parabolic and k.p results, have good agreement with the analytic form, the differences are very small on the used scale.

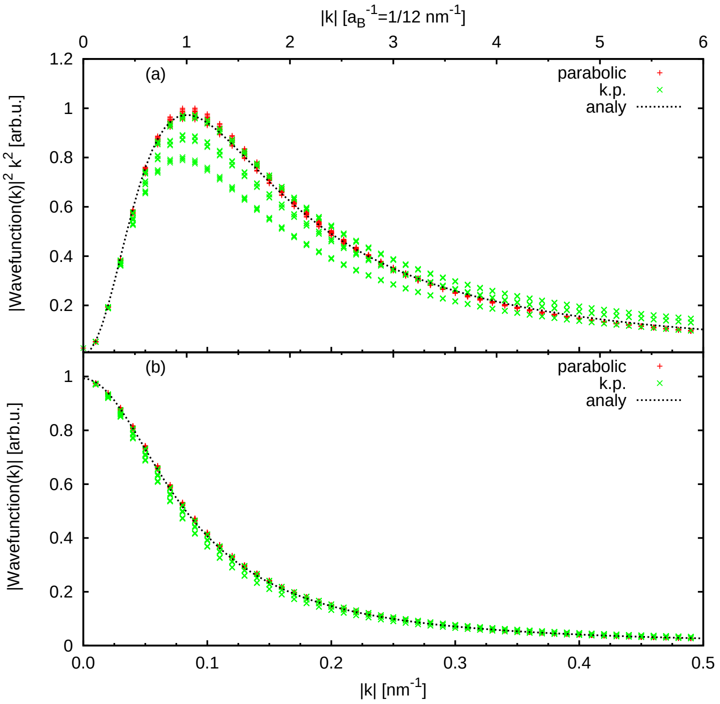

Figure 6.7: In (a) the numerically obtained parabolic and $k.p$ exciton density probabilities are compared with the analytical result for a parabolic dispersion. As in Fig. 6.6 the three-dimensional density probabilities are plotted as function of the radius $|\mathbf{k}|$. In (b) the calculated radial wave function for the parabolic and $k.p$ exciton is compared with the analytical formula $|\Psi(\mathbf{k})|^2 dV$ of Eq. (6.27).

6.6 Shift Current with Excitonic Enhancement

After verifying the exciton binding energies, the influence of the Coulomb interaction on the shift current is now analyzed. For the simulations a temperature of $T = 0.1\,\mathrm{K}$ is assumed which corresponds to a band gap of $E_{gap} = 1.517\,\mathrm{eV}$. To reduce the simulation times, a geodesic grid with $N_A = 12$ is used. This causes a low angular resolution of the grid but a comparison between $N_A = 12$ and $N_A = 48$ without Coulomb interaction shows a difference of less than 5% between the two grids. Therefore the calculated results are expected to be representative.

In Fig. 6.8 the simulated shift current with and without Coulomb interaction is shown. For below band gap excitation without Coulomb interaction, Fig. 6.8(a), the shift current is small and deviates from the analytic $E_{env}^2(t)$ shape as seen previously. With Coulomb interaction the shift current is several times larger and follows the $E_{env}^2(t)$ shape, its maximal amplitude depends on the dephasing and relaxation times T_2 and T_1. Fig. 6.8(b) shows that the exciton and the Coulomb enhancement of the continuum increases the shift current at the band edge several times. In comparison to the continuum the shift current caused by the exciton heavily depends on the dephasing in the system, for $T_2 = 100\,\mathrm{fs}$ the line broadening is so large that the exciton peak in the shift current becomes indistinguishable from the continuum.

The analysis of individual band contributions, Fig. 6.9, reveals an interesting observation. For above band gap excitation all current contributions flow in the same direction, a behavior seen for the bulk calculations without Coulomb interaction presented in Chapter 4.3. For excitation below and at the band gap the valence current changes its sign and starts to flow in the opposite direction. The behavior of the valence band current can be explained by the motion of holes. For above band excitation the created electrons and holes flow uncorrelated from each other, with the hole direction being on average opposite to that of the electron. Due to the different signs of their charge the hole current has the same sign as the electron current. For excitations near and below the band gap the electrons and holes are not uncorrelated and flow on average in the same direction, resulting in a negative current for the positively charged holes. The larger effective mass of the holes lead to a smaller displacement of the holes and consequently to a smaller shift current in the valence band than the conduction band. The line broadening of the exciton decreases the exciton shift current for all contributions for below band gap excitation, in particular, the sign changes of the valence band moves to higher energies. This indicates

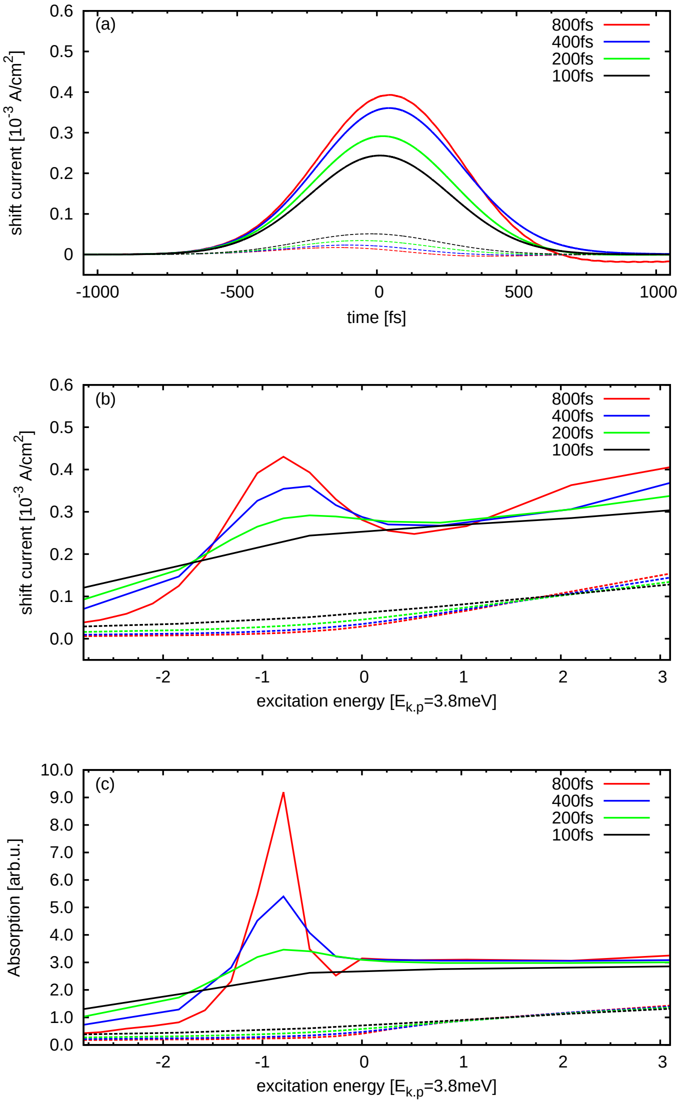

Figure 6.8: The shift current is calculated for dephasing and relaxation times $T_2 = T_1 = 800\,\mathrm{fs}$, $400\,\mathrm{fs}$, $200\,\mathrm{fs}$ and $100\,\mathrm{fs}$, respectively. The system is excited by a Gaussian pulse, $FWHM = 500\,\mathrm{fs}$, linearly polarized in (110)-direction, generating a shift current in (001)-direction. For comparison the system is simulated with, full lines, and without, dotted lines, Coulomb interaction. (a) Time evolution of the shift current for a photon energy $\hbar\omega_L = 1.515\,\mathrm{eV}$. (b) Peak shift current for different photon energies $\hbar\omega_L$ which are given in units of the analytical result for the exciton binding energy $E_{analy} = 4.58\,\mathrm{meV}$. (c) The linear absorption of the system for the respective dephasing and relaxation times.

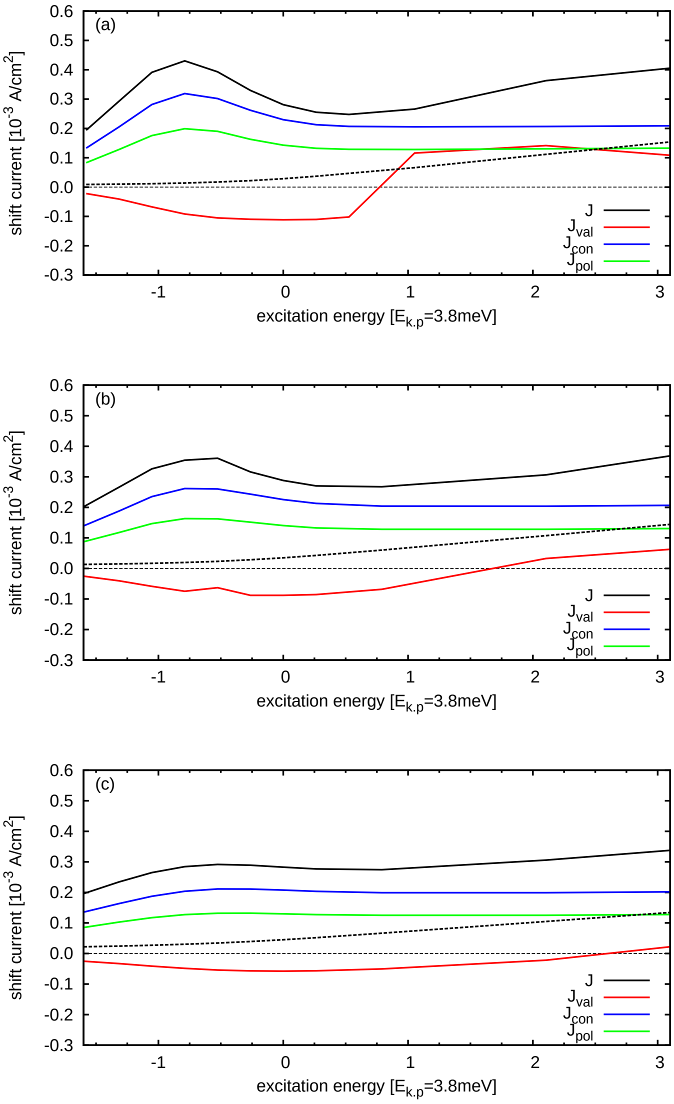

Figure 6.9: The total shift current from Fig. 6.8 and its subcurrents are displayed for dephasing and relaxation times (a) $T_2 = T_1 = 800\,$fs, (b) 400 fs, and (c) 200 fs, respectively. The maximum values of the total J, the valence J_{val}, the conduction J_{con}, and the interband current J_{pol} are shown as a function of the central excitation frequency $\hbar\omega_L$, here directly compared to the k.p exciton binding energy $E_{k.p} = 3.8\,$eV. For comparison the total shift current without Coulomb interaction, dotted black line, is included.

that with increasing line broadening the bound motion of electrons and holes is obscured by the free motion in the continuum. For above band gap excitation the continuum contributions of the conduction band and the interband polarization are constant and about $J_{con} \approx 0.2\,\mathrm{mA/cm^2}$ and $J_{int} \approx 0.1\,\mathrm{mA/cm^2}$. In comparison the valence band contributions depend on the dephasing and relaxation times T_2 and T_1 due to the intraband coherence between different valence bands which also contributes to the signal.

Another way to quantify a shift current is by the shift distance d_{shift}, the average displacement of the electron in the crystal structure. From Maxwell equations the relation

$$\mathbf{d}_{shift}(t)e_0 n(t) = \int_{-\infty}^{t} dt' \mathbf{J}_{shift}(t') \tag{6.30}$$

holds, $n(t)$ being the total conduction band population and e_0 the elementary charge. Therefore the shift distance can be calculated by

$$\mathbf{d}_{shift}(t) = \frac{\int_{-\infty}^{t} dt' \mathbf{J}_{shift}(t')}{e_0 n(t)}. \tag{6.31}$$

While the shift current $\mathbf{J}_{shift}(t)$ is an off-resonant process following the envelope of the excitation, the population $n(t)$ has resonant contributions and relaxes on its own. Therefore, Eq. (6.31) only describes the shift distance until the relaxation of the population $n(t)$ causes an artificial increase.

The bond length in GaAs, the closest distance between a gallium and an arsenic atom, is $\frac{\sqrt{3}}{4}a_0$. With the lattice constant $a_0 = 0.565\,\mathrm{nm}$, the bond length in (111)-direction is approximately 0.25 nm. In (001)-direction the bond length is approximately 0.14 nm. The simulated shift current $\mathbf{J}_{shift}$ and population density $n(t)$ are calculated for a unit volume. A GaAs unit cell is composed of two ffc-lattices, one for gallium and one for arsenic, respectively. A ffc-lattice contains four atoms, thus a GaAs unit cell contains four gallium and four arsenic atoms and consequently four transitions. In (001)-direction two transitions are each parallel which means that from the four transitions half of them do not contribute to a shift in (001)-direction. To compare the calculated shift distance with the atomic bond length a factor $n_T = 2$ is introduced in Eq. (6.31) to account for the multiple transitions:

$$\mathbf{d}_{shift}(t) = \frac{\int_{-\infty}^{t} dt' \mathbf{J}_{shift}(t')}{n_T e_0 n(t)} \tag{6.32}$$

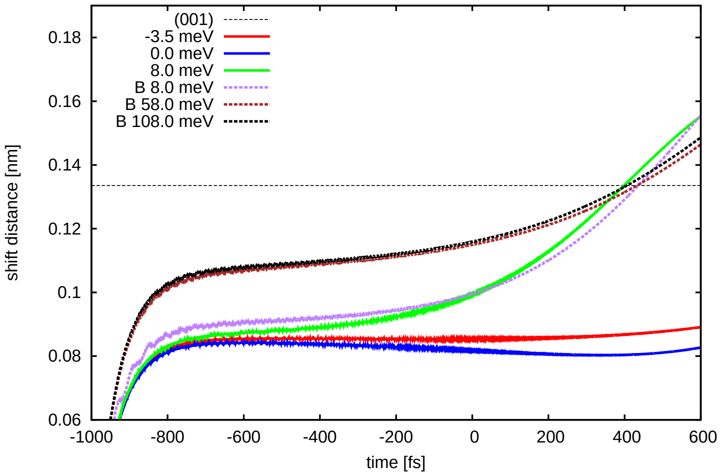

Figure 6.10: Shift current distance $d_{shift}(t)$ in (001)-direction calculated for different excitation energies $\hbar\omega_L$. The dotted B-lines represent simulations without Coulomb interaction. In addition, the bond lengths of GaAs in (001)-direction, dotted line, is included for comparison. To minimize relaxation effects of the population, the simulations are performed for a very long relaxation time $T_1 = 1600\,\mathrm{fs}$.

In Fig. 6.10 the shift distance $\mathbf{d}_{shift}(t)$ is calculated for simulations with and without Coulomb interaction. The calculated shift distances $\mathbf{d}_{shift}(t)$ settle themselves after a short time period of $\approx 150\,\mathrm{fs}$ and remain constant for a long time. Due to the mention resonant contributions and the relaxation of the population $n(t)$, the shift distances start to increase for $t > 0\,\mathrm{fs}$. Without Coulomb interaction, dotted lines in Fig. 6.10, the shift distances in (001)-direction are $d_{shift} \approx 0.09\,\mathrm{nm}$ for band gap excitation and $d_{shift} \approx 0.1\,\mathrm{nm}$ for higher excitations, approximately 63% and 70% of the bond length in (001)-direction, respectively. For band gap excitation the shift distance is slightly smaller than for higher band excitation, with the two excitation $\hbar\omega_L = 58\,\mathrm{meV} + E_{gap}$ and $\hbar\omega_L = 108\,\mathrm{meV} + E_{gap}$ having about the same shift distance.

The shift distance with Coulomb interaction, solid lines in Fig. 6.10, show a shift distance of $d_{shift} \approx 0.082\,\mathrm{nm}$ in (001)-direction, approximately 58% of the bond length. The shift distance varies with the central excitation energy $\hbar\omega$, but remains slightly smaller than the corresponding shift distance without Coulomb interaction. Despite causing a larger shift current on a whole due to increased absorption, the shift distance is slightly smaller due to the attractive interaction between holes and electrons.

It should however be mentioned that due to numerical restrains only the Coulomb interaction between the valence and conduction bands near the band gap has been considered here. While this is sufficient to describe the excitonic absorption near the band gap, the shift current is an off-resonant effect which includes higher conduction bands. It therefore may be possible that the missing Coulomb interaction between the lowest and the higher conduction bands may modify the shift current and therefore the shift distance. In the limits of this work this question cannot be answered and will require further investigation.

Chapter 7

Rectification Currents in GaAs

Besides the injection and the shift current a third current exists in non-centro symmetry semiconductor systems, the rectification current. If an electric field is applied to an insulator or semiconductor, the electric field causes a shift of the electron density along the field direction and creates a microscopic polarization inside the material. For optical frequencies the sign of the electric field changes so rapidly, that one may assume that the microscopic polarizations oscillate as fast and for larger time scales averages itself out. But in solids the electron potential $V(\mathbf{r})$ can be anharmonic, i.e.,

$$V(\mathbf{r}_0 - \Delta\mathbf{r}) \neq V(\mathbf{r}_0 + \Delta\mathbf{r}) \tag{7.1}$$

with $\mathbf{r}_0$ being the electron position of the undisturbed system. In an anharmonic potential the deflection of an electron in an oscillating electric field is different for $+\mathbf{E}$ and $-\mathbf{E}$, thus even for optical frequencies the average position $\tilde{\mathbf{r}}$ can change without causing an excitation of the electron from the valence to the conduction band. The spatial displacement of the average electron position leads to a static polarization in the material, i.e., the optical rectification $\mathbf{P}_{rec}$ and depends on the electric field strength. The optical rectification was first observed by Bass et al. in 1962 in zincblende type crystals.[102] Optical rectification can be used to generate infrared radiation in bulk GaAs.[103]

In the case of a time-varying envelope of the optical pulse, the optical rectification is time-varying too which consequently generates a microscopic rectification current $\mathbf{j}_{rec}$. As it was the case for the shift current, for linear optical excitations in certain direction the counter current $-\mathbf{j}_{rec}$ to $\mathbf{j}_{rec}$ is symmetry forbidden and thus allowing a non-vanishing rectification current $\mathbf{J}_{rec}$ to exist in the system. The rectification current was measured via THz spectroscopy in zincblende crystals and metal nano films[104, 105] and was theoretically investigated for bulk and surface currents.[35, 106, 107] In this chapter it is briefly investigated if the combined theory of k.p and SBE can be used to describe rectification currents in bulk GaAs and GaAs QW systems.

7.1 Rectification Current in Bulk GaAs

By exciting the system with linearly polarized light parallel to the (110)-direction, a rectification current is generated in (001)-direction. Like the shift current, the optical rectification $\mathbf{P}_{rec}$ follows the envelope of the optical pulse. It is the frequency $\omega = 0$ component of the total polarization

$$\mathbf{P}(t) = e \sum_{\lambda,\lambda' \neq \lambda,\mathbf{k}} \mathbf{r}_{\mathbf{k}}^{\lambda\lambda'} x_{\mathbf{k}}^{\lambda\lambda'}, \tag{7.2}$$

with $\mathbf{\Pi}_{\mathbf{k}}^{\lambda\lambda'} = \mathrm{i} m_0 \omega_{\mathbf{k}}^{\lambda\lambda'} \mathbf{r}_{\mathbf{k}}^{\lambda\lambda'}$ being the transition dipole moments. As it was the case for the shift current, the frequency filtering method around $\omega = 0$ is applied to so separate the optical rectification $\mathbf{P}_{rec}$ from the fast oscillating terms in $\mathbf{P}$. The rectification current is then given by the time derivative of $\mathbf{P}_{rec}$,

$$\mathbf{J}_{rec}(t) = \frac{\partial}{\partial t} \mathbf{P}_{rec}(t). \tag{7.3}$$

In Fig. 7.1(a) the time evolution of the rectification current is shown for the case of below, at, and above bandgap excitation. For an instantaneous response in the off-resonant limit the rectification polarization is given by[39]

$$P_{rec}^{a}(t) = \Gamma_{abc} E_{env}^{b}(t) E_{env}^{c}(t), \tag{7.4}$$

with Γ_{abc} being the rectification current tensor. For below band gap excitation the rectification current has good agreement with the expected form $J_{rec}(t) = \frac{\partial}{\partial t} P_{rec}^{a}(t) \propto \frac{\partial}{\partial t} E_{env}^{2}(t)$. For band gap excitation the rectification current becomes larger, but diverges from the form $J_{rec}(t) \propto \frac{\partial}{\partial t} E_{env}^{2}(t)$ due to resonant contributions of the band structure. For above band gap excitation the rectification is smaller in comparison with band gap excitation. This is in contrast to the shift current which for bulk systems reflects the density of states and monotonously grows in the considered energy range.

In Fig. 7.1(b) the rectification current is plotted as function of the photon

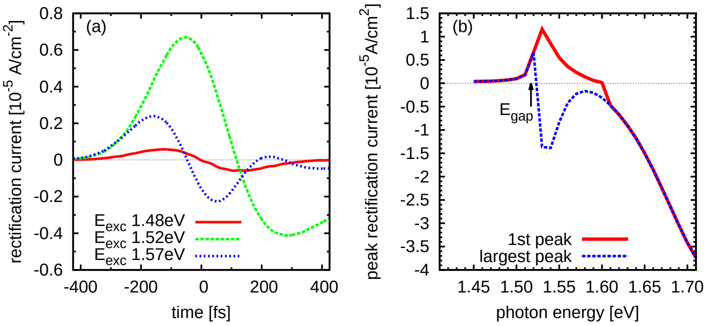

Figure 7.1: (a) Rectification current in **Z**-direction calculated for Gaussian pulses with FWHM of 300 fs and linear polarization in (110)-direction for three different photon energies $\hbar\omega_L$. (b) Rectification current as function of the photon energy. Since the rectification current transient has more than one peak, the value of the first and the largest peak of the rectification current are displayed. For the simulations the band structure is obtained for a temperature of 0.1 K which corresponds to a band gap of 1.517 eV. The dephasing and relaxation times are set to $T_1 = T_2 = 200\,\text{fs}$ to reduce dephasing and relaxation effects in the rectification current. The results were published [80].

energy $\hbar\omega_L$. For below band gap excitation no carriers are excited from the valence to the conduction band. The rectification current is predominantly created by the deflection of the electrons in the valence band which is a purely off-resonant effect, thus the agreement with Eq. (7.4). At the band gap the rectification current amplitude grows rapidly due to the resonant excitation of carriers. The electron density moves from As-atoms to the Ga-atoms resulting in a greater static polarization which contributes to the rectification current, see Fig. 4.3 in Chapter 4.1.1. Unexpectedly, the rectification current is not increasing monotonically with the photon energy but at a certain energy decreases and undergoes a current reversal. Since the rectification current transient has not one central peak, the current reversal happens at different energies depending if the first or the largest peak is used as measurement. Using the largest peak, the rectification current undergoes a current reversal slightly after the band gap, jumping at $\approx 1.53\,\text{eV}$ from positive to negative. Using the first peak, the rectification current decreases and has a zero crossing at $\approx 1.61\,\text{eV}$. After the zero crossing the rectification current rapidly grows in amplitude with growing photon energy. This sign change of the rectification current was also predicted in other theoretical studies by Nastos and Sipe[39] and was experimentally observed by Zhang[28].

7.2 Rectification Currents in (110)-grown GaAs Quantum Well Systems

Similar how the shift current was analyzed in Ch. 5.2, the rectification current is investigated in a (110)-grown QW, specifically in terms of angular dependence. As it was the case for the shift current simulations, a QW with 8 nm thickness is considered, using 12 valence bands and 28 conduction bands during the time evolution of the SBE. The used coordinates axes are $\mathbf{X} = (001)$, $\mathbf{Y} = (1\text{-}10)$, and $\mathbf{Z} = (110)$ again.

In Fig. 7.2 the system is excited with a linearly polarized pulse in the xy-plane, the angle θ lies between polarization direction and the **X**-direction. The rectification current follows the same symmetry rules as the shift current does, thus the polarization dependence in **X**-direction is described by

$$J_{rec}^{\mathbf{X}} = A\cos(2\theta) + B \tag{7.5}$$

and in **Y**-direction described by

$$J_{rec}^{\mathbf{Y}} = C\sin(2\theta). \tag{7.6}$$

The **X**-current has a offset as the shift current does, but is in comparison significantly smaller, see Chapter 5.2.1.

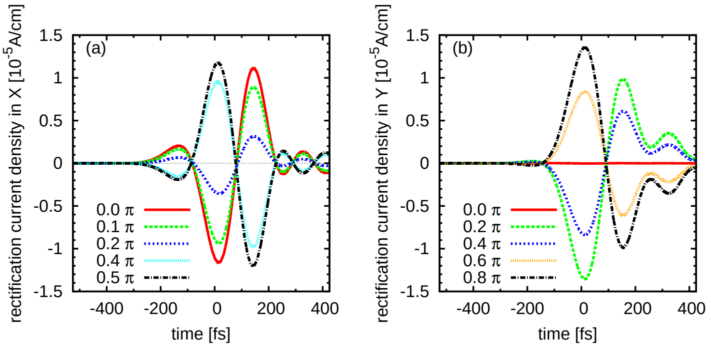

Figure 7.2: (a) Rectification currents in **X**-direction calculated for a linear polarized Gaussian pulses with central frequency corresponding to 1.6 eV, a FWHM of 200 fs, and different θ which is the angle between the **X**-axis and the linear polarization direction of the pulse. (b) Corresponding rectification currents in **Y**-direction. As in the case of the shift current calculations, dephasing and relaxation times of $T_1 = T_2 = 200\,\text{fs}$ are considered. The results were published [80].

Chapter 8

Real-Space Mapping of Shift Currents

In the combined theory of k.p and SBE the shift current is calculated in **k**-space via

$$\mathbf{J}_{shift}(t) = \int_{\Omega k} \mathbf{j}_{\mathbf{k}}(t)\, d\mathbf{k}. \tag{8.1}$$

This method allows for the calculation of the shift current in a unit volume, but does not contain any real-space information. Given that the shift current is created by the spatial shift of the electrons in the inversion asymmetric crystal structure of GaAs, it would be interesting if the method could be extended to provide a real-space visualization of the shift current and if the real-space shift current would display the properties expected by the symmetry considerations. In previous research k.p theory was incorporated in real-space simulations, but the application was restricted to the calculation of spatially resolved band energies.[108, 109]

8.1 Theory

In general an operator $\hat{a}$ and an eigenvector $|i\rangle$ have the relation

$$\hat{a}|i\rangle = a_i|i\rangle, \tag{8.2}$$

with a_i being the eigenvalue. Consequently, the operator $\hat{a}$ can be written as

$$\hat{a} = \sum_i a_i|i\rangle\langle i|. \tag{8.3}$$

Applying Eq. (8.3) on the shift current, the shift current operator in the extended Kane model has the explicit form

$$\begin{aligned}\hat{\mathbf{j}}^{ll'}(t,\mathbf{k}) =&\mathbf{j}^{ll'}(t,\mathbf{k})|l,\mathbf{k}\rangle\langle l',\mathbf{k}| \\ =&\mathbf{\Pi}_{\mathbf{k}}^{ll'}x_{\mathbf{k}}^{ll'}(t)|l,\mathbf{k}\rangle\langle l',\mathbf{k}|.\end{aligned} \tag{8.4}$$

The shift current operator consists of the momentum matrix elements $\mathbf{\Pi}_{\mathbf{k}}^{ll'}$ and the time evolution matrix of the system $x_{\mathbf{k}}^{ll'}(t)$ which is calculated via the SBE. The Ket-vectors $|l,\mathbf{k}\rangle$ are the band structure eigenvectors obtained from matrix diagonalization and can be written as

$$|l,\mathbf{k}\rangle = \sum_n c_l^n(\mathbf{k})|n\rangle, \tag{8.5}$$

with $|n\rangle$ being the 14×14 eigenbasis of the extended Kane Hamiltonian. Using Eq. (8.5) the general shift current operator is

$$\hat{\mathbf{j}}^{ll'}(t,\mathbf{k}) =\mathbf{\Pi}_{\mathbf{k}}^{ll'}x_{\mathbf{k}}^{ll'}(t)\sum_{mm'} c_l^m(\mathbf{k})\bar{c}_{l'}^{m'}(\mathbf{k})|m\rangle\langle m'|. \tag{8.6}$$

If an operator $\hat{a}$ is applied on a Ket $|j\rangle$, which is **not** an eigenvector of the operator, the result will be

$$\hat{a}|j\rangle = \hat{a}\sum_i c_{ji}|i\rangle = \sum_i c_{ji}a_i|i\rangle. \tag{8.7}$$

The c_{ji} are the expansion coefficients of writing the Ket $|j\rangle$ in the eigenbasis $|i\rangle$ of the operator $\hat{a}$, see Eq. (8.3). Using the definition of the expectation value

$$\langle a_j\rangle = \langle j|\hat{a}|j\rangle \tag{8.8}$$

it is clear that c_{ji}^2 are the probabilities to measure a_i. Using Eq. (8.7) & Eq. (8.8) it must be possible to write the space expectation value as

$$\langle \mathbf{r}_j\rangle = \langle j|\hat{\mathbf{r}}|j\rangle = \langle j|\sum_i \mathbf{r}_i|i\rangle\langle i||j\rangle. \tag{8.9}$$

From this it becomes obvious that $\langle i|j\rangle = \Psi_j(\mathbf{r}_i)$, or in other words $\langle \mathbf{r}|j\rangle$ is the real-space representation of the wave function $|\Psi_j\rangle$. Using Eq. (8.8) again, the expectation value

$$\langle a_{\mathbf{r}}\rangle = \langle \mathbf{r}|\hat{a}|\mathbf{r}\rangle \tag{8.10}$$

is consequently the real-space representation of the observable a, or in other words $a(\mathbf{r})$. Using the shift current operator Eq. (8.6) and Eq. (8.10) the real-space representation of the shift current is

$$\mathbf{j}_{\mathbf{k}}^{ll'}(t,\mathbf{r}) = \left\langle \mathbf{r} \middle| \hat{\mathbf{j}}^{ll'}(t,\mathbf{k}) \middle| \mathbf{r} \right\rangle = \mathbf{\Pi}_{\mathbf{k}}^{ll'} x_{\mathbf{k}}^{ll'}(t) \sum_{mm'} c_l^m(\mathbf{k}) \bar{c}_{l'}^{m'}(\mathbf{k}) \underbrace{\langle \mathbf{r}|m\rangle}_{\Psi_m(\mathbf{r})} \underbrace{\langle m'|\mathbf{r}\rangle}_{\bar{\Psi}_{m'}(\mathbf{r})}, \qquad (8.11)$$

with $\Psi_{m'}(\mathbf{r})$ being the real-space representations of the Bloch wave function at the Γ-point $\mathbf{k} = 0$. By integrating over $\mathbf{k}$-space, the real-space shift current $\mathbf{J}^{ll'}(t,\mathbf{r})$ is obtained.

Table 8.1: Angular momentum eigenfunctions of the extended Kane model.

Γ_8^c	$\left\vert \tfrac{3}{2} \tfrac{3}{2} \right\rangle_{c'} = -\tfrac{1}{\sqrt{2}} \left\vert \begin{pmatrix} X' + \mathrm{i}Y' \\ 0 \end{pmatrix} \right\rangle$	$\left\vert \tfrac{3}{2} \tfrac{1}{2} \right\rangle_{c'} = \tfrac{1}{\sqrt{6}} \left\vert \begin{pmatrix} 2Z' \\ -X' - \mathrm{i}Y' \end{pmatrix} \right\rangle$
	$\left\vert \tfrac{3}{2} -\tfrac{1}{2} \right\rangle_{c'} = \tfrac{1}{\sqrt{6}} \left\vert \begin{pmatrix} X' - \mathrm{i}Y' \\ 2Z' \end{pmatrix} \right\rangle$	$\left\vert \tfrac{3}{2} -\tfrac{3}{2} \right\rangle_{c'} = \tfrac{1}{\sqrt{2}} \left\vert \begin{pmatrix} 0 \\ X' - \mathrm{i}Y' \end{pmatrix} \right\rangle$
Γ_7^c	$\left\vert \tfrac{1}{2} \tfrac{1}{2} \right\rangle_{c'} = -\tfrac{1}{\sqrt{3}} \left\vert \begin{pmatrix} Z' \\ X' + \mathrm{i}Y' \end{pmatrix} \right\rangle$	$\left\vert \tfrac{1}{2} -\tfrac{1}{2} \right\rangle_{c'} = -\tfrac{1}{\sqrt{3}} \left\vert \begin{pmatrix} X' - \mathrm{i}Y' \\ -Z' \end{pmatrix} \right\rangle$
Γ_6^c	$\left\vert \tfrac{1}{2} \tfrac{1}{2} \right\rangle_{c} = \left\vert \begin{pmatrix} S \\ 0 \end{pmatrix} \right\rangle$	$\left\vert \tfrac{1}{2} -\tfrac{1}{2} \right\rangle_{c} = \left\vert \begin{pmatrix} 0 \\ S \end{pmatrix} \right\rangle$
Γ_8^v	$\left\vert \tfrac{3}{2} \tfrac{3}{2} \right\rangle_{v} = -\tfrac{1}{\sqrt{2}} \left\vert \begin{pmatrix} X + \mathrm{i}Y \\ 0 \end{pmatrix} \right\rangle$	$\left\vert \tfrac{3}{2} \tfrac{1}{2} \right\rangle_{v} = \tfrac{1}{\sqrt{6}} \left\vert \begin{pmatrix} 2Z \\ -X - \mathrm{i}Y \end{pmatrix} \right\rangle$
	$\left\vert \tfrac{3}{2} -\tfrac{1}{2} \right\rangle_{v} = \tfrac{1}{\sqrt{6}} \left\vert \begin{pmatrix} X - \mathrm{i}Y \\ 2Z \end{pmatrix} \right\rangle$	$\left\vert \tfrac{3}{2} -\tfrac{3}{2} \right\rangle_{v} = \tfrac{1}{\sqrt{2}} \left\vert \begin{pmatrix} 0 \\ X - \mathrm{i}Y \end{pmatrix} \right\rangle$
Γ_7^v	$\left\vert \tfrac{1}{2} \tfrac{1}{2} \right\rangle_{v} = -\tfrac{1}{\sqrt{3}} \left\vert \begin{pmatrix} Z \\ X + \mathrm{i}Y \end{pmatrix} \right\rangle$	$\left\vert \tfrac{1}{2} -\tfrac{1}{2} \right\rangle_{v} = -\tfrac{1}{\sqrt{3}} \left\vert \begin{pmatrix} X - \mathrm{i}Y \\ -Z \end{pmatrix} \right\rangle$

In general the k.p Bloch functions lack a complete real-space description. The angular part of the wave function is developed in the basis of the angular momentum eigenfunctions $|m,\mathbf{r}\rangle$, also known as the spherical harmonics, see Table 8.1, the radial part is missing in the theory. To complete the real-space representation of the Bloch wave functions, the radial part is required and has to be obtained from somewhere else. Here the radial part is calculated from the real-space wave functions $\left|\Psi_m^{DFT}(\mathbf{r})\right|^2$ obtained from density functional theory calculations, at this point the author wants to thank Andreas Lücke for providing the necessary density functional theory (DFT) calculations.

The radial part is calculated by

$$\Psi_m^{pseudo-rad}(\mathbf{r}) = \sqrt{|\Psi_m^{DFT}(\mathbf{r})|^2}. \qquad (8.12)$$

The DFT wave functions contain both the radial and the angular part of the wave function. To not include the angular part of the wave function twice, the wave functions obtained from Eq. (8.12) are divided by the absolute value of the angular momentum eigenfunctions,

$$\Psi_m^{rad}(\mathbf{r}) = \frac{\Psi_m^{pseudo-rad}(\mathbf{r})}{\sqrt{|\langle m, \mathbf{r}|m, \mathbf{r}\rangle|}}. \tag{8.13}$$

The Bloch wave functions are then obtained by combining the radial part with the angular momentum eigenfunctions,

$$\Psi_m(\mathbf{r}) = \Psi_m^{rad}(\mathbf{r}) \cdot |m, \mathbf{r}\rangle. \tag{8.14}$$

The so-obtained Ψ_m are used for the real-space calculations. Besides the Ψ_m Eq. (8.11) contains the expansion coefficients $c_l^m(\mathbf{k})$ from the k.p vectors. Because the matrix diagonalization process allows for a random phase factor φ_l for each k.p vector $|l\rangle$ at each $\mathbf{k}$-point, the expansions coefficients would have to be phase corrected before an integration over $\mathbf{k}$-space can be performed. Instead of doing a phase correction, Eq. (8.11) is modified into

$$\mathbf{j}_{\mathbf{k}}^{ll'}(t, r) = \left\langle \mathbf{r} \middle| \hat{\mathbf{j}}^{ll'}(t, \mathbf{k}) \middle| \mathbf{r} \right\rangle = \mathbf{\Pi}_{\mathbf{k}}^{ll'} x_{\mathbf{k}}^{ll'}(t) \left| \sum_{mm'} c_l^m(\mathbf{k}) \bar{c}_l^{m'}(\mathbf{k}) \Psi_m(r) \bar{\Psi}_{m'}(r) \right|, \tag{8.15}$$

where the problem of the random phase is treated by just considering the absolute value of the coefficients. This approximation leads to the problem of ignoring the natural change of the phase in $\mathbf{k}$-space, but is sufficient for a first trial.

8.2 Results

Using Eq. (8.15) the real-space representation of the shift current is calculated. The used DFT-wave functions have a spatial resolution of 31^3 grid points. For each real-space point Eq. (8.15) has to be evaluated and summed up over the whole $\mathbf{k}$-space. In Fig. 8.1 the shift current created by the interband polarization is shown inside the GaAs primitive cell. The real-space picture shows shift current contributions around the As- and Ga-atoms. For an excitation in (010)-direction the GaAs symmetry does not allow a shift current to remain. In the corresponding picture above and below the As atom positive and negative current contributions are visible, with the negative blue contributions being slightly larger. For (110)-polarization, the upper picture, two current density clouds are visible, reaching from below the As-atom to the two Ga-atoms above.

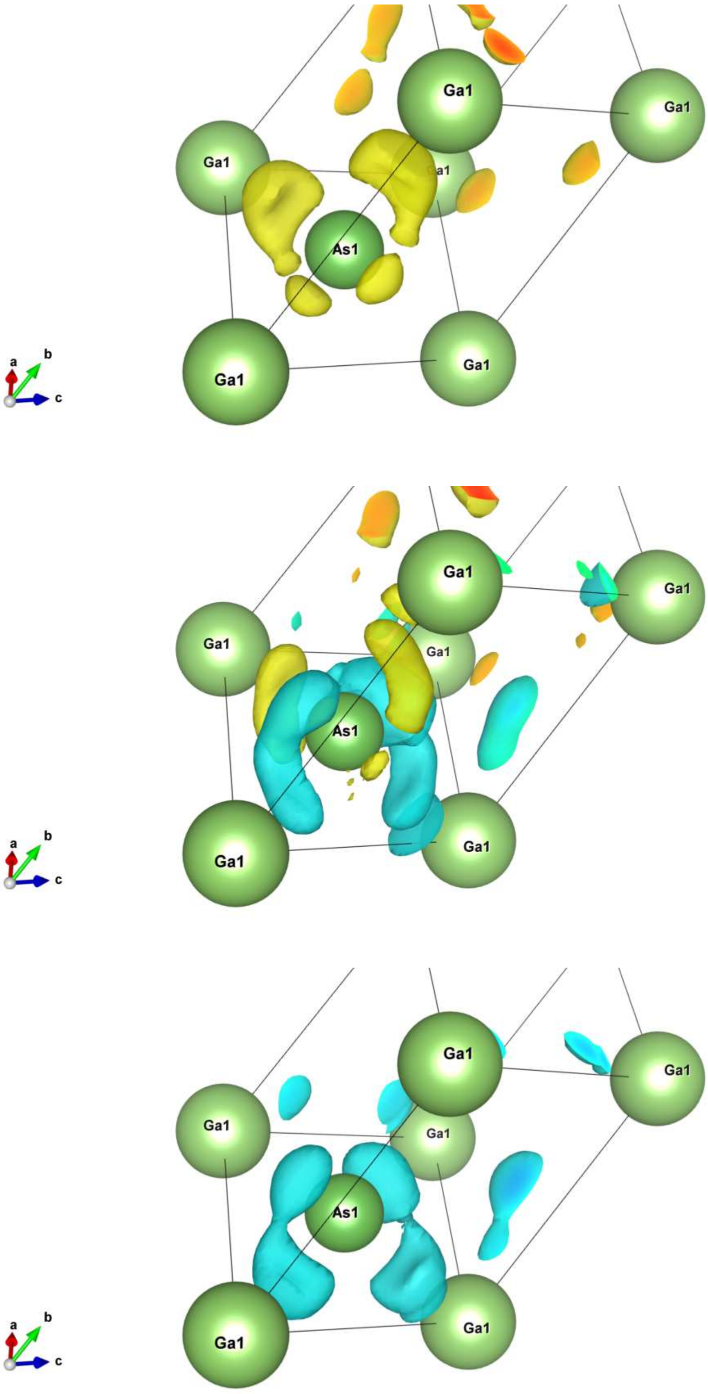

Figure 8.1: The shift current $J_z(\mathbf{r})$ in the primitive cell of GaAs. The vectors a, b, and c are the unit vectors of the primitive cell and point in (-101), (011), (-110). The shift current is calculated for $t = 0$. In the upper, middle, and lower picture the shift current, created by the interband polarization, is depicted for a linear polarized excitation in (110), (010), and (-110) which generates a shift current in +z, no shift current, and -z-direction, respectively. Yellow marks positive and blue negative current contributions. The pictures were made using the atomic density visualization program VESTA.

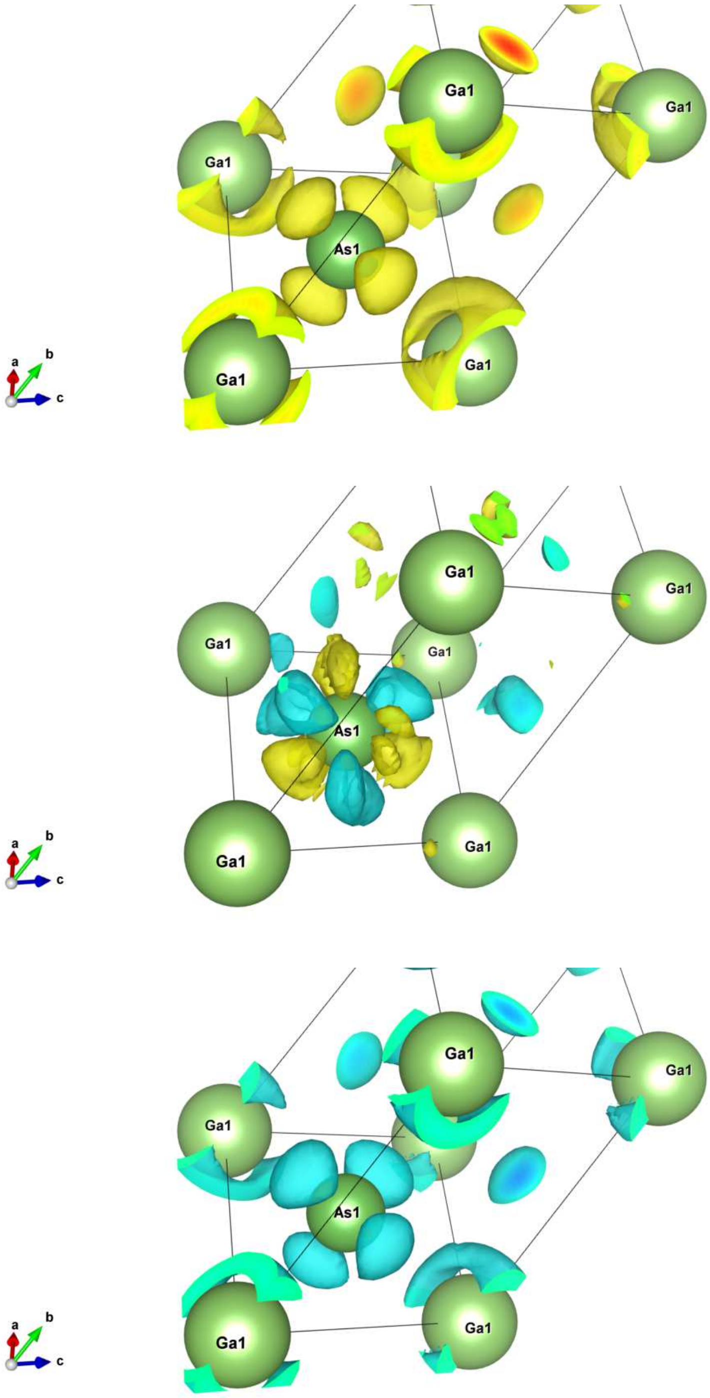

Figure 8.2: The shift current $J_z(\mathbf{r})$ in the primitive cell of GaAs. The vectors a, b, and c are the unit vectors of the primitive cell and point in (-101), (011), (-110). The shift current is calculated for $t = 0$. In the upper, middle and lower picture the shift current, created by the whole band structure, is depicted for a linear polarized excitation in (110), (010), and (-110) which generates a shift current in +z, no shift current, and -z direction, respectively. Yellow marks positive and blue negative current contributions. The pictures were made using the atomic density visualization program VESTA.

The real-space picture shows that the shift current has a positive contribution, i.e, it flows in +z-direction and that it travels to the two As-atoms parallel to the optical (110)-excitation, respectively. Both of this are in agreement with the previous established shift current symmetries. For (1-10)-polarization, the lower picture, the shift current manifests as two large current density clouds reaching from above the As-atom to the two lower Ga-atoms. It visualizes how the current flows in -z-direction.

The GaAs-structure has to be invariant under its symmetry operation. Consequently, the spatial shift current has to be invariant under certain GaAs-symmetry operation. For a shift current in z-direction the spatial shift current has to be invariant regarding mirroring at the As-atom in (110) and (1-10)-direction. Another symmetry is the 90°-rotation around and additional mirroring in (001)-direction at the As-atom. This symmetry describes how the shift current flows in +z and -z-direction for optical (110) and (1-10)-polarization. The spatial shift currents in Fig. 8.1 partially break both of this symmetries. For the simple mirror symmetry the spatial pictures show only minuscule asymmetries. For second symmetry the +z and -z shift current pictures show large differences. This differences are explained by the approximation made in Eq. (8.15) where the random phase problem was treated by just considering the absolute values. This approximation does not account for the intrinsic phase change in **k**-space.

In Fig. 8.2 the full shift current, i.e. valence, conduction and interband contributions, is depicted. For (100)-polarization the partial shift current show positive and negative contributions, canceling each other out. For (110)-polarization, the upper picture, a positive current density cloud surrounds the Ga-atoms. Around the As-atom four density clouds are visible, with the cloud above the As-atom being slightly closer to each other. For (1-10)-polarization, the lower picture, the current density cloud below the As-atom are slightly closer to each other. The spatial picture of the whole current is not as intuitive as the interband current in Fig. 8.1, but with the clouds in the shift current direction being slightly closer to each other it still partially agrees with the conception of the shift current moving from the As-atom to the two Ga-atoms above.

In Fig. 8.3(a) the spatial shift current is integrated over the primitive cell for varying polarizations angle θ which is the angle between the x-axis and the linear polarization. As expected, the real-space shift current follows approximately a $\sin(2\theta)$ dependence. In theory the x- and y-currents should vanish for the used excitation conditions, but in Fig. 8.3(a) non-vanishing contributions

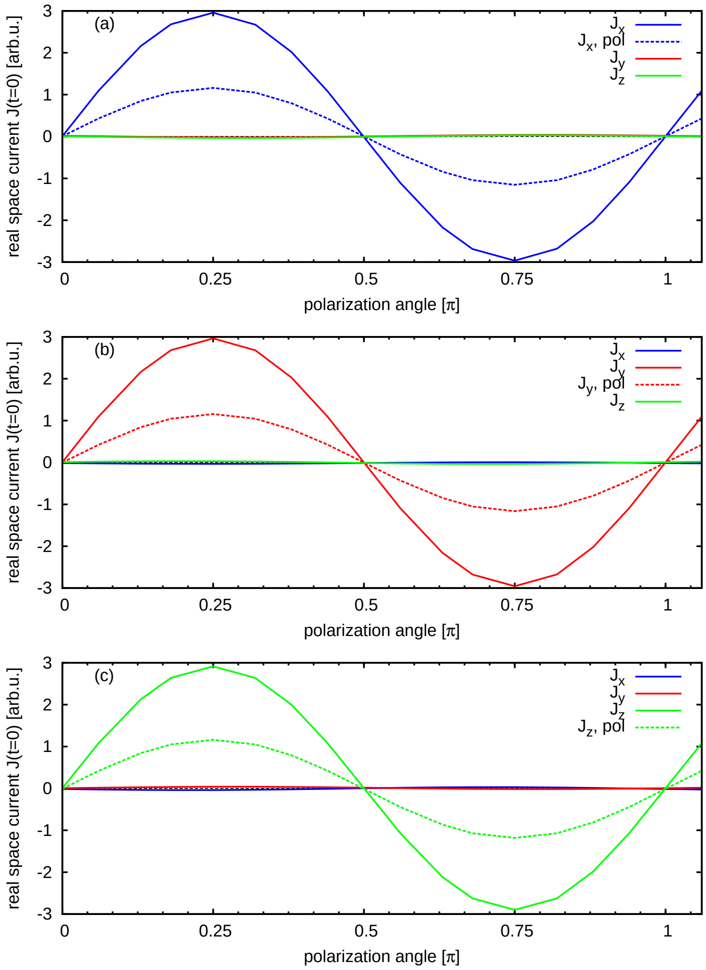

Figure 8.3: The x-, y-, and z-currents are integrated over the GaAs primitive cell. Displayed are the integrated current for varying linear polarizations in (a) the xy-plane and (b) the xz-plane. The currents are shown as a function of the polarization angle between the x-axis and the linear polarization.

are visible. However, these contributions are much smaller as the shift current in z-direction. In addition to the full current, also the current only created by the interband polarization is shown. It too follows the $\sin(2\theta)$ dependence, but only makes up for $\approx 30\%$ of the total current.

Despite only considering the absolute value of the complex k.p eigenvectors, the novel method allows for a visualization of a real-space shift current which is in agreement with the established symmetry rules for the shift current. In addition, the shift current created by interband polarization current shows in real-space how the current *flows* between the As-atom and the Ga-atom.

Chapter 9

Conclusion

In this work it was shown that the combined theory of k.p perturbation theory and the semiconductor Bloch equations is suitable to describe the shift and the rectification current in GaAs based systems. The theory reproduces the known symmetry properties of the shift current and its linear dependence regarding the intensity of the optical excitation in the low intensity limit. The theory also qualitatively reproduces the emergence of alternating shift currents for optical excitation using chirped pulses, which has been observed in experiments. A band analysis of the shift current reveals that the shift current is created by the off-resonant interaction of the lowest conduction band with higher conduction bands. The theory predicts that high excitation intensities will lead to time-dependent current reversals of the shift current, concurrent with Rabi-oscillation in the population. It also predicts for coherent two pulse excitation a small intrinsic phase in the shift current because of the formation of fringes in the population.

The extended Kane model reproduces the band structure of GaAs around the Γ-point, but becomes incorrect for larger **k**-values. Consequently, in this work the shift current simulations have been limited to excitations around the Γ-point. For full Brillouin zone calculation an expansion of the theory is possible by combining the SBE with full band structure k.p models or density functional theory. Due to the symmetry of the zinceblende band structure in **k**-space, excitation at the Brillouin zone borders could lead to new unexpected effects in the shift current. A full band structure theory could also be used to investigate other effects, e.g., Bloch oscillations.[55] Thus it represents a promising research topic for future investigation.

By using a non-standard geodesic grid, it is possible to include Coulomb interaction for a three-dimensional band structure. The calculations have the advantage of high convergence and comparably small numerical effort. A converged exciton has been observed in simulations with a parabolic and a k.p band structure. The anisotropy of the k.p band structure reflects itself in a anisotropy of the exciton wave function, deviating from the radial-symmetric $|1s\rangle$ wave function known from hydrogen model. The Coulomb interaction leads to a strong enhancement of the absorption and consequently the shift current. However, the binding electron-hole interaction for below band gap excitation leads to a negative hole current which results in a reduction of the shift distances in comparison with simulations without Coulomb interaction.
Due to numerical demands the Coulomb interaction with the higher conduction bands is not included in this work. Since the higher conduction bands are responsible for the creation of the shift current, the inclusion of the higher bands via Coulomb interaction may cause additional effects in the shift current and has to be further investigated. Besides shift current, the inclusion of Coulomb interaction allows for the investigation of other excitonic effects at the band gap, e.g., two-color excitation experiments.[94]

By using the envelope function approach the extended Kane model can be modified to describe the band structure in a quantum well system. For (110)-grown quantum well(QW) systems the shift current was analyzed and a new shift current tensor element was observed which does not exist in bulk GaAs. In addition, a sign change of the shift current was observed for higher excitation energies and a **k**-space resolved analysis revealed the importance of band crossing in the shift current. Both of these effects were observed in experiment, validating the applicability of the combined theory for QW systems.
How the Coulomb interaction affects the shift current in QW systems has not been investigated in this work, but the surprising results for bulk as well as the higher exciton binding energies make this an interesting research topic. The band crossing in (110)-grown QW systems is responsible for a non-vanishing Berry-phase in the band structure which also represents a further topic for future research.[110, 111]

Using a novel approach which combines k.p theory with DFT wave functions, the shift current is visualized in real-space on an atomic scale. The calculated shift currents in real-space obey the shift current symmetries and show the electron transfer from arsenic to gallium in the primitive cell. However, the random phase of the wave function in **k**-space was treated by only considering the absolute value. This leads to an approximation error which appears as a small symmetry break between the + and - current in real-space. Consequently, a better treatment of the random phase is expected to lead to further improvement of the method. While the method was developed for shift currents, it can be adapted for the real-space visualization of all effects described by the combined theory of k.p method and SBE, e.g., excitonic resonances and rectification currents.

Appendix A

Additional Theory Considerations

A.1 Theoretical Basics

A.1.1 Theory of Invariants

Applying a symmetry operation $\hat{S}_G$ of system G on its Hamiltonian gives back the Hamiltonian itself. Thus it must be possible to construct the Hamiltonian in terms of symmetry invariant components.[47, 48] In point group theory a symmetry class is expressed by a number of irreducible representations Γ_i. A matrix, which expresses a symmetry operation of the system, can be decomposed into a set of smaller matrices which transform according to an irreducible representation of the symmetry class. The irreducible representation represent a basis in which all symmetry matrices and invariant expressions can be developed. Given the bands α and β, which transform according to the irreducible representations Γ_α and Γ_β, the Hamiltonian $\hat{\mathrm{H}}_{\alpha\beta}$ has to transform according to the irreducible representation Γ_κ contained in the product representation $\Gamma_\alpha \otimes \Gamma_\beta^\dagger$. Therefore $\hat{\mathrm{H}}_{\alpha\beta}$ can be expanded as a superposition of its invariant expressions $I_{\kappa\lambda\mu}$

$$\hat{H}_{\alpha\beta} = \sum_{\kappa,\lambda,\mu} a^{\alpha\beta}_{\kappa\lambda\mu} I_{\kappa\lambda\mu}, \tag{A.1}$$

where the index κ sums up over all invariant expressions transforming according to the irreducible representation Γ_κ. The indices λ and μ sum over degeneracies either in Γ_κ or in the point group itself. Combining this approach with perturbation theory allows for a straightforward formulation of a finite dimensional Hamiltonian.

A.1.2 Löwdin Partitioning

Normally it is not possible to distinguish between degenerate states in perturbation theory. Löwdin partitioning is a quasi-degenerate perturbation theory which starts by a separation of the eigenstates $|\phi_n\rangle$ of a Hamiltonian $\hat{\mathrm{H}}_0$ into two weakly interacting subsets A and B.[112, 113] The full Hamiltonian $\hat{\mathrm{H}}$ is

given by

$$\hat{\mathrm{H}} = \hat{\mathrm{H}}_0 + \hat{\mathrm{H}}^{'}, \tag{A.2}$$

with $\hat{\mathrm{H}}^{'}$ being the perturbation. In quasi-degenerate perturbation theory it is assumed that an unitary operator $e^{\hat{S}}$ can be found with the property that the matrix elements between the sets A and B

$$\langle \varphi_A | e^{-\hat{S}} \hat{\mathrm{H}} e^{\hat{S}} | \varphi_B \rangle = \langle \varphi_A | \hat{\mathrm{H}}_d + \hat{\mathrm{H}}_n | \varphi_B \rangle \tag{A.3}$$

vanish up to the desired order in $\hat{\mathrm{H}}^{'}$. A block-diagonal Hamiltonian $\hat{\mathrm{H}}_d$ and a non-block-diagonal Hamiltonian $\hat{\mathrm{H}}_n$ is introduced. The full Hamiltonian is divided up into

$$\hat{\mathrm{H}} = \hat{\mathrm{H}}_0 + \hat{\mathrm{H}}_1 + \hat{\mathrm{H}}_2. \tag{A.4}$$

The Hamiltonian $\hat{\mathrm{H}}_1$ has non-zero elements only *within* the sets A and B while $\hat{\mathrm{H}}_2$ only *between* A and B, respectevely. The unitary operator $e^{-\hat{S}}$ has to fulfill the conditions

$$\hat{\mathrm{H}}_d = e^{-\hat{S}} \left(\hat{\mathrm{H}}_0 + \hat{\mathrm{H}}_1 + \hat{\mathrm{H}}_2 \right) e^{\hat{S}}, \tag{A.5}$$

$$\hat{\mathrm{H}}_n = 0. \tag{A.6}$$

Using $e^{\hat{S}} = 1 + \hat{S} + \frac{1}{2!}\hat{S}^2 + ...$ and the ansatz $\hat{S} = \hat{S}^{(1)} + \hat{S}^{(2)} + ...$ $\hat{S}$ can be develop up to the jth order. The perturbed Hamiltonian is then

$$\hat{\mathrm{H}}_d = \hat{\mathrm{H}}_d^{(0)} + \hat{\mathrm{H}}_d^{(1)} + \hat{\mathrm{H}}_d^{(2)} + ... \tag{A.7}$$

A.1.3 Matrix Expressions

Here the matrices of the extended Kane model are listed.

Table A.1: Explicit form of matrices used in the invariant form of the extended Kane Hamiltonian.[52, 62]

$$\sigma_x = \begin{pmatrix} 0 & 1 \\ 1 & 0 \end{pmatrix} \quad \sigma_y = \begin{pmatrix} 0 & -\mathrm{i} \\ \mathrm{i} & 0 \end{pmatrix} \qquad \sigma_z = \begin{pmatrix} 1 & 0 \\ 0 & -1 \end{pmatrix} \quad \mathbb{1}_{2\times 2} = \begin{pmatrix} 1 & 0 \\ 0 & 1 \end{pmatrix}$$

$$J_x = \begin{pmatrix} 0 & \sqrt{3} & 0 & 0 \\ \sqrt{3} & 0 & 2 & 0 \\ 0 & 2 & 0 & \sqrt{3} \\ 0 & 0 & \sqrt{3} & 0 \end{pmatrix} \qquad J_y = \begin{pmatrix} 0 & -\sqrt{3} & 0 & 0 \\ \sqrt{3} & 0 & -2 & 0 \\ 0 & 2 & 0 & -\sqrt{3} \\ 0 & 0 & \sqrt{3} & 0 \end{pmatrix}$$

$$J_z = \begin{pmatrix} 3 & 0 & 0 & 0 \\ 0 & 1 & 0 & 0 \\ 0 & 0 & -1 & 0 \\ 0 & 0 & 0 & -3 \end{pmatrix} \qquad \mathbb{1}_{4\times 4} = \begin{pmatrix} 1 & 0 & 0 & 0 \\ 0 & 1 & 0 & 0 \\ 0 & 0 & 1 & 0 \\ 0 & 0 & 0 & 1 \end{pmatrix}$$

$$T_x = \frac{1}{3\sqrt{2}} \begin{pmatrix} -\sqrt{3} & 0 & 1 & 0 \\ 0 & -1 & 0 & \sqrt{3} \end{pmatrix} \qquad T_y = \frac{-\mathrm{i}}{3\sqrt{2}} \begin{pmatrix} \sqrt{3} & 0 & 1 & 0 \\ 0 & 1 & 0 & \sqrt{3} \end{pmatrix}$$

$$T_z = \frac{\sqrt{3}}{3\sqrt{2}} \begin{pmatrix} 0 & 1 & 0 & 0 \\ 0 & 0 & 1 & 0 \end{pmatrix}$$

$$T_{xx} = \frac{1}{3\sqrt{2}} \begin{pmatrix} 0 & -1 & 0 & \sqrt{3} \\ -\sqrt{3} & 0 & 1 & 0 \end{pmatrix} \qquad T_{yy} = \frac{1}{3\sqrt{2}} \begin{pmatrix} 0 & -1 & 0 & -\sqrt{3} \\ \sqrt{3} & 0 & 1 & 0 \end{pmatrix}$$

$$T_{zz} = \frac{\sqrt{3}}{3\sqrt{2}} \begin{pmatrix} 0 & 1 & 0 & 0 \\ 0 & 0 & -1 & 0 \end{pmatrix}$$

$$T_{yz} = \frac{\mathrm{i}}{2\sqrt{6}} \begin{pmatrix} -1 & 0 & -\sqrt{3} & 0 \\ 0 & \sqrt{3} & 0 & 1 \end{pmatrix} \qquad T_{zx} = \frac{1}{2\sqrt{6}} \begin{pmatrix} -1 & 0 & \sqrt{3} & 0 \\ 0 & \sqrt{3} & 0 & -1 \end{pmatrix}$$

$$T_{xy} = \frac{\mathrm{i}}{\sqrt{6}} \begin{pmatrix} 0 & 0 & 0 & -1 \\ -1 & 0 & 0 & 0 \end{pmatrix}$$

A.1.4 Extended Kane Parameters

Here the parameters used for the extended Kane model are listed. For the $GaAs - Al_xGa_{1-x}As$ QW the offset of the valence bands is considered to be 35%.[114]

Table A.2: Band structure parameters of GaAs.[46, 115, 116]

E_0	E_0'	Δ_0	Δ_0'	Δ^-
1.517 eV	4.488 eV	0.341 eV	0.171 eV	−0.050i eV
P	P_0'	Q	C_k	
10.493 eVÅ	4.780i eVÅ	8.165 eVÅ	−0.0034 eVÅ	
m^*	g^*			
0.0665 m_0	−0.44			
γ_1	γ_2	γ_3	κ	q
6.85	2.10	2.90	1.20	0.01

Table A.3: Band structure parameters of $\mathrm{Al}_{0.35}\mathrm{Ga}_{0.65}\mathrm{As}$.[42, 61]

E_0	E_0'	Δ_0	Δ_0'	Δ^-
1.972 eV	4.527 eV	0.317 eV	0.171 eV	−0.085i eV
P	P_0'	Q	C_k	
9.44 eVÅ	1.17i eVÅ	6.26 eVÅ	−0.0017 eVÅ	
m^*	g^*			
0.095 m_0	0.61			
γ_1	γ_2	γ_3	κ	q
5.59	1.59	2.31	0.54	0.01

A.1.5 Semiconductor Bloch Equations

The semiconductor Bloch equations are derived by solving the Heisenberg Eq. (3.17) for the single-particle Hamiltonian Eq. 3.10 in Sec. 3.2.

$$\begin{aligned}\frac{\partial}{\partial t}\hat{a}_{\mathbf{k}}^{\dagger\lambda}\hat{a}_{\mathbf{k}}^{\lambda'} &= \frac{\mathrm{i}}{\hbar}\left[\hat{\mathrm{H}},\hat{a}_{\mathbf{k}}^{\dagger\lambda}\hat{a}_{\mathbf{k}}^{\lambda'}\right] \\ &= \frac{\mathrm{i}}{\hbar}\underbrace{\left[\hat{\mathrm{H}}_0,\hat{a}_{\mathbf{k}}^{\dagger\lambda}\hat{a}_{\mathbf{k}}^{\lambda'}\right]}_{\mathcal{A}}+\frac{\mathrm{i}}{\hbar}\underbrace{\left[\hat{\mathrm{H}}_{LM},\hat{a}_{\mathbf{k}}^{\dagger\lambda}\hat{a}_{\mathbf{k}}^{\lambda'}\right]}_{\mathcal{B}}+\frac{\mathrm{i}}{\hbar}\underbrace{\left[\hat{\mathrm{H}}_C,\hat{a}_{\mathbf{k}}^{\dagger\lambda}\hat{a}_{\mathbf{k}}^{\lambda'}\right]}_{\mathcal{C}}\end{aligned} \qquad (A.8)$$

The three commutators $\mathcal{A}$,$\mathcal{B}$ & $\mathcal{C}$ are solved separately using the Fermion anti-commutator relations:

$$\left[\hat{a}_{\mathbf{k}}^{\dagger\lambda}, \hat{a}_{\mathbf{k}'}^{\lambda'}\right]_{+} = \delta_{\lambda,\lambda'}\delta_{\mathbf{k},\mathbf{k}'} \tag{A.9a}$$

$$\left[\hat{a}_{\mathbf{k}}^{\dagger\lambda}, \hat{a}_{\mathbf{k}'}^{\dagger\lambda'}\right]_{+} = 0 \tag{A.9b}$$

$$\left[\hat{a}_{\mathbf{k}}^{\lambda}, \hat{a}_{\mathbf{k}'}^{\lambda'}\right]_{+} = 0 \tag{A.9c}$$

The commutator $\mathcal{A}$ is the homogeneous part and has the final form

$$\begin{aligned}
\frac{\mathrm{i}}{\hbar}\underbrace{\left[\hat{\mathrm{H}}_0, \hat{a}_{\mathbf{k}}^{\dagger\lambda}\hat{a}_{\mathbf{k}}^{\lambda'}\right]}_{\mathcal{A}} &= \frac{\mathrm{i}}{\hbar}\left[\sum_{\mu}\omega_{\mathbf{k}}^{\mu}\hat{a}_{\mathbf{k}}^{\dagger\mu}\hat{a}_{\mathbf{k}}^{\mu}, \hat{a}_{\mathbf{k}}^{\dagger\lambda}\hat{a}_{\mathbf{k}}^{\lambda'}\right] \\
&= \frac{\mathrm{i}}{\hbar}\sum_{\mu}\omega_{\mathbf{k}}^{\mu}\left\{\hat{a}_{\mathbf{k}}^{\dagger\mu}\hat{a}_{\mathbf{k}}^{\mu}\hat{a}_{\mathbf{k}}^{\dagger\lambda}\hat{a}_{\mathbf{k}}^{\lambda'} - \hat{a}_{\mathbf{k}}^{\dagger\lambda}\hat{a}_{\mathbf{k}}^{\lambda'}\hat{a}_{\mathbf{k}}^{\dagger\mu}\hat{a}_{\mathbf{k}}^{\mu}\right\} \\
&= \frac{\mathrm{i}}{\hbar}\sum_{\mu}\omega_{\mathbf{k}}^{\mu}\left\{\hat{a}_{\mathbf{k}}^{\dagger\mu}\hat{a}_{\mathbf{k}}^{\mu}\hat{a}_{\mathbf{k}}^{\dagger\lambda}\hat{a}_{\mathbf{k}}^{\lambda'} - \hat{a}_{\mathbf{k}}^{\dagger\mu}\hat{a}_{\mathbf{k}}^{\mu}\hat{a}_{\mathbf{k}}^{\dagger\lambda}\hat{a}_{\mathbf{k}}^{\lambda'} + \hat{a}_{\mathbf{k}}^{\dagger\mu}\hat{a}_{\mathbf{k}}^{\lambda'}\delta_{\lambda\mu} - \hat{a}_{\mathbf{k}}^{\dagger\lambda}\hat{a}_{\mathbf{k}}^{\mu}\delta_{\lambda'\mu}\right\} \\
&= \frac{\mathrm{i}}{\hbar}\left(\omega_{\mathbf{k}}^{\lambda} - \omega_{\mathbf{k}}^{\lambda'}\right)\hat{a}_{\mathbf{k}}^{\dagger\lambda}\hat{a}_{\mathbf{k}}^{\lambda'}.
\end{aligned} \tag{A.10}$$

The light-matter interaction is represented by commutator $\mathcal{B}$ and has the final form

$$\begin{aligned}
\frac{\mathrm{i}}{\hbar}\underbrace{\left[\hat{\mathrm{H}}_{LM}, \hat{a}_{\mathbf{k}}^{\dagger\lambda}\hat{a}_{\mathbf{k}}^{\lambda'}\right]}_{\mathcal{B}} &= \frac{\mathrm{i}}{\hbar}\left[\sum_{\mu\mu'}\mathbf{A}\cdot\Pi_{\mathbf{k}}^{\mu\mu'}\hat{a}_{\mathbf{k}}^{\dagger\mu}\hat{a}_{\mathbf{k}}^{\mu'}, \hat{a}_{\mathbf{k}}^{\dagger\lambda}\hat{a}_{\mathbf{k}}^{\lambda'}\right] \\
&= \frac{\mathrm{i}}{\hbar}\sum_{\mu\mu'}\mathbf{A}\cdot\Pi_{\mathbf{k}}^{\mu\mu'}\left\{\hat{a}_{\mathbf{k}}^{\dagger\mu}\hat{a}_{\mathbf{k}}^{\mu'}\hat{a}_{\mathbf{k}}^{\dagger\lambda}\hat{a}_{\mathbf{k}}^{\lambda'} - \hat{a}_{\mathbf{k}}^{\dagger\lambda}\hat{a}_{\mathbf{k}}^{\lambda'}\hat{a}_{\mathbf{k}}^{\dagger\mu}\hat{a}_{\mathbf{k}}^{\mu'}\right\} \\
&= \frac{\mathrm{i}}{\hbar}\mathbf{A}\sum_{\mu\mu'}\Pi_{\mathbf{k}}^{\mu\mu'}\left\{\hat{a}_{\mathbf{k}}^{\dagger\mu}\hat{a}_{\mathbf{k}}^{\mu'}\hat{a}_{\mathbf{k}}^{\dagger\lambda}\hat{a}_{\mathbf{k}}^{\lambda'} - \hat{a}_{\mathbf{k}}^{\dagger\mu}\hat{a}_{\mathbf{k}}^{\mu'}\hat{a}_{\mathbf{k}}^{\dagger\lambda}\hat{a}_{\mathbf{k}}^{\lambda'} + \hat{a}_{\mathbf{k}}^{\dagger\mu}\hat{a}_{\mathbf{k}}^{\lambda'}\delta_{\lambda\mu'} - \hat{a}_{\mathbf{k}}^{\dagger\lambda}\hat{a}_{\mathbf{k}}^{\mu'}\delta_{\lambda'\mu}\right\} \\
&= \frac{\mathrm{i}}{\hbar}\mathbf{A}\left\{\sum_{\mu}\Pi_{\mathbf{k}}^{\mu\lambda}\hat{a}_{\mathbf{k}}^{\dagger\mu}\hat{a}_{\mathbf{k}}^{\lambda'} - \sum_{\mu'}\Pi_{\mathbf{k}}^{\lambda'\mu'}\hat{a}_{\mathbf{k}}^{\dagger\lambda}\hat{a}_{\mathbf{k}}^{\mu'}\right\} \\
&= \frac{\mathrm{i}}{\hbar}\mathbf{A}\sum_{\mu}\Pi_{\mathbf{k}}^{\mu\lambda}\hat{a}_{\mathbf{k}}^{\dagger\mu}\hat{a}_{\mathbf{k}}^{\lambda'} - \Pi_{\mathbf{k}}^{\lambda'\mu}\hat{a}_{\mathbf{k}}^{\dagger\lambda}\hat{a}_{\mathbf{k}}^{\mu}.
\end{aligned} \tag{A.11}$$

In this section of the thesis the Coulomb interaction is omitted, $\hat{\mathrm{H}}_C = 0$. Consequently, the commutator $\mathcal{C}$ is

$$\frac{\mathrm{i}}{\hbar}\underbrace{\left[\hat{\mathrm{H}}_C, \hat{a}_{\mathbf{k}}^{\dagger\lambda}\hat{a}_{\mathbf{k}}^{\lambda'}\right]}_{\mathcal{C}} = 0. \tag{A.12}$$

The time evolution of the operator $\hat{a}_{\mathbf{k}}^{\dagger\lambda}\hat{a}_{\mathbf{k}}^{\lambda'}$ has the final form

$$\frac{\partial}{\partial t}\hat{a}_{\mathbf{k}}^{\dagger\lambda}\hat{a}_{\mathbf{k}}^{\lambda'} = \frac{\mathrm{i}}{\hbar}\left(\omega_{\mathbf{k}}^{\lambda} - \omega_{\mathbf{k}}^{\lambda'}\right)\hat{a}_{\mathbf{k}}^{\dagger\lambda}\hat{a}_{\mathbf{k}}^{\lambda'} + \frac{\mathrm{i}}{\hbar}\mathbf{A}\sum_{\mu}\Pi_{\mathbf{k}}^{\mu\lambda}\hat{a}_{\mathbf{k}}^{\dagger\mu}\hat{a}_{\mathbf{k}}^{\lambda'} - \Pi_{\mathbf{k}}^{\lambda'\mu}\hat{a}_{\mathbf{k}}^{\dagger\lambda}\hat{a}_{\mathbf{k}}^{\mu}. \tag{A.13}$$

A.2 Shift Currents in Bulk

For an excitation with two optical pulses, separated by a long delay time τ, the analytic solution of the second-order SBE is

$$\begin{aligned}\frac{\partial}{\partial t}x_k^{(2)dd'} &= \mathrm{i}\omega_k^{dd'}x_k^{(2)dd'} - \frac{\mathrm{i}}{\hbar}A(t)\sum_{\mu}\Pi_k^{\mu d}x_k^{(1)\mu d'} - \Pi_k^{d'\mu}x_k^{(1)d\mu} \\ &= \mathrm{i}\omega_k^{dd'}x_k^{(2)dd'} - \frac{\mathrm{i}}{\hbar}A(t)(\underbrace{\sum_{\bar{d}'}\Pi_k^{\bar{d}'d}x_k^{(1)\bar{d}'d'}}_{A} - \underbrace{\sum_{\bar{d}}\Pi_k^{d\prime\bar{d}}x_k^{(1)d\bar{d}}}_{B}). \qquad \text{(A.14)}\end{aligned}$$

Further evaluation of the terms A & B gives the results

$$\begin{aligned}x_k^{(2)dd'} &= e^{\mathrm{i}\omega_k^{dd'}t}\int_{-\infty}^{t}dt'e^{-\mathrm{i}\omega_g^{dd'}t'}\frac{-\mathrm{i}}{\hbar\omega_g}E(t')\cos(\omega_g t')\sum_{\bar{d}'}\Pi_k^{\bar{d}'d}x_k^{(1)\bar{d}'d'} \\ &= e^{\mathrm{i}\omega_k^{dd'}t}\sum_{\bar{d}'}\frac{-\mathrm{i}\left\langle\Pi_k^{\bar{d}'d}|E2\right\rangle}{\hbar\omega_g}\int_{-\infty}^{t}dt'e^{-\mathrm{i}\omega_k^{dd'}t'}\frac{-\mathrm{i}\left\langle\Pi_k^{d'\bar{d}'}|E1\right\rangle}{2\hbar\omega_g} \\ &\times E(t')\cos(\omega_g t'+\varphi)(E_1(-\omega_g-\omega_k^{\bar{d}'d'})+E_1(\omega_g-\omega_k^{\bar{d}'d'})) * e^{\mathrm{i}\omega_k^{\bar{d}'d'}t'} \\ &= e^{\mathrm{i}\omega_k^{dd'}t}\sum_{\bar{d}'}\frac{-\mathrm{i}\left\langle\Pi_k^{\bar{d}'d}|E2\right\rangle}{2\hbar\omega_g}\frac{-\mathrm{i}\left\langle\Pi_k^{d'\bar{d}'}|E1\right\rangle}{2\hbar\omega_g}(E_1(-\omega_g-\omega_k^{\bar{d}'d'})+E_1(\omega_g-\omega_k^{\bar{d}'d'})) \\ &\times\int_{-\infty}^{t}dt'E(t')(e^{\mathrm{i}(\omega_k^{\bar{d}'d'}-\omega_g-\omega_k^{dd'})t'}e^{-\mathrm{i}\varphi}+e^{\mathrm{i}(\omega_k^{\bar{d}'d'}+\omega_g-\omega_k^{dd'})t'}e^{\mathrm{i}\varphi})\end{aligned}$$

$$\text{(A.15)}$$

and

$$\begin{aligned}x_k^{(2)dd'} &= e^{\mathrm{i}\omega_k^{dd'}t}\sum_{\bar{d}}\frac{-\mathrm{i}\left\langle\Pi_k^{d'\bar{d}}|E2\right\rangle}{2\hbar\omega_g}\frac{-\mathrm{i}\left\langle\Pi_k^{\bar{d}d}|E1\right\rangle}{2\hbar\omega_g}(E_1(-\omega_g-\omega_k^{d\bar{d}})+E_1(\omega_g-\omega_k^{d\bar{d}})) \\ &\times\int_{-\infty}^{t}dt'E(t')(e^{\mathrm{i}(\omega_k^{d\bar{d}}-\omega_g-\omega_k^{dd'})t'}e^{-\mathrm{i}\varphi}+e^{\mathrm{i}(\omega_k^{d\bar{d}}+\omega_g-\omega_k^{dd'})t'}e^{\mathrm{i}\varphi}).\end{aligned}$$

$$\text{(A.16)}$$

Combining the solutions for the terms A and B gives the final expression for the second-order

$$\begin{aligned}
x_k^{(2)dd'} &= e^{\mathrm{i}\omega_k^{dd'}t}\int_{-\infty}^{t} dt' \frac{-1}{(2\hbar\omega_g)^2} E(t')(\\
&\quad + \sum_{\bar{d}'} \left\langle \Pi_k^{\bar{d}'d} | E2 \right\rangle \left\langle \Pi_k^{d'\bar{d}'} | E1 \right\rangle (E_1(-\omega_g - \omega_k^{\bar{d}'d'}) + E_1(\omega_g - \omega_k^{\bar{d}'d'})) \\
&\quad \times (e^{\mathrm{i}(\omega_k^{\bar{d}'d'} - \omega_g - \omega_k^{dd'})t'} e^{-\mathrm{i}\varphi} + e^{\mathrm{i}(\omega_k^{\bar{d}'d'} + \omega_g - \omega_k^{dd'})t'} e^{\mathrm{i}\varphi}) \\
&\quad - \sum_{\bar{d}} \left\langle \Pi_k^{d'\bar{d}} | E2 \right\rangle \left\langle \Pi_k^{\bar{d}d} | E1 \right\rangle (E_1(-\omega_g - \omega_k^{d\bar{d}}) + E_1(\omega_g - \omega_k^{d\bar{d}})) \\
&\quad \times (e^{\mathrm{i}(\omega_k^{d\bar{d}} - \omega_g - \omega_k^{dd'})t'} e^{-\mathrm{i}\varphi} + e^{\mathrm{i}(\omega_k^{d\bar{d}} + \omega_g - \omega_k^{dd'})t'} e^{\mathrm{i}\varphi})).
\end{aligned} \tag{A.17}$$

A.3 Coulomb Hamiltonian

The Hamilton operator of the Coulomb interaction has the form

$$\hat{\mathrm{H}}_C \approx \frac{1}{2} \sum_{\substack{\lambda_1,\lambda_2,\lambda_3,\lambda_4 \\ \mathbf{k}_3,\mathbf{k}_4,\mathbf{q}}} \hat{a}^{\dagger\lambda_1}_{\mathbf{k}_4+\mathbf{q}} \hat{a}^{\dagger\lambda_2}_{\mathbf{k}_3-\mathbf{q}} \hat{a}^{\lambda_3}_{\mathbf{k}_3} \hat{a}^{\lambda_4}_{\mathbf{k}_4} \times V^{\lambda_1,\lambda_2,\lambda_3,\lambda_4}_{\mathbf{k}_3,\mathbf{k}_4,\mathbf{q}}, \tag{A.18}$$

derived in Sec. 6.1.1. As in Sec. 3.2 the equation of motion is derived by evaluating the Heisenberg equation.

$$\begin{aligned} \frac{\mathrm{i}}{\hbar}\left[\hat{\mathrm{H}}_C, \hat{a}^{\dagger i}_{\mathbf{k}} \hat{a}^{j}_{\mathbf{k}}\right] = \frac{\mathrm{i}}{\hbar}\frac{1}{2} \sum V^{l_1 l_2 l_3 l_4}_{\mathbf{k}_3,\mathbf{k}_4,\mathbf{q}} \Big\{ &+ \hat{a}^{\dagger l_1}_{\mathbf{k}_4+\mathbf{q}} \hat{a}^{\dagger l_2}_{\mathbf{k}_3-\mathbf{q}} \hat{a}^{l_3}_{\mathbf{k}_3} \hat{a}^{l_4}_{\mathbf{k}_4} \hat{a}^{\dagger i}_{\mathbf{k}} \hat{a}^{j}_{\mathbf{k}} \\ &- \hat{a}^{\dagger i}_{\mathbf{k}} \hat{a}^{j}_{\mathbf{k}} \hat{a}^{\dagger l_1}_{\mathbf{k}_4+\mathbf{q}} \hat{a}^{\dagger l_2}_{\mathbf{k}_3-\mathbf{q}} \hat{a}^{l_3}_{\mathbf{k}_3} \hat{a}^{l_4}_{\mathbf{k}_4} \Big\} \\ = \frac{\mathrm{i}}{\hbar}\frac{1}{2} \sum V^{l_1 l_2 l_3 l_4}_{\mathbf{k}_3,\mathbf{k}_4,\mathbf{q}} \Big\{ &- \hat{a}^{\dagger l_1}_{\mathbf{k}_3+\mathbf{q}} \hat{a}^{\dagger l_2}_{\mathbf{k}_3-\mathbf{q}} \hat{a}^{l_4}_{\mathbf{k}_4} \hat{a}^{j}_{\mathbf{k}} \delta_{i,l_3} \delta_{\mathbf{k},\mathbf{k}_3} \\ &+ \hat{a}^{\dagger l_1}_{\mathbf{k}_3+\mathbf{q}} \hat{a}^{\dagger l_2}_{\mathbf{k}_3-\mathbf{q}} \hat{a}^{l_3}_{\mathbf{k}_3} \hat{a}^{j}_{\mathbf{k}} \delta_{i,l_4} \delta_{\mathbf{k},\mathbf{k}_4} \\ &- \hat{a}^{\dagger i}_{\mathbf{k}} \hat{a}^{\dagger l_2}_{\mathbf{k}_3-\mathbf{q}} \hat{a}^{l_3}_{\mathbf{k}_3} \hat{a}^{j}_{\mathbf{k}} \delta_{l_4,k_4} \delta_{\mathbf{k},\mathbf{k}_4+\mathbf{q}} \\ &+ \hat{a}^{\dagger i}_{\mathbf{k}} \hat{a}^{\dagger l_1}_{\mathbf{k}_4+\mathbf{q}} \hat{a}^{l_3}_{\mathbf{k}_3} \hat{a}^{j}_{\mathbf{k}} \delta_{j,l_2} \delta_{\mathbf{k},\mathbf{k}_3-\mathbf{q}} \Big\} \end{aligned} \tag{A.19}$$

The time-evolution of the four-point operators at the end of Eq. (A.19) is obtained by solving the Heisenberg equation for each one. However, this leads to a hierarchy problem where a $< n >$-point operator couples to a $< n+1 >$-point operator. To resolve the hierarchy problem, approximations have to be made at a certain level. In this work the Coulomb interaction is treated on the level of the Hartree-Fock approximation where the four-point operator is factorized intro products of two-point operators,

$$\langle 1234 \rangle = \langle 14 \rangle \langle 23 \rangle - \langle 13 \rangle \langle 24 \rangle . \tag{A.20}$$

In the Hartree-Fock approximation the Coulomb interaction is cut of at the level of two particle correlations, higher correlations e.g. biexcitons are not included. Applying the Hartree-Fock approximation on Eq. (A.19) and using the symmetry of the Coulomb matrix element V, the equation of motion has the form

$$\begin{aligned}\left\langle \frac{\mathrm{i}}{\hbar}\left[\hat{\mathrm{H}}_C, \hat{a}^{\dagger i}_{\mathbf{k}} \hat{a}^{j}_{\mathbf{k}}\right]\right\rangle = \frac{\mathrm{i}}{\hbar}\frac{1}{2}\sum \Big\{ & - V^{l_1 l_2 i l_4}_{\mathbf{k},\mathbf{k}_4,\mathbf{q}} \left(\left\langle \hat{a}^{\dagger l_1}_{\mathbf{k}_4+\mathbf{q}} \hat{a}^{j}_{\mathbf{k}}\right\rangle \left\langle \hat{a}^{\dagger l_2}_{\mathbf{k}-\mathbf{q}} \hat{a}^{l_4}_{\mathbf{k}_4}\right\rangle \right.\\ & \left. - \left\langle \hat{a}^{\dagger l_1}_{\mathbf{k}_4+\mathbf{q}} \hat{a}^{l_4}_{\mathbf{k}_4}\right\rangle \left\langle \hat{a}^{\dagger l_2}_{\mathbf{k}-\mathbf{q}} \hat{a}^{j}_{\mathbf{k}}\right\rangle\right) \\ & + V^{l_1 l_2 l_3 i}_{\mathbf{k}_4,\mathbf{k},\mathbf{q}} \left(\left\langle \hat{a}^{\dagger l_1}_{\mathbf{k}+\mathbf{q}} \hat{a}^{j}_{\mathbf{k}}\right\rangle \left\langle \hat{a}^{\dagger l_2}_{\mathbf{k}_4-\mathbf{q}} \hat{a}^{l_3}_{\mathbf{k}_4}\right\rangle \right.\\ & \left. - \left\langle \hat{a}^{\dagger l_1}_{\mathbf{k}+\mathbf{q}} \hat{a}^{l_3}_{\mathbf{k}_4}\right\rangle \left\langle \hat{a}^{\dagger l_2}_{\mathbf{k}_4-\mathbf{q}} \hat{a}^{j}_{\mathbf{k}}\right\rangle\right) \\ & - V^{j l_2 l_3 l_4}_{\mathbf{k}_4,\mathbf{k}-\mathbf{q},\mathbf{q}} \left(\left\langle \hat{a}^{\dagger i}_{\mathbf{k}} \hat{a}^{l_4}_{\mathbf{k}-\mathbf{q}}\right\rangle \left\langle \hat{a}^{\dagger l_2}_{\mathbf{k}_4-\mathbf{q}} \hat{a}^{l_3}_{\mathbf{k}_4}\right\rangle \right.\\ & \left. - \left\langle \hat{a}^{\dagger i}_{\mathbf{k}} \hat{a}^{l_3}_{\mathbf{k}_4}\right\rangle \left\langle \hat{a}^{\dagger l_2}_{\mathbf{k}_4-\mathbf{q}} \hat{a}^{l_4}_{\mathbf{k}-\mathbf{q}}\right\rangle\right) \\ & + V^{l_1 j l_3 l_4}_{\mathbf{k}+\mathbf{q},\mathbf{k}_4,\mathbf{q}} \left(\left\langle \hat{a}^{\dagger i}_{\mathbf{k}} \hat{a}^{l_4}_{\mathbf{k}_4}\right\rangle \left\langle \hat{a}^{\dagger l_1}_{\mathbf{k}_4+\mathbf{q}} \hat{a}^{l_3}_{\mathbf{k}+\mathbf{q}}\right\rangle \right.\\ & \left. - \left\langle \hat{a}^{\dagger i}_{\mathbf{k}} \hat{a}^{l_3}_{\mathbf{k}+\mathbf{q}}\right\rangle \left\langle \hat{a}^{\dagger l_1}_{\mathbf{k}_4+\mathbf{q}} \hat{a}^{l_4}_{\mathbf{k}_4}\right\rangle\right) \Big\} \end{aligned} \tag{A.21a}$$

$$\begin{aligned} = -\frac{\mathrm{i}}{\hbar}\sum \Big\{ & + V^{l_1 l_2 l_3 i}_{\mathbf{k}_4+\mathbf{q},\mathbf{k},\mathbf{q}} \left(\left\langle \hat{a}^{\dagger l_1}_{\mathbf{k}+\mathbf{q}} \hat{a}^{l_3}_{\mathbf{k}_4+\mathbf{q}}\right\rangle \left\langle \hat{a}^{\dagger l_2}_{\mathbf{k}_4} \hat{a}^{j}_{\mathbf{k}}\right\rangle \right.\\ & \left. - \left\langle \hat{a}^{\dagger l_1}_{\mathbf{k}+\mathbf{q}} \hat{a}^{j}_{\mathbf{k}}\right\rangle \left\langle \hat{a}^{\dagger l_2}_{\mathbf{k}_4} \hat{a}^{l_3}_{\mathbf{k}_4+\mathbf{q}}\right\rangle\right) \\ & - V^{l_1 j l_3 l_4}_{\mathbf{k}+\mathbf{q},\mathbf{k}_4,\mathbf{q}} \left(\left\langle \hat{a}^{\dagger l_1}_{\mathbf{k}_4+\mathbf{q}} \hat{a}^{l_3}_{\mathbf{k}+\mathbf{q}}\right\rangle \left\langle \hat{a}^{\dagger i}_{\mathbf{k}} \hat{a}^{l_4}_{\mathbf{k}_4}\right\rangle \right.\\ & \left. - \left\langle \hat{a}^{\dagger l_1}_{\mathbf{k}_4+\mathbf{q}} \hat{a}^{l_4}_{\mathbf{k}_4}\right\rangle \left\langle \hat{a}^{\dagger i}_{\mathbf{k}} \hat{a}^{l_3}_{\mathbf{k}+\mathbf{q}}\right\rangle\right) \Big\} . \end{aligned} \tag{A.21b}$$

The equation can be simplified further with the random phase approximation which states that the sum

$$\sum_{\mathbf{k}'} \left\langle \hat{a}^{\dagger}_{\mathbf{k}'} \hat{a}_{\mathbf{k}} \right\rangle \propto e^{\mathrm{i}(\varphi_{\mathbf{k}'} - \varphi_{\mathbf{k}})} \tag{A.22}$$

only has non neglectable contributions for $\mathbf{k}' = \mathbf{k}$ due to the anti-symmetry of the complex exponential function. In addition, the $\mathbf{q} = 0$ is omitted in the Jellium model. With both considerations, the equation of motion for the $\hat{\mathrm{H}}_C$ takes the final form

$$\begin{aligned}\left\langle \frac{\mathrm{i}}{\hbar}\left[\hat{\mathrm{H}}_C, \hat{a}^{\dagger i}_{\mathbf{k}} \hat{a}^{j}_{\mathbf{k}}\right]\right\rangle = & - \frac{\mathrm{i}}{\hbar}\sum V^{l_1 l_2 l_3 i}_{\mathbf{k}+\mathbf{q},\mathbf{k},\mathbf{q}} \left\langle \hat{a}^{\dagger l_1}_{\mathbf{k}+\mathbf{q}} \hat{a}^{l_3}_{\mathbf{k}+\mathbf{q}}\right\rangle \left\langle \hat{a}^{\dagger l_2}_{\mathbf{k}} \hat{a}^{j}_{\mathbf{k}}\right\rangle \\ & + \frac{\mathrm{i}}{\hbar}\sum V^{l_1 j l_3 l_4}_{\mathbf{k}+\mathbf{q},\mathbf{k},\mathbf{q}} \left\langle \hat{a}^{\dagger l_1}_{\mathbf{k}+\mathbf{q}} \hat{a}^{l_3}_{\mathbf{k}+\mathbf{q}}\right\rangle \left\langle \hat{a}^{\dagger i}_{\mathbf{k}} \hat{a}^{l_4}_{\mathbf{k}}\right\rangle . \end{aligned} \tag{A.23}$$

Appendix B

Magnetic Currents

The high symmetry of a zincblende structure normally causes microscopic $\omega \simeq 0$ currents to vanish. Due to the inversion asymmetry the shift current can exist for specific optical excitation. In a QW the reduced symmetry allows for new currents like the injection current. Similarly, an applied magnetic B-field reduces the symmetry in the bulk and the QW band structure which causes new effects to exist, e.g. previously forbidden photo currents. [117–123]

In this Chapter a brief discussion about the magnetic effects on the optically induced second-order $\omega \simeq 0$ currents inside the theoretical frame of the combined theory of k.p and SBE is presented. The magnetic B-field is included in the band structure by the addition of Zeeman terms to the k.p Hamiltonian:

$$\hat{\mathrm{H}}^{z}_{6c6c} = \frac{1}{2} g' \mu_B \, \boldsymbol{\sigma} \cdot \mathbf{B} \tag{B.1}$$

$$\hat{\mathrm{H}}^{z}_{8v8v} = -2\mu_B \left[\kappa' \, \boldsymbol{J} \cdot \mathbf{B} + q' \, \boldsymbol{\mathcal{J}} \cdot \mathbf{B}\right] \tag{B.2}$$

$$\hat{\mathrm{H}}^{z}_{7v7v} = -2\mu_B \kappa' \, \boldsymbol{\sigma} \cdot \mathbf{B} \tag{B.3}$$

$$\hat{\mathrm{H}}^{z}_{8v7v} = -3\mu_B \kappa' \, \boldsymbol{U} \cdot \mathbf{B} \tag{B.4}$$

The simulations are made for a magnetic field in (1-10)-direction and the system is excited by a Gaussian pulse with circular polarization. In Fig. B.1 the current parallel to the magnetic B-field is presented for varying B-field strengths. It shows that the symmetry break inside the band structure does cause the generation of a current which is linear in the external B-field as seen in Fig. (2a). A Fourier analysis, Fig. (3a), shows that the current contains a small frequency component $\approx 6\,\mathrm{meV}$ which is largely independent on the external B-field and therefore an intrinsic part of the band structure. An analysis of the band structure, in particular the region which lies in the range of the optical excitation,

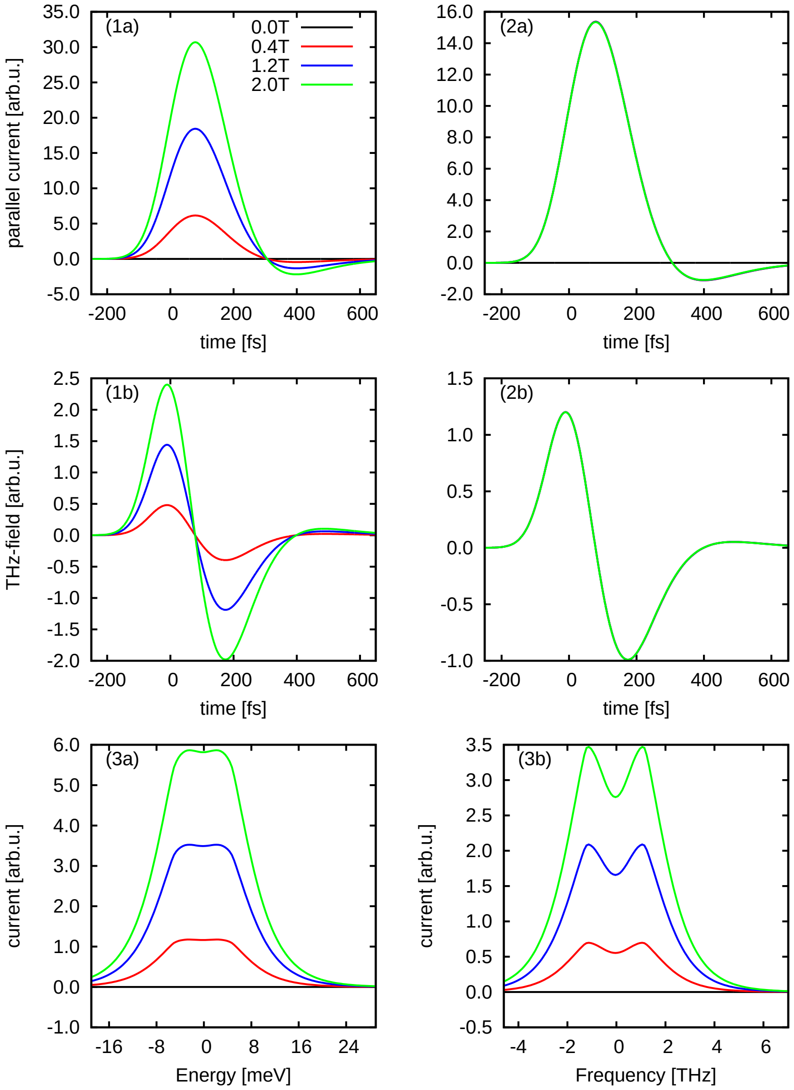

Figure B.1: A magnetic B-field in (1-10)-direction is applied to the system which is excited by a circular polarized pulse propagating in (001)-direction. (1a) The photo current generated in the system parallel to the applied B-field. (1b) is the photo current normalized to the B-field strength. The black line represents the zero current and is included as reference. (1b) and (2b) are the absolute and normalized THz-field created by the current. (3a) is the Fourier transform of (1a). (3b) is the Fourier transform of the valence band current.

reveals that the small frequency in the magnetic current corresponds to the spin splitting in the light-hole valence band, Fig. (3b). Normally due to the inversion asymmetry of the band structure, the intraband coherences cancel each other for $-\mathbf{k}$ and $+\mathbf{k}$, but due to the magnetic introduced symmetry break a small net contribution remains.

In Fig. B.2 the current in (110)-direction, perpendicular to the magnetic B-field and the optical propagation direction, is shown. In comparison to the parallel current, the perpendicular current is larger by a magnitude. This means that symmetry break in the band structure causes currents to flow mainly perpendicular to the applied magnetic field. The light-hole coherence is still contributing to the current, but its relative contribution is smaller.

In Fig. B.3(a) the current is plotted as function of the ellipticity of the optical excitation. The parallel current displays a

$$J_{\|}(\varphi) \propto \cos(\varphi) \tag{B.5}$$

dependence and has a maximum and minimum for a fully σ^- and σ^+ polarized excitation, respectively. For a linear polarization at a phase of 0.5π, which is lying parallel to the magnetic B-field, the parallel current vanishes. Seeing how σ^- and σ^+ excitation generate a current in the respective opposite direction, the linear polarization can be understood as a super position of σ^- and σ^+ light. Consequently, for a fully linear polarization the parallel current vanishes. In comparison the anti-parallel current follows

$$J_{\perp}(\varphi) \propto \sin(\varphi) + C, \tag{B.6}$$

resulting in the current being the largest for pure linear polarization and being the smallest for pure circular polarization.

In Fig. B.3(b) the angular dependence of the linearly excited photo current is plotted. The angle 0.25π is equivalent to the phase of 0.5π in Fig. B.3(a). For an angle of 0.25π and 0.75π, parallel and anti-parallel to the magnetic B-field respectively, the parallel current vanishes while the anti-parallel current is minimal and maximal. As in the case of circular polarization the parallel and anti-parallel currents display

$$\begin{aligned} J_{\|}(\theta) &\propto \cos(2\theta) \\ J_{\perp}(\theta) &\propto \sin(2\theta) + C, \end{aligned} \tag{B.7}$$

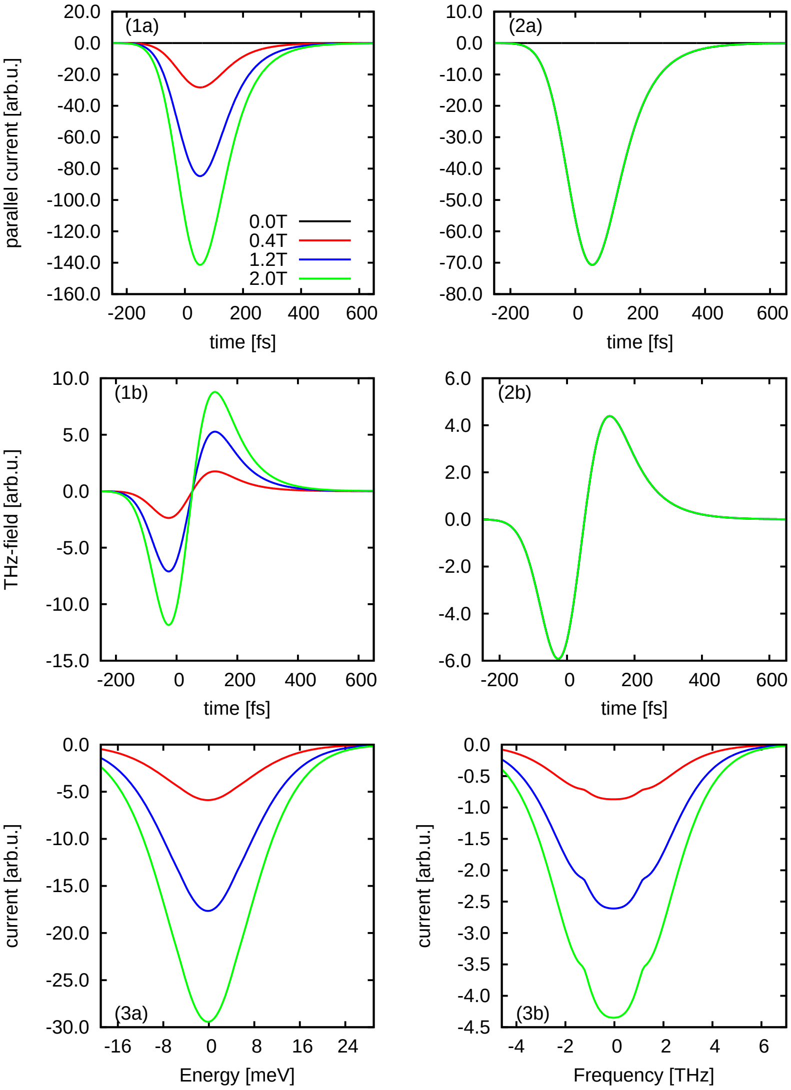

Figure B.2: As in Fig. B.1, a magnetic B-field in (1-10)-direction is applied to the system which is excited by a circular polarized pulse propagating in (001)-direction. (1a) The photo current generated in the system perpendicular to the applied B-field, flowing in (110)-direction. (1b) is the photo current normalized to the B-field strength. The zero current is again included as reference. (1b) and (2b) are the absolute and normalized THz-field created by the current. (3a) is the Fourier transform of (1a). (3b) is the Fourier transform of the valence band current.

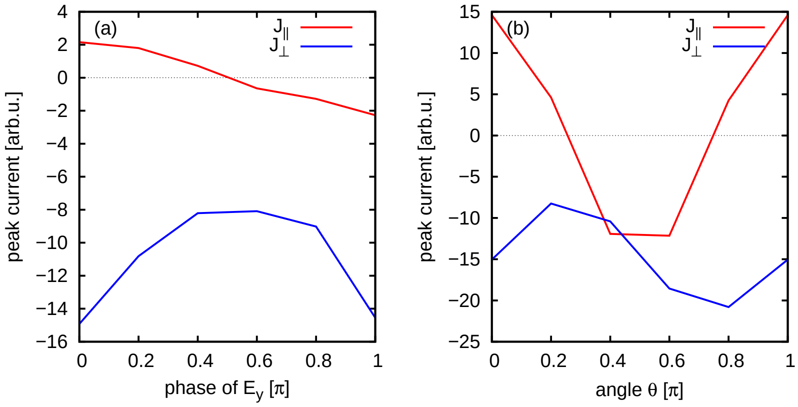

Figure B.3: The maximum value of the photo currents $J_{\|}$ and $J_{\perp}$, parallel and perpendicular to the external magnetic B-field, generated in the system with an applied B-field, 1.2 T, in (110)-direction. (a) The current dependence on the phase of the E_y component. A phase of 0π and 1π represents σ^- and σ^+ circular polarization while 0.5π is purely linear polarization in (110)-direction. (b) The peak current shwon as function of the polarization angle θ between the x-axis and the linear polarized optical excitation.

dependence. Using Jones notation the basic vectors for circular polarization are defined as

$$\begin{aligned} |{+\sigma}\rangle &= \frac{1}{\sqrt{2}}\left(|L_{\|}\rangle + \mathrm{i}|L_{\perp}\rangle\right) \\ |{-\sigma}\rangle &= \frac{1}{\sqrt{2}}\left(|L_{\|}\rangle - \mathrm{i}|L_{\perp}\rangle\right), \end{aligned} \tag{B.8}$$

with $|L_{\|}\rangle$ and $|L_{\perp}\rangle$ standing for linear polarizations parallel and perpendicular to the magnetic field, in this case (110) and (1-10), respectively. The linear polarizations can be rewritten in the circular basis as

$$\begin{aligned} |L_{\|}\rangle &= \frac{1}{\sqrt{2}}\left(|{+\sigma'}\rangle + |{-\sigma'}\rangle\right) \\ |L_{\perp}\rangle &= \frac{-\mathrm{i}}{\sqrt{2}}\left(|{+\sigma'}\rangle - |{-\sigma'}\rangle\right). \end{aligned} \tag{B.9}$$

An arbitrary linear polarization vector $|L\rangle = |L_{\|}\rangle\cos(\theta') + |L_{\perp}\rangle\sin(\theta')$ can be written as

$$\begin{aligned} |L\rangle &= \frac{1}{\sqrt{2}}\left(|{+\sigma}\rangle\left(\cos(\theta') - \mathrm{i}\sin(\theta')\right) + |{-\sigma}\rangle\left(\cos(\theta') + \mathrm{i}\sin(\theta')\right)\right) \\ &= \frac{1}{\sqrt{2}}\left(|{+\sigma}\rangle e^{-\mathrm{i}\theta'} + |{-\sigma}\rangle e^{\mathrm{i}\theta'}\right). \end{aligned} \tag{B.10}$$

Because second-order photo currents are being investigated, the square of the optical field has to be considered. It has the simple form

$$\begin{aligned} J \propto |L\rangle^2 =& |{+\sigma}\rangle^2 e^{-\mathrm{i}2\theta'} + 2|{+\sigma}\rangle|{-\sigma}\rangle + |{-\sigma}\rangle^2 e^{+\mathrm{i}2\theta'} \\ =& \left(|{+\sigma}\rangle^2 + |{-\sigma}\rangle^2\right)\cos(2\theta') + 2|{+\sigma}\rangle|{-\sigma}\rangle. \\ &+ \mathrm{i}\left(|{+\sigma}\rangle^2 - |{-\sigma}\rangle^2\right)\sin(2\theta') \end{aligned} \tag{B.11}$$

In Fig. B.3 the angle θ is the angle between the linear polarization an the x-axis, thus $\theta = \theta' + \frac{\pi}{4}$. Entering this in Eq. (B.11) and considering that $\sin(\theta + \frac{\pi}{2}) = \cos\theta$, the final expression is

$$\begin{aligned} J \propto |L\rangle^2 =& \left(|{+\sigma}\rangle^2 + |{-\sigma}\rangle^2\right)\sin(2\theta) + 2|{+\sigma}\rangle|{-\sigma}\rangle \\ &- \mathrm{i}\left(|{+\sigma}\rangle^2 - |{-\sigma}\rangle^2\right)\cos(2\theta). \end{aligned} \tag{B.12}$$

A simple comparison between Eq. (B.7) and Eq. (B.12) reveals, that the parallel current $J_{||}$ is given by the imaginary part of Eq. (B.12) while the anti-parallel current $J_{\perp}$ is given by the real part.

Similar magnetically induced photo current dependencies have been observed in GaAs QW.[121]

References

[1] H. Hertz, “Ueber einen Einfluss des ultravioletten Lichtes auf die elektrische Entladung,” *Annalen der Physik*, vol. 267, p. 983, 1887.

[2] A. Einstein, “Über einen die Erzeugung und Verwandlung des Lichtes betreffenden heuristischen Gesichtspunkt,” *Annalen der Physik*, vol. 17, p. 132, 1905.

[3] D. E. Eastman and W. D. Gorbman, “Photoemission densities of intrinsic surface states for Si, Ge and GaAs,” *Phys. Rev. Lett.*, vol. 28, p. 1378, 1972.

[4] I. Robel, V. Subramanian, M. Kuno, and P. V. Kamat, “Quantum dot solar cells. harvesting light energy with CdSe nanocrystals molecularly linked to mesoscopic TiO_2 films,” *J. Am. Chem. Soc.*, vol. 128, p. 2385, 2006.

[5] A. Mills and S. Le Hunte, “An overview of semiconductor photocatalysis,” *Journal of Photochemistry and Photobiology A: Chemistry*, vol. 108, p. 1, 1997.

[6] J. Schmutzler, P. Lewandowski, M. Aßman, D. Niemietz, S. Schumacher, M. Kamp, C. Schneider, S. Höfling, and M. Bayer, “All-optical flow control of polariton condensate using nonresonant excitation,” *Phys. Rev. B*, vol. 91, p. 195 308, 2015.

[7] M. Burgelman, P. Nollet, and S. Degrave, “Modelling polycrystalline semiconductor solar cells,” *Thin Solid Films*, vol. 361, p. 527, 2000.

[8] D. E. Aspnes, “Energy-band theory of the second-order nonlinear optical susceptibility of crystals of zinc-blende symmetry,” *Phys. Rev. B*, vol. 6, p. 4648, 1972.

[9] E. Ghahramani, D. J. Moss, and J. E. Sipe, “Full-band-structure calculation of second-harmonic generation in odd-period strained $(Si)_n/(Ge)_n$ superlattices,” *Phys. Rev. B*, vol. 43, p. 8990, 1991.

[10] M. Bieler, "THz generation from resonant excitation of semiconductor nanostructures: Investigation of second-order nonlinear optical effects," *IEEE Journal of Selected Topics in Quantum Electronics*, vol. 14, p. 458, 2008.

[11] H. Haug and S. W. Koch, *Quantum theory of the optical and electronic properties of semiconductors*, 4th, Ed. World Scientific, 2004.

[12] E. Sternemann, T. Jostmeier, C. Ruppert, S. Thunich, H. T. Duc, R. Podzimski, T. Meier, and M. Betz, "Quantum interference control of electrical currents in gaas microstructures: Physics and spectroscopic applications," *Applied Physics B*, vol. 122, p. 44, 2016.

[13] A. Haché, J. E. Sipe, and H. M. van Driel, "Quantum interference control of electrical currents in GaAs," *IEEE Journal of Quantum Electronics*, vol. 34, p. 1144, 1998.

[14] R. Atanasov, A. Haché, J. L. P. Hughes, H. M. van Driel, and J. E. Sipe, "Coherent control of photocurrent generation in bulk semiconductors," *Phys. Rev. Lett.*, vol. 76, p. 1703, 1996.

[15] R. D. R. Bhat and J. E. Sipe, "Optically injected spin currents in semiconductors," *Phys. Rev. Lett.*, vol. 85, p. 5432, 2000.

[16] M. J. Stevens, A. L. Smirl, R. D. R. Bhat, A. Najmaie, J. E. Sipe, and H. M. van Driel, "Quantum interference control of ballistic pure spin currents in semiconductors," *Phys. Rev. Lett.*, vol. 90, p. 136 603, 2003.

[17] R. von Baltz and W. Kraut, "Theory of the bulk photovoltaic effect in pure crystals," *Phys. Rev. B*, vol. 23, p. 5590, 1981.

[18] V. I. Belinicher, E. L. Ivchenko, and B. I. Sturman, "Kinetic theory of the displacement photovoltaic effect in piezoelectrics," *Sov. Phys. JETP*, vol. 56, p. 359, 1982.

[19] S. D. Ganichev, E. L. Ivchenko, S. N. Danilov, J. Eroms, W. Wegscheider, D. Weiss, and W. Prettl, "Conversion of spin into directed electric current in quantum wells," *Phys. Rev. Lett.*, vol. 86, p. 4358, 2001.

[20] H. T. Duc, T. Meier, and S. W. Koch, "Microscopic analysis of the coherent optical generation and the decay of charge and spin currents in semiconductor heterostructures," *Phys. Rev. Lett.*, vol. 95, p. 086 606, 2005.

[21] S. D. Ganichev, U. Rössler, E. L. Ivchenko, V. V. Bel'kov, R. Neumann, K. Brunner, and G. Abstreiter, "Removal of spin degeneracy in p-SiGe quantum wells demonstrated by spin photocurrents," *Phys. Rev. B*, vol. 66, p. 075 328, 2002.

[22] M. Bieler, K. Pierz, U. Siegner, and P. Dawson, "Quantum interference currents by excitation of heavy- and light-hole excitons in GaAs/$Al_{0.3}Ga_{0.7}As$ quantum wells," *Phys. Rev. B*, vol. 73, p. 241 312, 2006.

[23] B. Pasenow, H. T. Duc, T. Meier, and S. W. Koch, "Rabi flopping of charge and spin currents generated by ultrafast two-colour photoexcitation of semiconductor quantum wells," *Sol. Stat. Comm.*, vol. 352, pp. 2480–2483, 2008.

[24] S. Priyadarshi, A. M. Racu, K. Pierz, U. Siegner, M. Bieler, H. T. Duc, J. Förstner, and T. Meier, "Reversal of coherently controlled ultrafast photocurrents by band mixing in undoped GaAs quantum wells," *Phys. Rev. Lett.*, vol. 104, p. 217 401, 2010.

[25] H. T. Duc, J. Förstner, and T. Meier, "Microscopic analysis of charge and spin photocurrents injected by circularly polarized one-color laser pulses in GaAs quantum wells," *Phys. Rev. B*, vol. 82, p. 115 316, 2010.

[26] H. T. Duc, J. Förstner, T. Meier, S. Priyadarshi, A. M. Racu, K. Pierz, U. Siegner, and M. Bieler, "Oscillatory excitation energy dependence of injection currents in GaAs/AlGaAs quantum wells," *Phys. Status Solidi (c)*, vol. 8, p. 1137, 2011.

[27] M. Pochwała, H. T. Duc, J. Förstner, and T. Meier, "Intensity-dependent ultrafast dynamics of injection currents in unbiased GaAs quantum wells," *Phys. Status Solidi RLL*, vol. 5, p. 119, 2011.

[28] X.-C. Zhang, Y. Jin, K. Yang, and L. J. Schowalter, "Resonant nonlinear susceptibility near the GaAs band gap," *Phys. Rev. Lett.*, vol. 69, p. 2303, 1992.

[29] G. Dalba, Y. Soldo, F. Rocca, V. M. Fridkin, and P. Sainctavit, "Giant bulk photovoltaic effect under linearly polarized X-ray synchrotron radiation," *Phys. Rev. Lett.*, vol. 74, p. 988, 1995.

[30] Z. Chen, M. Segev, D. W. Wilson, R. E. Muller, and P. D. Maker, "Self-trapping of an optical vortex by use of the bulk photovoltaic effect," *Phys. Rev. Lett.*, vol. 78, p. 2948, 1997.

[31] N. Laman, M. Bieler, and H. M. van Driel, "Ultrafast shift and injection currents observed in wurtzite semiconductors via emitted terahertz radiation," *J. Appl. Phys.*, vol. 98, p. 103 507, 2005.

[32] M. Bieler, K. Pierz, and U. Siegner, "Simultaneous generation of shift and injection currents in (110)-grown GaAs/AlGaAs quantum wells," *J. Appl. Phys.*, vol. 100, p. 83 710, 2006.

[33] M. Bieler, K. Pierz, and U. Siegner, "Shift currents from symmetry reduction and Coulomb effects in (110)-orientated GaAs/$Al_{0.3}Ga_{0.7}As$ quantum wells," *Phys. Rev. B*, vol. 76, p. 161 304, 2007.

[34] S. Priyadarshi, M. Leidinger, K. Pierz, A. M. Racu, U. Siegner, M. Bieler, and P. Dawson, "Terahertz spectroscopy of shift currents resulting from asymmetric (110)-oriented GaAs/AlGaAs quantum wells," *J. Appl. Phys.*, vol. 95, p. 151 110, 2009.

[35] D. Côte, N. Laman, and H. M. van Driel, "Rectification and shift currents in GaAs," *J. Appl. Phys.*, vol. 80, p. 905, 2002.

[36] S. M. Young and A. M. Rappe, "First principles calculation of the shift current photovoltaic effect in ferroelectrics," *Phys. Rev. Lett.*, vol. 109, p. 116 601, 2012.

[37] S. M. Young, F. Zheng, and A. M. Rappe, "Prediction of a linear spin bulk photovoltaic effect in antiferromagnets," *Phys. Rev. Lett.*, vol. 110, p. 057 201, 2013.

[38] C. Somma, K. Reimann, C. Flytzanis, T. Elsaesser, and M. Woerner, "High-field terahertz bulk photovoltaic effect in lithium niobate," *Phys. Rev. Lett.*, vol. 112, p. 146 602, 2014.

[39] F. Nastos and J. E. Sipe, "Optical rectification and shift currents in GaAs and GaP response: Below and above the band gap," *Phys. Rev. B*, vol. 74, p. 035 201, 2006.

[40] P. Král, "Quantum kinetic theory of shift-current electron pumping in semiconductors," *J. Phys.: Condens. Matter*, vol. 12, p. 4851, 2000.

[41] J. A. Brehm, S. M. Young, and A. M. Rappe, "First-principles calculations of the bulk photovoltaic effect of the polar compounds $LiAsS_2$, $LiAsSe_2$, and $NaAsSe_2$," *J. Chem. Phys.*, vol. 141, p. 204 704, 2014.

[42] P. von Allmen, "Conduction subbands in a $GaAs/Al_xGa_{1-x}As$ quantum well: Comparing different k·p models," *Phys. Rev. B*, vol. 46, p. 18 382, 1992.

[43] W. J. Elder, R. M. Ward, and J. Zhang, "Double-group formulation of k·p theory for cubic crystals," *Phys. Rev. B*, vol. 83, p. 165 210, 2011.

[44] J. Hübner, S. Kunz, S. Oertel, D. Schuh, M. Pochwała, H. T. Duc, J. Förstner, T. Meier, and M. Oestreich, "Electron g-factor anisotropy in symmetric (110)-oriented GaAs quantum wells," *Phys. Rev. B*, vol. 84, p. 041 301, 2011.

[45] M. El kurdi, G. Fishman, S. Sauvage, and P. Boucaud, “Comparison between 6-band and 14-band k·p formalisms in SiGe/Si heterostructures,” *Phys. Rev. B*, vol. 68, p. 165 333, 2003.

[46] H. Mayer and U. Rössler, “Spin splitting and anisotropy of cyclotron resonance in the conduction band of GaAs,” *Phys. Rev. B*, vol. 44, p. 9048, 1991.

[47] P. Y. Yu and M. Cardona, *Fundamentals of semiconductors physics and materials properties*, 3rd. Springer, 2005.

[48] G. L. Bir and G. E. Pikus, *Symmetry and strain-induced effects in semiconductors.* Wiley, New York, 1974.

[49] S. Richard, F. Aniel, and G. Fishman, “Band diagrams of Si and Ge quantum wells via the 30-band k·p method,” *Phys. Rev. B*, vol. 72, p. 245 316, 2005.

[50] P. Enders, A. Bärwolff, and M. Woerner, “K·p theory of energy bands, wave functions, and optical selection rules,” *Phys. Rev. B*, vol. 51, p. 16 695, 1995.

[51] T. Fujisawam, T. Sato, M. Mitsuhara, T. Kakitsuka, T. Yamanaka, Y. Kondo, and F. Kano, “Successfull application of the 8-band $k \cdot p$ theory to optical properties of highly strained In(Ga)As/InGaAs quantum wells with strong conduction-valence band coupling,” *IEEE Journal of Quantum Electronics*, vol. 45, p. 1183, 2009.

[52] R. Winkler, *Spin-orbit coupling effects in two-dimensional electron and hole systems.* Springer, 2003.

[53] E. Sternemann, T. Jostmeier, C. Ruppert, H. T. Duc, T. Meier, and M. Betz, “Femtosecond quantum interference control of electrical currents in GaAs: Signatures beyond the perturbative $\chi^{(3)}$ limit,” *Phys. Rev. B*, vol. 88, p. 165 204, 2013.

[54] T. Meier, P. Thomas, and S. W. Koch, *Coherent semiconductor optics.* Springer, 2006.

[55] O. Schubert, M. Hohenleutner, F. Langer, F. Urbanek, C. Lange, U. Huttner, D. Golde, T. Meier, M. Kira, S. W. Koch, and R. Huber, “Subcycle control of terahertz high-harmonics generation by dynamical bloch ocillations,” *Nature Photonics*, vol. 8, p. 119, 2014.

[56] E. N. Adams, “Some consequences of possible degeneracy of energy bands in Ge,” *Physical Review*, vol. 92, p. 1063, 1953.

[57] G. Dresselhaus, A. F. Kip, and C. Kittel, “Spin-oribit interaction and the effectve masses of holes in germanium,” *Physical Review*, vol. 95, p. 568, 1954.

[58] R. H. Parmenter, “Symmetry properties of the energy bands of the zinc blende structure,” *Physical Review*, vol. 100, p. 573, 1955.

[59] G. Dresselhaus, “Spin-orbit coupling effects in zinc blende structures,” *Physical Review*, vol. 100, p. 580, 1955.

[60] J. J. Sakurai, *Modern quantum mechanics*, Revised Edition, S. F. Tuan, Ed. Addison Wesley Longman, 1993.

[61] L. Wissinger, U. Rössler, R. Winkler, B. Jusserand, and D. Richards, “Spin splitting in the electron subband of asymmetric GaAs/$\mathrm{Al}_x\mathrm{Ga}_{1-x}As$ quantum wells: The multiband envelope function approach,” *Phys. Rev. B*, vol. 58, p. 15 375, 1998.

[62] H.-R. Terbin, U. Rössler, and R. Ranvaud, “Quantum resonances in the valence bands of zinc-blende semiconductors. i. theoretical aspects,” *Phys. Rev. B*, vol. 20, p. 686, 1979.

[63] J. E. Sipe and E. Ghahramani, “Nonlinear optical response of semiconductors in the independent-particle approximation,” *Phys. Rev. B*, vol. 48, p. 11 705, 1993.

[64] C. Aversa and J. E. Sipe, “Nonlinear optical susceptibilities of semiconductors: Results with a length-gauge analysis,” *Phys. Rev. B*, vol. 52, p. 14 636, 1995.

[65] K. S. Virk and J. E. Sipe, “Semiconductor optics in length gauge: A general numerical approach,” *Phys. Rev. B*, vol. 76, no. 035213, 2007.

[66] Y.-C. Chang and R. B. James, “Saturation of intersubband transitions in p-type semiconductor quantum wells,” *Phys. Rev. B*, vol. 39, p. 12 672, 1989.

[67] C. Herring, “Effect of time-reversal symmetry on energy bands of crystals,” *Physical Review*, vol. 52, p. 361, 1937.

[68] N. O. Lipari and A. Baldereschi, “Angular momentum theory and localized states in solids. investigation of shallow aceceptor states in semiconductors,” *Phys. Rev. Lett.*, vol. 25, no. 1660, 1970.

[69] J. M. Luttinger, “Quantum theory of cyclotron resonance in semiconductors: General theory,” *Physical Review*, vol. 102, p. 1030, 1956.

[70] R. Heikes and D. A. Randall, “Numerical integration of the shallow-water equations of a twisted icosahedral grid. part i: Basic design and results of tests.,” *Monthly Weather Review*, vol. 123, p. 1862, 1995.

[71] A. Mahdavi-Amiri, E. Harrison, and S. Faramarz, “Hexagonal connectivity maps for digital earth,” *International Journal of Digital Earth*, vol. 8, p. 750, 2015.

[72] J. E. Sipe and A. I. Shkrebtii, “Second-order optical response in semiconductors,” *Phys. Rev. B*, vol. 61, pp. 5337–5352, 2000.

[73] R. Podzimski, H. T. Duc, and T. Meier, “Time-domain calculations of shift currents in bulk GaAs,” *Proc. SPIE*, vol. 93611V, p. 9361, 2015.

[74] J. R. Petta, A. C. Johnson, J. M. Taylor, E. A. Laird, A. Yacoby, M. D. Lukin, C. M. Marcus, M. P. Hanson, and A. C. Gossard, “Coherent manipulation of coupled electron spins in semiconductor quantum dots,” *Science*, vol. 309, p. 2180, 2005.

[75] A. P. Heberle, J. J. Baumberg, and K. Kohler, “Ultrafast coherent control and destruction of excitons in quantum wells,” *Phys. Rev. Lett.*, vol. 75, p. 2598, 1995.

[76] M. Spasenovic, M. Betz, L. Costa, and H. M. van Driel, “All-optical coherent control of electrical currents in centrosymmetric semiconductors,” *Phys. Rev. B*, vol. 77, p. 085 201, 2008.

[77] J. Güdde, M. Rohleder, T. Meier, S. W. Koch, and U. Höfer, “Time-resovled investigation of coherent controlled electric currents at a metal surface,” *Science*, vol. 318, p. 1287, 2007.

[78] A. M. Racu, S. Priyadarshi, M. Leidinger, U. Siegner, and M. Bieler, “Coherent control of ultrafast shift currents in GaAs with chirped optical pulses,” *Optics Letters*, vol. 34, p. 2784, 2009.

[79] M. O. Nestoklon and S. A. Tarasenko, “Spin splitting of electron states in (110) quantum wells: Symmetry analysis and k·p theory versus microscopic calculations,” *Phys. Rev. B*, vol. 85, p. 205 307, 2012.

[80] R. Podzimski, H. T. Duc, and T. Meier, “Photocurrents in semiconductors and semiconductor quantum wells analyzed by k.p-based bloch equations,” *Proc. SPIE*, vol. 97460W, p. 9746, 2016.

[81] H. T. Duc, R. Podzimski, S. Priyadarshi, M. Bieler, and T. Meier, “Ultrafast shift and rectification photocurrents in gaas quantum wells: Excitation intensity dependence and the importance of band mixing,” *Phys. Rev. B*, vol. 94, p. 085 305, 2016.

[82] G. H. Wannier, “The structure of electronic excitation levels in insulating crystals,” *Physical Review*, vol. 52, p. 191, 1937.

[83] N. Saigal, V. Sungunakar, and S. Ghosh, “Exciton binding energy in bulk MoS_2: A reassessment,” *Applied Physics Letters*, vol. 108, p. 132 105, 2016.

[84] D. A. B. Miller, D. S. Chemla, T. C. Damen, A. C. Gossard, W. Wiegmann, T. H. Wood, and C. A. Burrus, “Band-edge electronabsorption in quantum well structures: The quantum-confined Stark effect,” *Phys. Rev. Lett.*, vol. 53, p. 2173, 1984.

[85] R. L. Greene, K. K. Bajaj, and D. E. Pheleps, “Energy levels of wannier excitons in GaAs-$Ga_{1-x}Al_xAs$ quantum-well structures,” *Phys. Rev. B*, vol. 29, p. 1807, 1984.

[86] H. Zhao and S. Mazumdar, “Electron-electron interaction effects on the optical excitations of semiconducting single-walled carbon nanotubes,” *Phys. Rev. Lett.*, vol. 93, p. 157 402, 2004.

[87] H. Liu, S. Schumacher, and T. Meier, “Influence of Coulomb-induced band couplings on linear excitonic absorption spectra of semiconducting carbon nanotubes,” *Phys. Rev. B*, vol. 89, p. 155 407, 2014.

[88] D. D. Sell, “Resolved free-exciton transitions in the optical-absorption spectrum of GaAs,” *Phys. Rev. B*, vol. 6, p. 3750, 1972.

[89] M. Parenteau, C. Carlone, and S. M. Khanna, “Damage coefficient associated with free exciton lifetime in GaAs irradiated with neutrons and electrons,” *J. Appl. Phys.*, vol. 71, p. 3747, 1992.

[90] M. Lindberg, Y. Z. Hu, R. Binder, and S. W. Koch, “$\chi^{(3)}$ formalism in optically excited semiconductors and its applications in four-wave-mixing spectroscopy,” *Phys. Rev. B*, vol. 50, p. 18 060, 1994.

[91] W. Langbein, T. Meier, S. W. Koch, and J. M. Hvam, “Spectral signatures of $\chi^{(5)}$ processes in four-wave mixing of homogeneously broadened excitons,” *J. Opt. Soc. Am. B*, vol. 18, p. 1318, 2001.

[92] R. Zimmermann and C. Trallero-Giner, “Exciton-phonon resonance in the continuum absorption of bulk semiconductors,” *Phys. Rev. B*, vol. 56, p. 9488, 1997.

[93] S. Rudin and T. L. Reinecke, “Exciton-acoustic-phonon linewidths in GaAs bulk and quantum wells,” *Phys. Rev. B*, vol. 65, p. 121 311, 2002.

[94] R. D. R. Bhat and J. E. Sipe, “Excitonic effects on the two-color coherent control of interband transitions in bulk semiconductors,” *Phys. Rev. B*, vol. 72, p. 075 205, 2005.

[95] V. Turkowski and C. A. Ullrich, "Time-dependent density-functional theory for ultrafast interband excitations," *Phys. Rev. B*, vol. 77, p. 075 204, 2008.

[96] V. Turkowski, A. Leonardo, and C. A. Ullrich, "Time-dependent density-functional approach for exciton binding energies," *Phys. Rev. B*, vol. 79, p. 233 201, 2009.

[97] Z.-h. Yang, Y. Li, and C. A. Ullrich, "A minimal model for excitons within time-dependent density-functional theory," *J. Chem. Phys.*, vol. 137, p. 014 513, 2012.

[98] Z.-h. Yang and C. A. Ullrich, "Direct calculation of exciton binding energies with time-dependent density-functional theory," *Phys. Rev. B*, vol. 87, p. 195 204, 2013.

[99] Y.-F. Jiang, N.-P. Wang, and M. Rohlfing, "Electronic excitations of bulk LiCl from many-body perturbation theory," *J. Chem. Phys.*, vol. 139, p. 214 710, 2013.

[100] W. W. Chow and S. W. Koch, *Semiconductor-laser fundamentals*. Springer-Verlag Berlin Heidelberg, 1999.

[101] C. Authors and editors of the volumes III/17A-22A-41A1a, "Gallium arsenide (gaas) dielectric constants," in *Landolt-Börnstein - Group III Condensed Matter, Lattice Properties*, U. Rössler and D. Strauch, Eds., vol. 41A1a, Springer-Verlag Berlin Heidelberg, 2001.

[102] M. Bass, P. A. Franken, J. F. Ward, and G. Weinreich, "Optical rectification," *Phys. Rev. Lett.*, vol. 9, p. 446, 1962.

[103] A. Bonvalet, M. Joffre, J. L. Martin, and A. Migus, "Generation of ultrabroadband femtosecond pulses in the mid-infrared by optical rectification of 15 fs pulses at 100 MHz repitition rate," *Applied Physics Letters*, vol. 67, p. 2907, 1995.

[104] A. Rice, Y. Jin, X. F. Ma, X.-C. Zhang, D. Bliss, J. Larkin, and M. Alexander, "Terahertz optical rectification from $< 110 >$ zink-blende crystals," *Applied Physics Letters*, vol. 64, p. 1324, 1994.

[105] F. Kadlec and P. Kuzel, "Study of terahertz radiation generated by optical rectification on thing gold films," *Optics Letters*, vol. 30, p. 1402, 2005.

[106] D. Côte, J. E. Sipe, and H. M. van Driel, "Simple methode for calculating the propagation of terahertz radiation in experimental geometries," *J. Opt. Soc. Am. B*, vol. 20, p. 1374, 2003.

[107] S. L. Chuang, S. Schmitt-Rink, B. I. Greene, P. N. Saeta, and F. J. Levi, "Optical rectification at semiconductor surfaces," *Phys. Rev. Lett.*, vol. 68, p. 102, 1992.

[108] N. Pons, N. Cavassilas, L. Raymond, F. Michelini, M. Lannoo, and M. Besconda, "Three-dimensional k·p real-space quantum transport simulations of p-type nanowire transistors: Influence of ionized impurities," *Applied Physics Letters*, vol. 99, p. 082 113, 2011.

[109] N. Akhavan, G. Jolley, G. Umana-Membreno, J. Antoszewski, and L. Faraone, "Atomistic modelling of p-channel junctionless silicon nanowire transistor: K.p approach," in *International Conference on Nanoscience and Nanotechnology*, IEEE, New York, 2014, p. 17.

[110] Y. Fang, F. Duqeu-Gomez, and J. E. Sipe, "Dynamics of the effective mass and the anomalous velocity in two-dimensional lattices," *Phys. Rev. A*, vol. 90, p. 053 407, 2014.

[111] S. Priyadarshi, K. Pierz, and M. Bieler, "Detection of the anomalous velocity with subpicosecond time resolution in semiconductor nanostructures," *Phys. Rev. Lett.*, vol. 115, p. 257 401, 2015.

[112] P. Löwdin, "A note on the quantum–mechanical perturbation theory," *J. Chem. Phys.*, vol. 19, p. 1396, 1951.

[113] J. M. Luttinger and W. Kohn, "Motion of electrons and holes in perturbed periodic fields," *Physical Review*, vol. 97, p. 869, 1951.

[114] J. Menendez, A. Pinczuk, D. J. Werder, A. C. Gossard, and J. H. English, "Light scattering determination of band offsets in GaAs-Al$_x$Ga$_{1-x}$As quantum wells," *Phys. Rev. B*, vol. 33, p. 8863, 1986.

[115] D. E. Aspnes and A. A. Studna, "Schottky-barrier electroreflectance: Application to GaAs," *Phys. Rev. B*, vol. 7, p. 4606, 1973.

[116] M. Cardona, N. E. Christensen, and G. Fasol, "Relativistic band structure and spin-orbit splitting of zinc-blende-type semiconductors," *Phys. Rev. B*, vol. 38, p. 1806, 1988.

[117] E. L. Ivchenko, Y. B. Lyanda-Geller, and G. E. Pikus, "Circular magnetophotocurrent and spin splitting of band states in optically-inactive crystals," *Sol. Stat. Comm.*, vol. 69, p. 663, 1989.

[118] V. L. Al'perovich, A. O. Minaev, and A. S. Terekhov, "Ballistic electron transport through epitaxial GaAs films in a magnetically induced surface photocurrent," *JETP Letters*, vol. 49, p. 702, 1989.

[119] M. J. Snelling, G. P. Flinn, A. S. Plaut, R. T. Harley, and A. C. Tropper, “Magnetic g factor of electrons in GaAs/$\mathrm{Al}_x\mathrm{Ga}_{1-x}\mathrm{As}$ quantum wells,” *Phys. Rev. B*, vol. 44, p. 11 345, 1991.

[120] R. Fiederling, M. Keim, G. Reuscher, W. Ossau, G. Schmidt, W. A., and M. L. W., “Injection and detection of a spin-polarized current in a light-emitting diode,” *Nature*, vol. 402, p. 787, 1999.

[121] V. V. Bel’kov, S. D. Ganichev, E. L. Ivchenko, S. A. Tarasenko, W. Weber, S. Giglberger, M. Olteanu, H.-P. Tranitz, S. N. Danilov, P. Schneider, W. Wegscheider, D. Weiss, and W. Prettl, “Magneto-gyrotropic photogalvanic effects in semiconductor quantum wells,” *J. Phys.: Condens. Matter*, vol. 17, p. 3405, 2005.

[122] C. B. Schmidt, S. Priyadarshi, S. A. Tarasenko, and M. Bieler, “Ultrafast magneto-photocurrents in GaAs: Separation of surface and bulk contributions,” *Applied Physics Letters*, vol. 106, p. 124 108, 2015.

[123] C. B. Schmidt, S. Priyadarshi, K. Pierz, and M. Bieler, “Ultrafast magneto-photocurrents as probe of anisotropy relaxation in GaAs,” *Applied Physics Letters*, vol. 108, p. 102 104, 2016.

Danksagung

Mein Dank gilt Professor Dr. Torsten Meier für meine Aufnahme in seine Arbeitsgruppe *Computational Optoelectronics and Photonics*, in der ich unter seiner Betreuung meinen Bachelor- und Master-Abschluss erlangt habe und letztendlich meine Promotion in der theoretischen Physik beginnen konnte. Ohne seine Unterstützung und Geduld wäre die Erstellung dieser Dissertation nicht möglich gewesen.

Mein Dank gilt auch Dr. Huynh Thanh Duc für die hilfreiche Einführung und spätere Zusammenarbeit im Forschungsgebiet der Photoströme. Nur mit Hilfe seine Vorarbeit zum Thema der Photoströme ist mein schneller Einstieg in das Themengebiet möglich gewesen.

Auch möchte ich mich bei meinen Arbeitskollegen für die gemeinsame Arbeit und das freundliche Arbeitsklima bedanken, besonderer Dank gilt Dr. Matthias Reichelt und Dr. Przemyslaw Lewandowski. Wegen seiner anhaltenden Hilfsbereitschaft möchte ich mich auch bei meinem alten Bürokollegen Dr. Christian Wiebler bedanken.

Für ihre Freundlichkeit und Arbeit möchte ich mich auch bei unserer Sekretärin Frau Simone Lange bedanken.

Viele Dank gilt auch meinen Eltern und meiner restlichen Familie für die Liebe und Unterstützung, die sie mir geben.